Holocene Relative Sea-level Changes in Evenes, Northern Norway

Master's Thesis in Physical Geography

Mohib Billah

Department of Geography

University of Bergen

June 2020

Acknowledgments

First of all, I would like to thank my principal supervisor Kristian Vasskog (Department of Geography, UiB), for his unlimited support throughout the program. I am also grateful to Svein Olaf Dahl (Department of Geography, UiB), my co-supervisor, for his heartfelt support during the same period.

My special thanks go to Svein Olaf Dahl, Kristian Vasskog, Pål Ringkjøb Nielsen, Matthew James Jenkin, and Joseph Michael Buckby for their contributions to conduct fieldwork.

While conducting different laboratory experiments required to accomplish the study, I got extensive cooperation from Kristian Vasskog. Eivind Nagel Støren (EARTH LAB, UiB) and Lubna Al-Saadi (Sediment Laboratory, UiB) provided necessary support to conduct different lithostratigraphic experiments. Lars Gjermund Evja (Department of Earth Science, UiB) helped me preparing phytoplankton samples for microscopic analysis. Anne Elisabeth Bjune (Department of Biology, UiB) provided required instructions and support to identify different phytoplankton species. I am grateful to all of them.

I am thankful to John-Inge Svendsen, Atle Nesje, and Jostein Bakke of the Department of Earth Science, UiB, and Rannveig Øvrevik Skoglund, Gidske Leknæs Andersen, Pål Ringkjøb Nielsen, and Benjamin Aubrey Robson of the Department of Geography, UiB, for their extended cooperation throughout the program. I am also grateful to Peter Andersen and Grethe Meling of the Department of Geography, UiB, for their wholehearted support every time required. Also, I would like to thank everyone connected to UiB for their respective cooperation during my study period. My heartfelt thanks to all of my classmates, specially Ane, Anna, Heidi, Joe, Ole, Ranveig, and Sunniva, for making the time I spent at the UiB memorable.

Last but not least, I would like to express my special gratitude to my parents and family members for their love and support throughout my life.

Bergen, June 2020 Mohib Billah

Abstract

The relative sea-level curve of Evenes has been revised based on bio, and lithostratigraphic analysis of an isolation basin (Pålsvatnet) which has an outlet threshold located at 23.74 m above present-day mean sea level (a.s.l.), and the lithostratigraphic boundary between topset and foreset of a glaciofluvial delta (74.49 m a.s.l.). The altitudes are adjusted for the tidal influence so that they correspond to the past mean sea level. For Pålsvatnet, results from X-ray fluorescence (XRF), magnetic susceptibility (MS), and loss on ignition (LoI) were analyzed to determine the isolation contact. A simple form of phytoplankton analysis, a less time-consuming method compared to diatom analysis, has been applied to determine the isolation contact of the lake more precisely. A total of six radiocarbon dates were conducted to establish the chronology of the investigated basin. Terrestrial macrofossils have been used for radiocarbon dating to avoid problems related to hard-water effect. Based on an age-depth model including all six dates, the age of the isolation of the lake was estimated to 6240 ± 60 calibrated years before present (cal BP). The altitude of the glaciofluvial delta was incorporated to minimize the altitudinal error associated with the marine limit of the area. In the reconstructed sea-level curve, the regression rate is found to be declining from the period after deglaciation to the late Holocene. Considering the rate of Holocene eustatic sea-level rise, a net postglacial land uplift of approximately 130 m is inferred. A shoreline diagram was constructed, between Leknes and Evenes, with shoreline gradients calculated to 0.79 m/km, 0.54 m/km, 0.37 m/km, 0.24 m/km, 0.22 m/km, 0.20 m/km. 0.15 m/km, 0.10 m/km, 0.06 m/km and 0.04 m/km for the periods 10,000 cal BP, 9000 cal BP, 8000 cal BP, 7000 cal BP, 6000 cal BP, 5000 cal BP, 4000 cal BP, 3000 cal BP, 2000 cal BP, and 1000 cal BP, respectively. The constructed shoreline diagram suggests that the Tapes transgression could have extended about 40 km further inland, from Leknes, considering where the 7000 cal BP and 8000 cal BP shorelines intersect each other. A layer of sandy gravel is found at the bottom of the core that is interpreted as a tsunami layer. It would probably be deposited during the pre-historical event of the Storegga tsunami that took place around 8150 cal BP.

Table of Contents

List of Figures

List of Tables

1. Introduction

The rapidly increasing rate of the global sea-level rise, from a few centimeters per century of the late Holocene rate to a few tens of centimeters per century in recent decades (Milne et al., 2009; Gehrels and Woodworth, 2013), has been considered as one of the most important global concerns and is strongly related to climate change (Gornitz, 2013: 149; Dutton et al., 2015). With the inception of modern devices, e.g., satellite altimetry, Argo network, and Gravity Recovery and Climate Experiment (GRACE) satellite missions, more precise measurement of the modern-day sea-level change has become possible (Milne et al., 2009; Gornitz, 2013: 154). According to the special report on the Ocean and Cryosphere in a Changing Climate of Intergovernmental Panel on Climate Change (IPCC), the global sea-level has increased 3.6 mm yr^{-1} over the period 2006 -2015 (IPCC, 2019). Under RCP8.5, one of the Representative Concentration Pathways (RCPs) developed as a basis of long-term and near-term climate modeling (Van Vuuren et al., 2011), the rate of global sea-level rise could be as high as 15 mm yr^{-1} in 2100 (Oppenheimer et al., 2019). The exchange of water between ice and ocean due to fluctuations of global mean temperature (Dutton et al., 2015), and the Earth's dynamic response to the changing surface load are the dominant source for the eustatic sea-level rise (Lambeck et al., 2014). In order to project the future sea-level change based on future climate scenarios, it is essential to know how the sea-level changed during the pre-industrial era (Barnett et al., 2015). More precise palaeo sea-level reconstructions with less uncertainty range from different geographical settings can help to reconstruct global sea-level change (Bloom et al., 1974; Lambeck et al., 2014), and projecting future sea-level change with higher confidence (Oppenheimer et al., 2019).

Eustatic sea level, that was 125 ± 5 m lower than present-day sea level approximately 21 thousand years ago the last glacial maximum (LGM) (Benn and Evans, 2013: 240-1), has been rising in general after the end of the LGM (Lambeck et al., 2014). Relative (local) sea-level rise, on the other hand, has not been increasing uniformly around the world (Milne et al., 2009); it has even been falling in places that were covered by ice during the last glaciation, especially after the Younger Dryas period (~11600 cal BP) (Chappell, 1983; Møller, 1989; Rasmussen et al., 2006; Lohne et al., 2007; Benn and Evans, 2013). Relative sea-level (RSL) change occurs as a result of vertical adjustment of the sea surface and/or the landmass in a regional setting; crustal movements due to tectonic activity or isostatic change may cause vertical movement of

the land, while, eustasy (glacio, tectono, and geoid), and local meteorological, hydrological and oceanographic changes contribute to the changes in sea level (Mörner, 1976; Shennan et al., 2015). Due to the retreat of the Scandinavian ice sheet and small glaciers after the Younger Dryas, Fennoscandia experienced a glacio-isostatic rebound (Berglund, 2004). As a result, a relative sea-level fall has been the general trend in the coastal areas of Norway throughout the Holocene, except for the mid-Holocene transgression that took place in many Norwegian coastal sites due to a higher rate of global ice melting compared to vertical land uplift (Simpson et al., 2015). Norway is a classical area for studies of ancient shorelines and sea-level histories due to the widespread occurrence of isolation basins, a natural depression situated below the postglacial marine limit that has been isolated from the sea due to changes in relative sea level (Kjemperud, 1986; Svendsen and Mangerud, 1987; Lohne et al., 2007; Balascio et al., 2011; Long et al., 2011; Romundset et al., 2018; Vasskog et al., 2019). Among a variety of coastal environments used to reconstruct relative sea-level history, isolation basins are particularly useful, as they can preserve continuous sedimentary archives of marine-lacustrine transitions and the facies transitions can be robustly dated on centennial timescales by radiocarbon dating of terrestrial plant remains. Additionally, the elevation of the basin threshold provides a stable sea-level index point that represents the palaeo-shoreline (mean high-tide sea level) at the time of isolation (Svendsen and Mangerud, 1987; Long et al., 2011; Romundset et al., 2018; Vasskog et al., 2019).

1.1. Objectives of the Study

The main aim of this research is to upgrade the existing Holocene (~11600 cal BP until present (Rasmussen et al., 2006; Lohne et al., 2007)) shore-level displacement curve of Møller (1989) and Lid (2019); and reconstruct the sea-level change that occurred primarily during the mid-Holocene in Evenes, northern Norway. The plan was to determine the isolation boundary using sediment cores retrieved from the isolation basin Pålsvatnet. The lake was selected based on its location and altitude to complement the existing palaeo sea-level data from the area. Several lithostratigraphic, geophysical, geochemical, and biostratigraphic tools have been applied to find the isolation contact in the retrieved sediment cores, although phytoplankton analysis, a biostratigraphic tool, is the main focus of this study. This analysis is based on counting specimens of microscopic freshwater algae and marine dinoflagellates in the sediment. Using the age derived from radiocarbon dating, and the altitude of the lake threshold, it is thus possible to add a sea-level index point to update the existing sea-level curves.

Another important part of improving the existing RSL curve was to determine the marine limit, i.e., the post-glacial highest sea level, of the area more precisely. Lid (2019) did not find any marine sediment from Store Trøsevatnet, a bog that had the threshold height at 73.5 m above the mean sea level, whereas the marine limit proposed by NGU (2020a) was 75 m above mean sea level. Thus, it became an interesting issue for this study to trace the marine deposit from places close to the expected marine limit and update the existing Quaternary geomorphological map of the area of interest.

Another aim of this work was to infer the Holocene land uplift trend (Lohne et al., 2007; Vasskog et al., 2019) using the eustatic sea-level curve and the updated sea-level diagram of this study. Such a land uplift trend can provide a general picture of the glacio-isostatic rebound of the area, and contribute to improvements of global glacial isostatic adjustment models (Peltier et al., 2015).

Recently, deposits from the Storegga tsunami, a major tsunami event that struck the Norwegian coast around 8150 years ago (Bondevik et al., 2012), were discovered in Lofoten (Midtun, 2019). A secondary aim of this research was, therefore, to analyze the sediment core for signals of any extreme natural events to investigate if the Storegga tsunami also impacted the Evenes area.

The final aim of this study was to construct a shoreline diagram for the area between Leknes (Vestvågøy municipality) and Evenes (Evenes municipality) of northern Norway combining the sea-level diagrams of Leknes (Midtun, 2019) and Evenes (updated curve from this study), and calculate gradients for shorelines of different ages. Such a shoreline diagram helps reconstruct a general overview of sea-level change that has occurred in places located between the sites with the sea-level curves (Svendsen and Mangerud, 1987).

1.2. Theoretical Background

Sea-level change can be measured in two ways, i.e., relative sea level (relative to a fixed point on land) and absolute sea level (relative to the Earth's center of mass). A wide variety of processes (e.g., vertical movement of the landmasses, ice melting, terrestrial water storage,

ocean circulation, density changes of the ocean water) are involved for the changes of both absolute and relative sea level (Milne et al., 2009), and all these processes are summarized in figure 1.1.

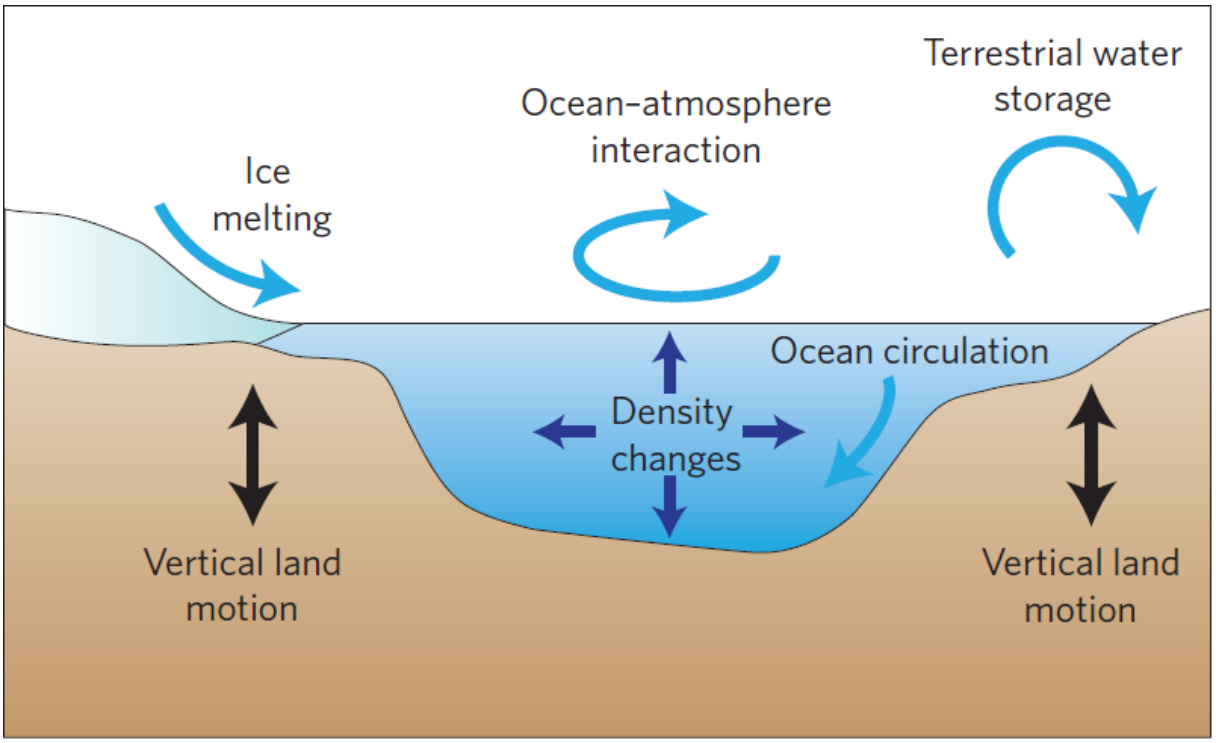

Figure 1.1: Process influencing relative and absolute sea-level changes (Milne et al., 2009).

The eustatic (absolute) sea-level has fluctuated significantly with the inception of glacial and interglacial periods throughout the Quaternary (the last ~ 2.6 million years) (Dutton et al., 2015), while after the last glacial maximum (LGM), the general trend of the eustatic sea level has been rising (figure 1.2). After the LGM, the general sea-level rise halted or slowed down during periods of glacial re-advance like the Younger Dryas (Lambeck et al., 2014), whereas it accelerated during the warm interstadials like the Bølling and Allerød (Deschamps et al., 2012). Periods with unusual high sea-level rise are termed as meltwater pulses (MP), e.g., MP1A, MP1B, MP1C (Cronin et al., 2007; Stanford et al., 2011). During the early part of the Holocene interglacial, the sea-level rise was comparatively faster as a response to melting of some large ice sheets, e.g., the Scandinavian ice sheet and, the Laurentide ice sheet (Bryson et al., 1969; Carcaillet et al., 2012). However, since many glaciers and some of the ice-sheets disappeared completely during the early Holocene, the rate of eustatic sea-level rise became slower from the period between the mid-Holocene and the late Holocene (Gornitz, 2013: 137-9; Lambeck et al., 2014). After several thousand year long period of stable sea levels, the rate started accelerating again at the beginning of the twentieth century (Gehrels and Woodworth, 2013) due to increase

of global mean temperature as a response of higher CO_2 concentration in the atmosphere (Dutton et al., 2015). Throughout the Holocene, the relative sea level of Fennoscandia is falling except for the mid-Holocene transgression known as the Tapes transgression, which occurred in the outer coastal areas as the isostatic uplift for a period became slower than the eustatic sea-level rise (Simpson et al., 2015). However, data from the instrumental period reveals a return to a positive trend in RSL change in some of the coastal areas of Norway (Richter et al., 2012).

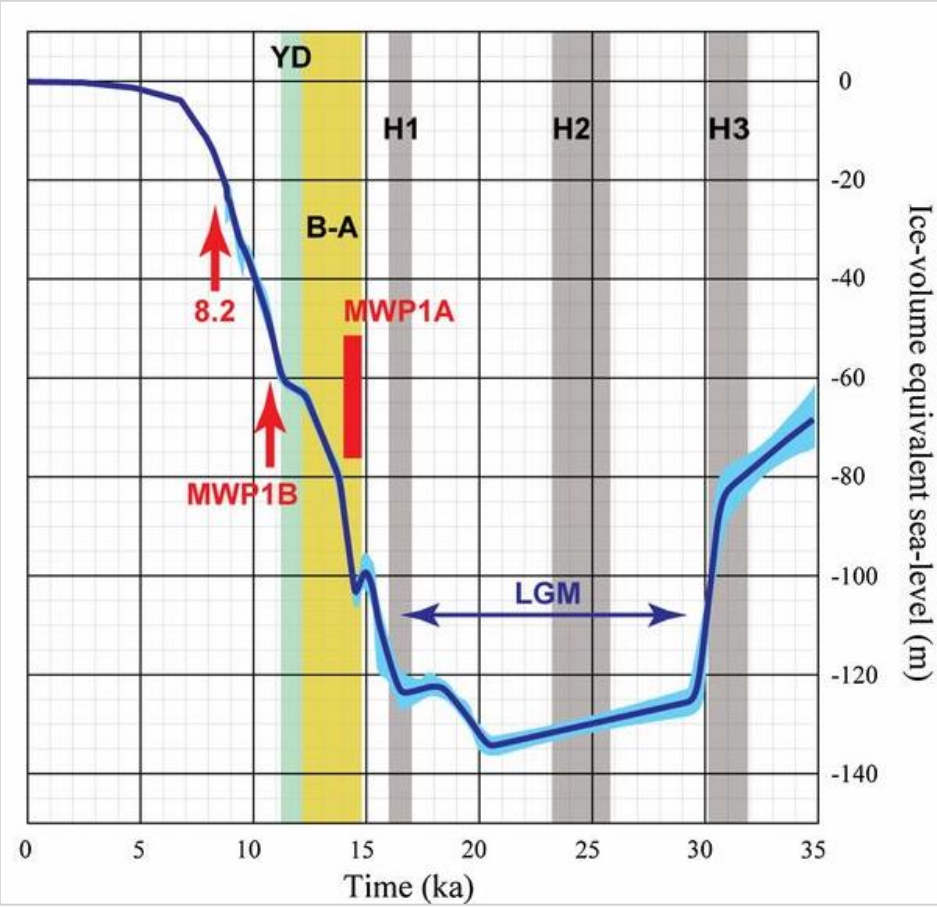

Figure 1.2: The ice-volume equivalent sea-level change for the last 30,000 cal BP. Major climatic events e.g., the last glacial maximum (LGM), Heinrich events H1 to H3, Bølling-Allerød (B-A) warm period, meltwater pulse 1A (MWP1A), Younger Dryas (YD) Cold period, meltwater pulse 1B (MWP1B), 8.2 K cal BP cooling event, are also shown (Lambeck et al., 2014).

RSL fluctuations occur as a result of the interaction between changes in sea-level and land (figure 1.3). Three types of eustasy control sea level: (1) Glacial eustasy: variations in the amount of ocean water related to global glacial volume, (2) Tectono-eustasy: alteration of ocean basin volume due to tectonic changes, and (3) Geoidal eustasy: geodial changes due to variations in the Earth's gravity field (Mörner, 1976; Anundsen and Fjeldskaar, 1983). In addition to these three types of eustasy, local meteorological, hydrological, and oceanographic

changes may contribute to sea-level changes. While geoidal eustasy may vary significantly over the globe, glacial eustasy and tectono-eustasy cause uniform change in global sea level (Mörner, 1976; Anundsen and Fjeldskaar, 1983). The land is influenced by crustal movement (and local compaction) that includes glacio-isostatic, hydro-isostatic, and tectonic processes (figure 1.4). The area covered with the thickest part of ice experiences the highest amount of uplift, for example, Ångermanland of Sweden has experienced the highest amount of uplift over Fennoscandia as it had the thickest amount of ice cover during the LGM (Berglund, 2004), while the amount of uplift reduces gradually towards the margin of the former ice sheet. In contrast, the areas located in the forebulge region, e.g., the Netherlands, southern North Sea, areas in front of the previous ice sheet margin, may experience subsidence as a result of glacial forebulge collapse (Vink et al., 2007).

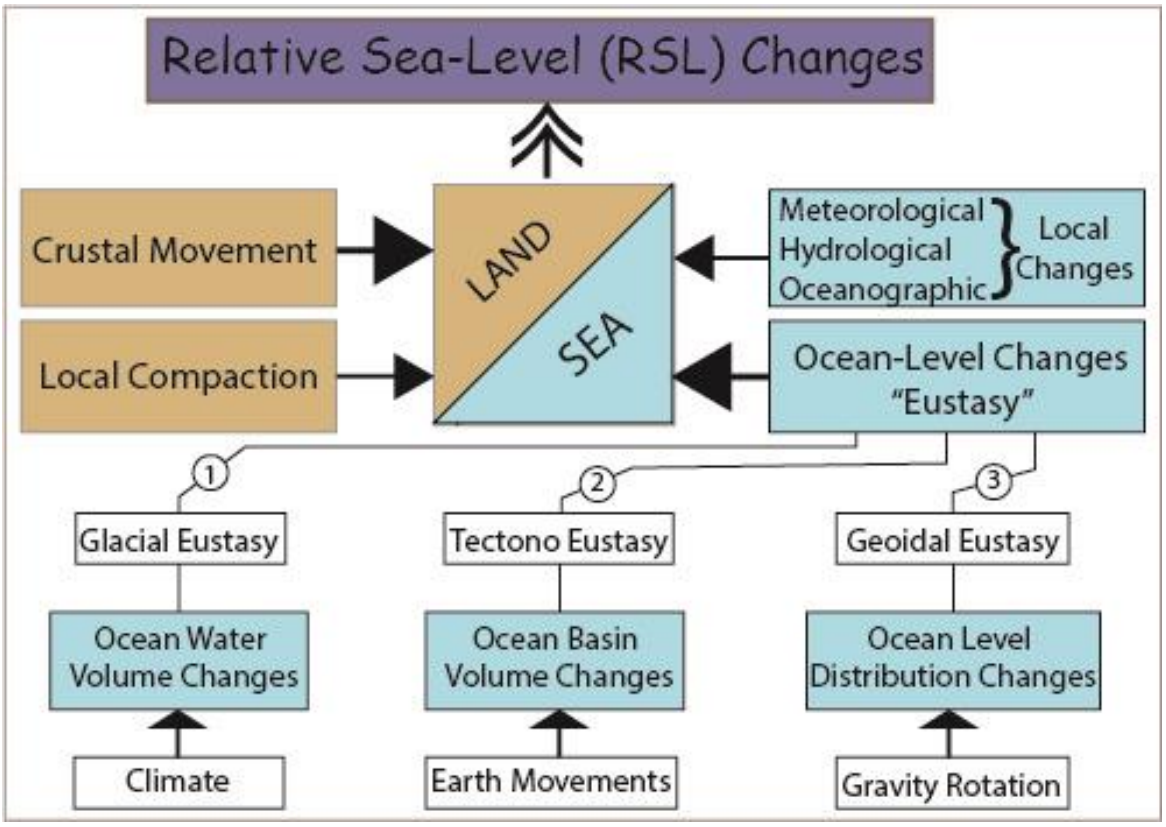

Figure 1.3: RSL change is the outcome of the changes of land and sea. The land is influenced by crustal movements (dominantly), and local compaction. Apart from the contribution from local meteorological, hydrological, oceanographic changes, the sea is mainly controlled by three types of eustasy, e.g., (1) glacial eustasy, (2) tectono eustasy, (3) geoidal eustasy. Modified from Mörner (1976) and Anundsen and Fjeldskaar (1983).

RSL change, in tectonically stable regions, is mainly a function of altering ice volume and Earth's response to the exchanging ice-water load (Lambeck et al., 2014). The eustatic sea-level

rise can also be inferred from a tectonically active site by adjusting for the land uplift or subsidence rate, given that it is stable over long timescales (Bard et al., 1996). Since there remains little tectonic activity in Norway (Svendsen and Mangerud, 1987), this is not an important RSL component here. However, Norway and other places that were covered with ice during the LGM still has a different sea-level history than the eustatic sea-level curve shown in figure 1.2. After the deglaciation, such areas experienced a glacio-isostatic rebound, unlike the far-field sites. Thus, after the LGM, when the large ice sheets and glaciers were melting away, Scandinavia experienced RSL change mainly due to glacio-isostatic rebound, global sea-level change, and geoid deformation (Svendsen and Mangerud, 1987), with smaller contribution from hydro-isostasy (figure 1.4).

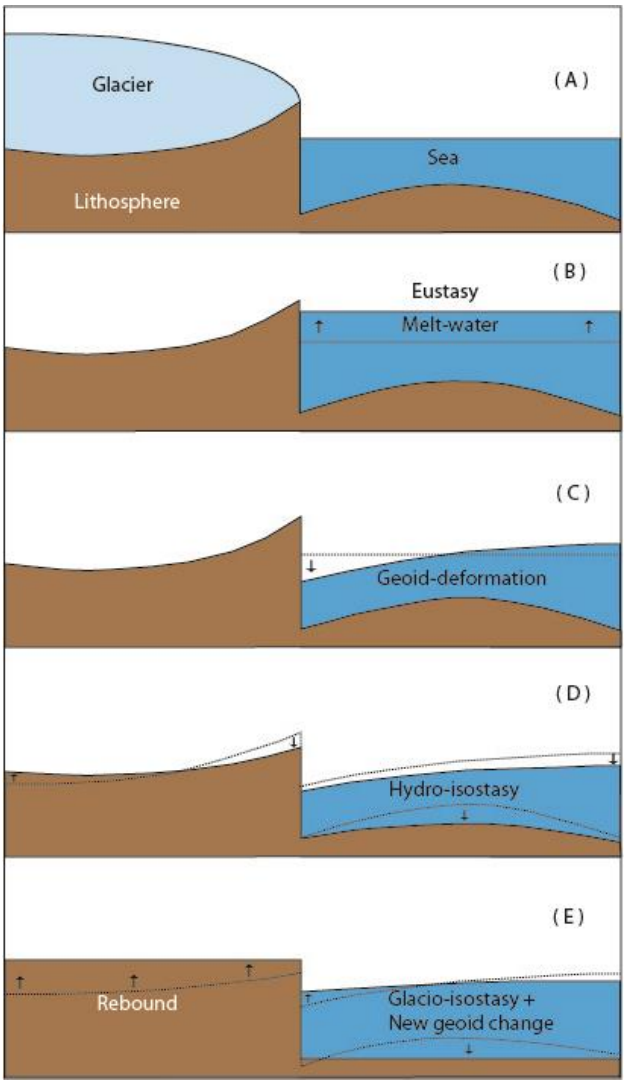

Figure 1.4: Illustration of sea-level change associated with deglaciation: (A) before the melting of ice, (B) glacio-eustatic sea-level rise with the increase of meltwater. (C) loss of ice's attraction on water results geoid deformation, (D) added weight to the ocean causes hydroisostatic lowering, (E) weight removal due to melting causes uplift in the continental part. Modified form Anundsen and Fjeldskaar (1983).

1.3. The Rationale of the Study

The complete shore displacement history of Evenes has not been studied in detail in the past, and the first isolation basin study was performed by Lid (2019). From the area of Lofoten and Vesterålen, further west from Evenes, some shore level displacement curves were constructed during the twentieth century. Marthinussen (1962) examined driftwood and dated them to establish a correlation with the past shorelines and constructed a shore-level displacement curve for Ramså at Andøya, where he proposed four stages of transgression during the Holocene. However, using different types of raised shore features Møller (1984) constructed a Holocene shore level displacement curve from Nappstraumen, Lofoten, and found two transgressions instead of the four transgressions proposed by Marthinussen (1962). Vorren and Moe (1986) updated the curve (figure 1.5) combining the results of Marthinussen (1962) and Møller (1984), and examining the peat layer found in sediment core retrieved from below the present tide level. Finally, Midtun (2019) studied an isolation basin close to the maximum Tapes level in Leknes, close to Nappstraumen, and found evidence of only one transgression phase.

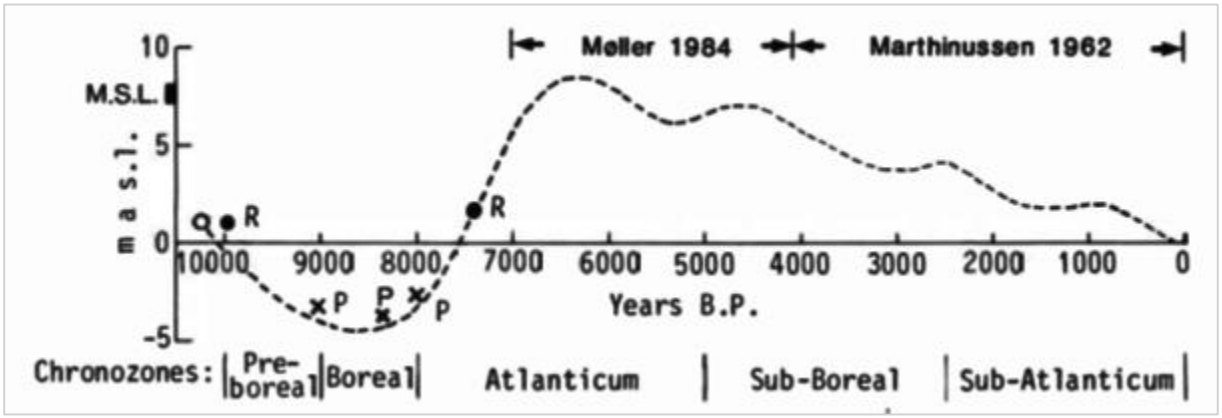

Figure 1.5: Shoreline displacement curve that covers Lofoten and Vesterålen archipelago (Vorren and Moe, 1986).

A sea-level curve from Sandstrand (figure 1.6), 11.71 km (distance measured from projection plane perpendicular to isobases from Pålsvatnet, fig. 1.7) away from Evenes, was constructed by Møller (1989). The curve was drawn based on a single local sea-level index point, combined with a regional sea-level model for all of Northern Norway constructed from raised beach ridges and marine terraces. The local sea-level index point came from an exposed marine terrace found at 16.5 m a.s.l. in Sandstrand, and a marine shell (*Artica islandica*) was collected and dated for the reference age of the terrace (Møller, 1989).

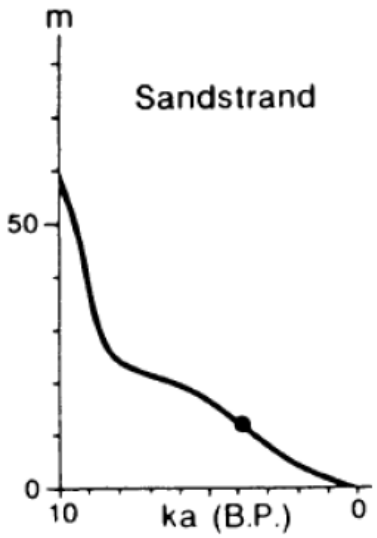

Figure 1.6: Shore-level displacement curve for Sandstrand (Møller, 1989).

Along with the sea-level index point from Møller (1989), Lid (2019) updated the curve for Skånland area, located to the north of Evenes. Lid (2019) added two data points from Svartvatnet and Store Trøsevatnet. Although the Svartvatnet data point was found representative of the sea-level curve as an isolation contact was discovered, the sea-level index point added from Store Trøsevatnet had a significant uncertainty in terms of altitude as no marine sediments was found in that basin.

RSL curves in Norway vary strongly based on location. For instance, the Tapes transgression, the local term used to describe a mid-Holocene transgression along the outer coast, is less evident or completely absent in further inland sites where the ice sheet was thicker, and the glacio-isostatic rebound is higher. In the shore level displacement curve constructed by Møller (1989) and Lid (2019), the mid-Holocene Tapes transgression was absent in the area of interest. Through this study, it is expected to add a data point from Pålsvatnet, an isolation basin of the Evenes area, to make the curve more precise for this mid-Holocene period, to see how much the rate of emergence slowed down during this period.

The marine limit map constructed by the Geological Survey of Norway (NGU) shows the estimated highest sea-level following deglaciation for any given area. NGU suggests a marine limit for the Evenes area of about 75 m. As per the Younger Dryas isobases, the study area is located in between the 60 m and 80 m isobases (figure 1.7). This area, however, was covered by ice during the Younger Dryas (Bergstrom et al., 2005) and thus, these isobases are not

directly indicative of the marine limit, only a maximum limiting estimate. Therefore, more data is required to reconstruct the postglacial sea level of Evenes.

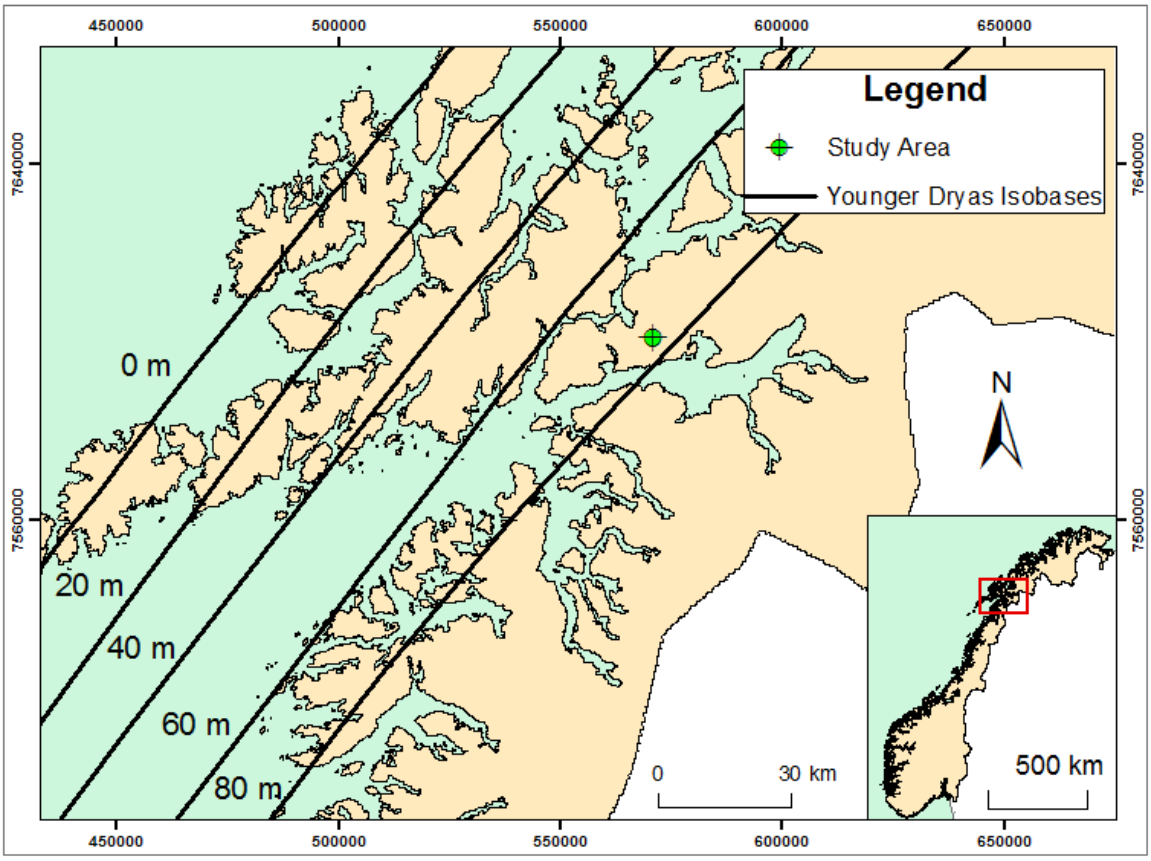

Figure 1.7: The study area is located between 60m and 80m Younger Dryas isobases. Modified from Møller (1989), the shapefile of Norway was downloaded from Hijmans (2020).

Following the Younger Dryas, only the Tapes shoreline has been mapped in detail for the Lofoten and Vesteålen region (Rasmussen, 1984), so a complete Holocene shoreline diagram, which shows the age, and tilt of shorelines (Svendsen and Mangerud, 1987), has not previously been constructed for the study area. However, considering the new RSL curve from this study and the shore-level displacement curve for Leknes, Vestvågøy (figure 1.8), it is possible to draw a shoreline diagram for the area between Leknes and Evenes, which may reflect an overview of the RSL change that occurred during the Holocene in this region.

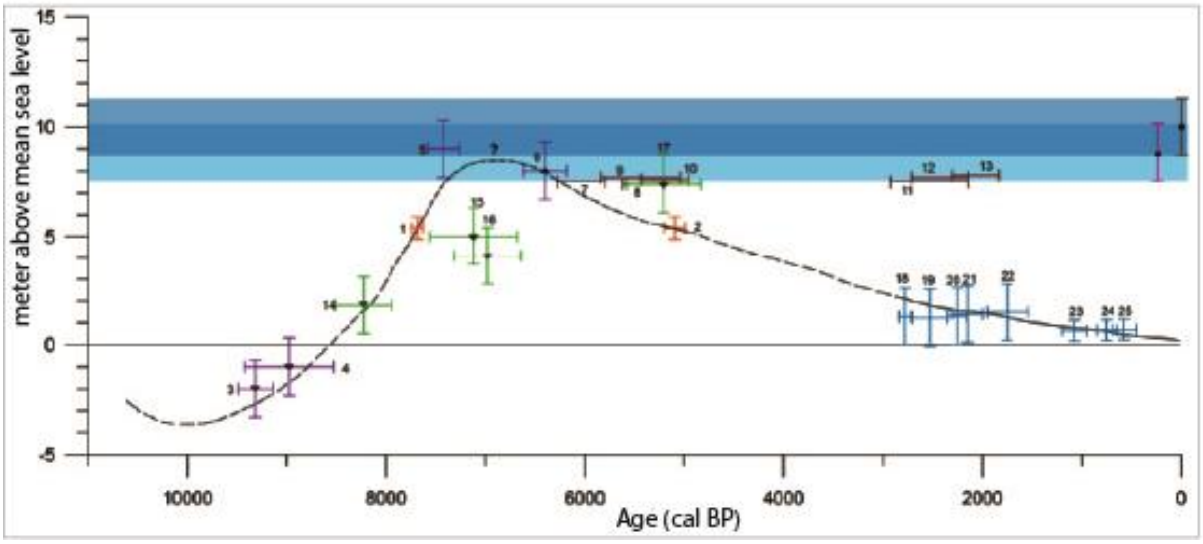

Figure 1.8: Sea-level diagram of Leknes, Vestvågøy (Midtun, 2019).

Finally, this study is significant for getting a rough estimate of the land uplift that occurred throughout the Holocene in the study area., which can be useful as an empirical constraint for models of glacial isostatic adjustment (Barnett et al., 2015; Peltier et al., 2015)

2. Study Area

2.1. Lake Setting

Pålsvatnet lake (figure 2.1), which is currently located 23.74 m above sea level (altitude of the threshold), is the main focus in the present study. However, to determine the threshold of Pålsvatnet, the adjacent Kjerkhaugvatnet lake (figure 2.2) is also taken into consideration as they share the same outlet threshold (see chapters 3 and 4). A relative sea-level curve for Skånland, the adjacent municipality, was drawn by Lid (2019), where results from Store Trøsevatnet and Svartvatnet basins were included. One of the aims of the present study is to update the sea-level curve, including the results from the Pålsvatnet. In figure 2.2, all the basins mentioned above are shown. Administratively, Pålsvatnet and Kjerkhaugvatnet are found in the Evenes Municipality (Kommune) in the Nordland county of Norway. On the other hand, Store Trøsevatnet and Svartvatnet are situated in Tjeldsund Municipality of Troms and Finnmark (Troms og Finnmark) county. The study area is located at the border of the two counties and the two municipalities of northern Norway.

Figure 2.1: Overview picture of the Pålsvatnet lake. The image was captured while the raft was in the middle of the lake. (Photo: Mohib Billah).

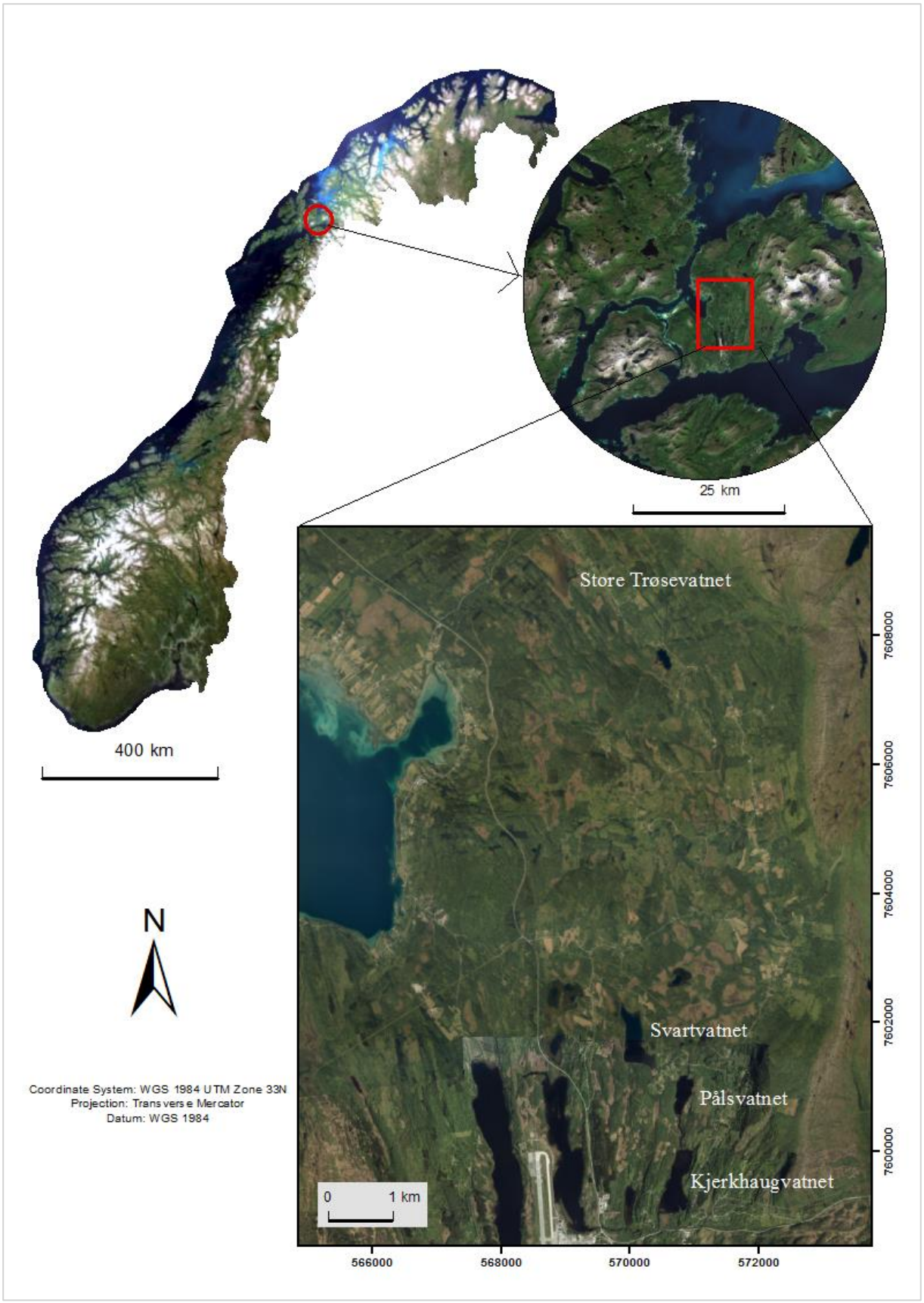

Figure 2.2: Overview map of the location of the basins used in the present study.

2.2. Climate and Tidewater

The climate of a place is determined based on weather data of an area for a standard period of 30 years. From the climate data, it is understood the average weather conditions and variability in that particular area. Considering the period of 1971 - 2000 for the Evenes region, the annual average temperature and precipitation were 3.6 ^{o}C and 998 mm (Norsk-Klimaservicesenter, 2020). This average data was found from the average of three surrounding weather stations, e.g., Liland, Eveneskjer, Gratangen, of Evenes Municipality (Norsk-Klimaservicesenter, 2020).

Relative sea-level change takes place several times a day as a result of tidal changes. The revolution of the moon around the Earth and the Earth's revolution around the sun are the main factors to create sufficient force to keep the tidal system active (Bills and Ray, 1999). Meteorological factors, e.g., air pressure, and wind pattern, may contribute to the tide levels. For example, if there remains high air pressure, due to the inverted barometer effect (IBE), water level remains low (Richter et al., 2012), and vice versa for low pressure. Along the Norwegian coast, meteorological factors may contribute up to 1 m of water level in addition to the astronomical tidal factors (Kartverket, 2019). Thermohaline variability may also contribute to changes in sea level that could be quantified from the instrumental data (Richter et al., 2012). It is crucial to consider the tidal limit while studying the sea-level change using isolation basins since the isolation basin may get saline water from high tides even after its threshold is raised above mean sea level (Sherman et al., 1996). However, the exact tidal level that the marine-lacustrine transition (isolation contact) in an isolation basin corresponds to, also known as the indicative meaning, is not entirely certain. Some authors have used the highest astronomical tide (HAT) as indicative meaning (Lohne et al., 2007), whereas, others have used the mean high water spring tide (MHWST) (Shennan et al., 2000; Shennan et al., 2018; Vasskog et al., 2019). In the present study, MHWST (table 2.1) is considered the tidal level corresponding to the isolation of Pålsvatnet, as the basin was probably sheltered from large waves during its isolation phase. The mean sea level from 1996 to 2014 is used as the zero reference point in this study, i.e. the 0-level in the final RSL curve.

Table 2.1: Different vertical datum and the relationship among them in Evenes Kommune (Nordland) with reference level Mean Sea Level (MSL) from 1996 to 2014 (Kartverket, 2020)

Vertical Datum	Altitude from mean sea level (1996 -2014)
Highest Astronomical Tide (HAT)	1.96 m
Mean High Water Spring Tide (MHWST)	1.34 m
Mean High Water Tide (MHWT)	0.99 m
Mean High Water Neap Tide (MHWNT)	0.64 m
Reference level NN2000	0.14 m
Mean Low Water Neap Tide (MLWNT)	-0.64 m
Mean Low Water Tide (MLWT)	-0.99m
Mean Low Water Spring Tide (MLWST)	-1.34 m
Lowest Astronomical Tide (LAT)	-1.83 m

2.3. Geological Setting

2.3.1. Bedrock

In the case of studying sea-level change from an isolation basin, information of the bedrock of the area is significant as the eroded bedrock material from the basin catchment will be deposited in the basin. During an isolation phase, it is expected that the source of minerogenic sediments changes from material transported into the basin by ocean currents to material washed in from the catchment. It is seen from the mapping (figure 2.3) of the Geological Survey of Norway (NGU) that the surrounding area of the lake is dominated with carbonate-based bedrock. This may potentially create a hard water effect for radiocarbon dating of any aquatic sample retrieved from the basin (Shotton, 1972). Due to the hard water effect, the age of aquatic samples would be overestimated, and to avoid such a problem, only radiocarbon samples with a terrestrial origin should be used from Pålsvatnet, This will also be discussed briefly in chapter 3.

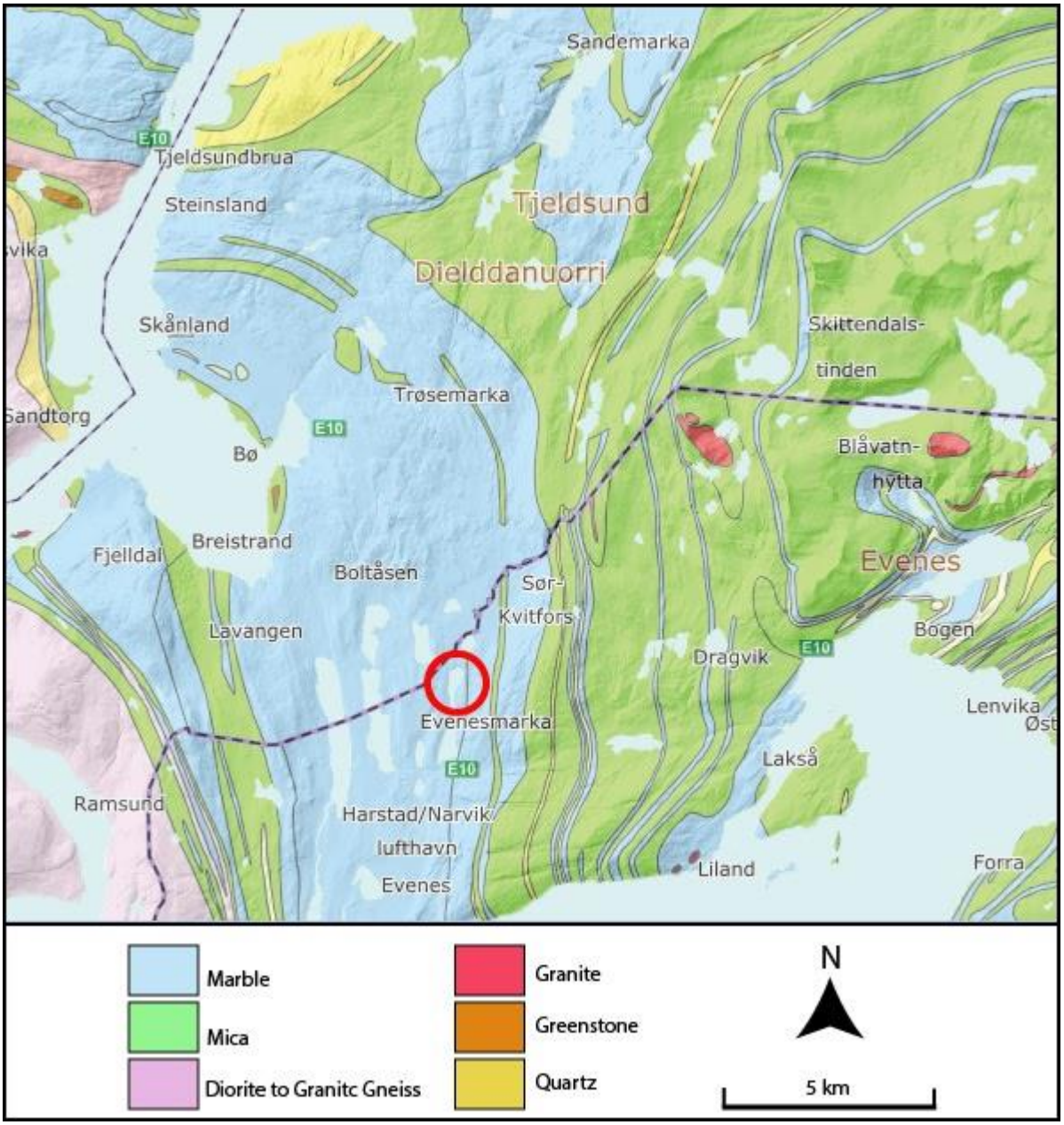

Figure 2.3: Bedrock map of the surrounding area of Pålsvatnet (marked with red circle). Modified from online map services of NGU (2020b).

2.3.2. Superficial Deposits

From the superficial deposits map (figure 2.4), it is observed that the surrounding area of Pålsvatnet is dominated by weathered material as per the mapping of NGU. As part of this study, a glaciofluvial delta (figure 2.4) was investigated in more detail, and a quaternary geological map was produced, with a focus on the extent of marine deposits. The Quaternary geological map will be presented in chapter 4, where some deposits have been reinterpreted from the NGU map (figure 2.4).

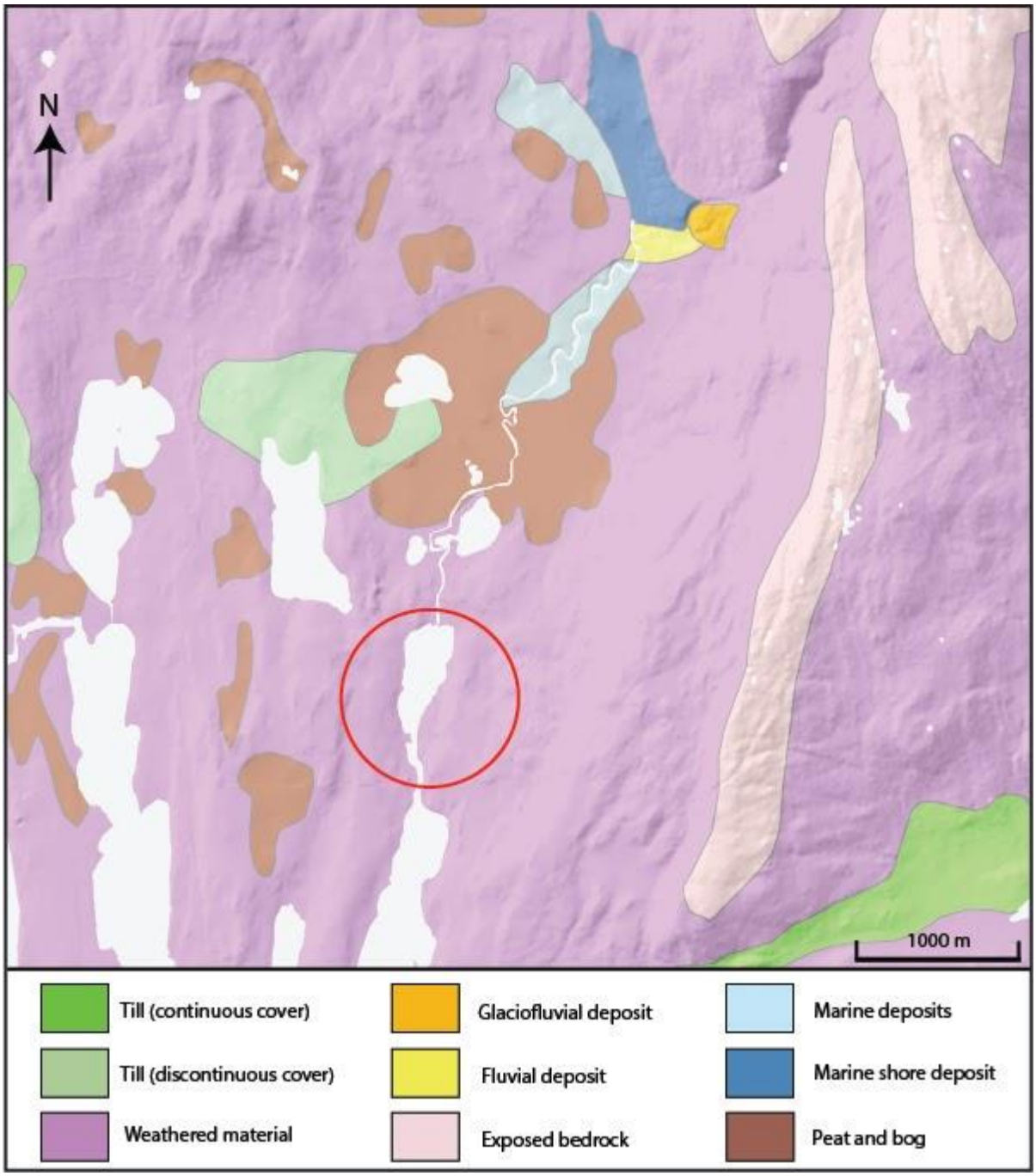

Figure 2.4: Superficial deposit map of Pålsvatnet and its surrounding area. The lake is marked with a red circle on the map, modified from the online map services of NGU (2020c).

2.4. Paleoclimate and Deglaciation History

Glaciers began expanding both in northern Europe and most of the glacial parts of the Earth from the beginning of the Quaternary (Ramberg, 2008: 483), the geological period that started about 2.6 million years ago (Dutton et al., 2015). The Pleistocene and the Holocene are the two

epochs of the Quaternary period, and the global sea-level was fluctuating due to numerous glacial and interglacial events throughout the Pleistocene. The Eemian (known as the 'Sangamonian' in North America), lasting from ~130,000 - ~116,000 years ago, was the last full interglacial (Arctic temperature was 3^0C - 5^0C above than the present) that occurred during the Pleistocene epoch. During the Eemian, eustatic sea-level was about 6 – 9 m higher than the present-day sea level (Gornitz, 2013: 102; Dutton et al., 2015). The Weichselian, which began after the Eemian, was the last glacial period when the eustatic sea-level dropped to some remarkable lowstands. Around 25000 calibrated radiocarbon years before present (cal BP), during the period of the last glacial maximum (LGM), the Eurasian ice sheets reached their maximum Weichselian extent (figure 2.5) when the global sea level was around 130 m lower than the present (Lambeck et al., 2014). When ice-sheets started retreating after the LGM, the sea level began to rise, and the rate accelerated during the Bølling-Allerød interstadial (around 14700 - 12800 cal BP) during the rapid eustatic sea-level rise that is also known as Meltwater Pulse 1A (Gornitz, 2013: 125). In some areas, a very short period of glacial re-advance is observed between the Bølling and the Allerød interstadials known as Older Dryas (OD) (Mangerud et al., 1974). Younger Dryas (YD) was the last stadial of the Weicheselian (and the Pleistocene epoch) that lasted around 1200 years until ~11600 cal BP, when glacial re-advance occurred over much of Europe probably due to the disrupted thermohaline circulation in the North Atlantic (Teller et al., 2002; Benn and Evans, 2013: 20). The Holocene, the current epoch of the geological time scale, started just after the Younger Dryas at the end of the Pleistocene epoch, which is the main focus of this study. During the earliest part of the Holocene, the current interglacial, the Earth experienced continued glacial retreat and eustatic sea-level rise in general (Lambeck et al., 2014). The Holocene is further subdivided into the Early (11700-8200 cal BP), middle (8200-4200 cal BP), and Late Holocene (4200 cal BP until present) (Walker et al., 2019). During the Middle Holocene, eustatic sea-level stabilized, and has remained fairly stable until the modern increase observed at present.

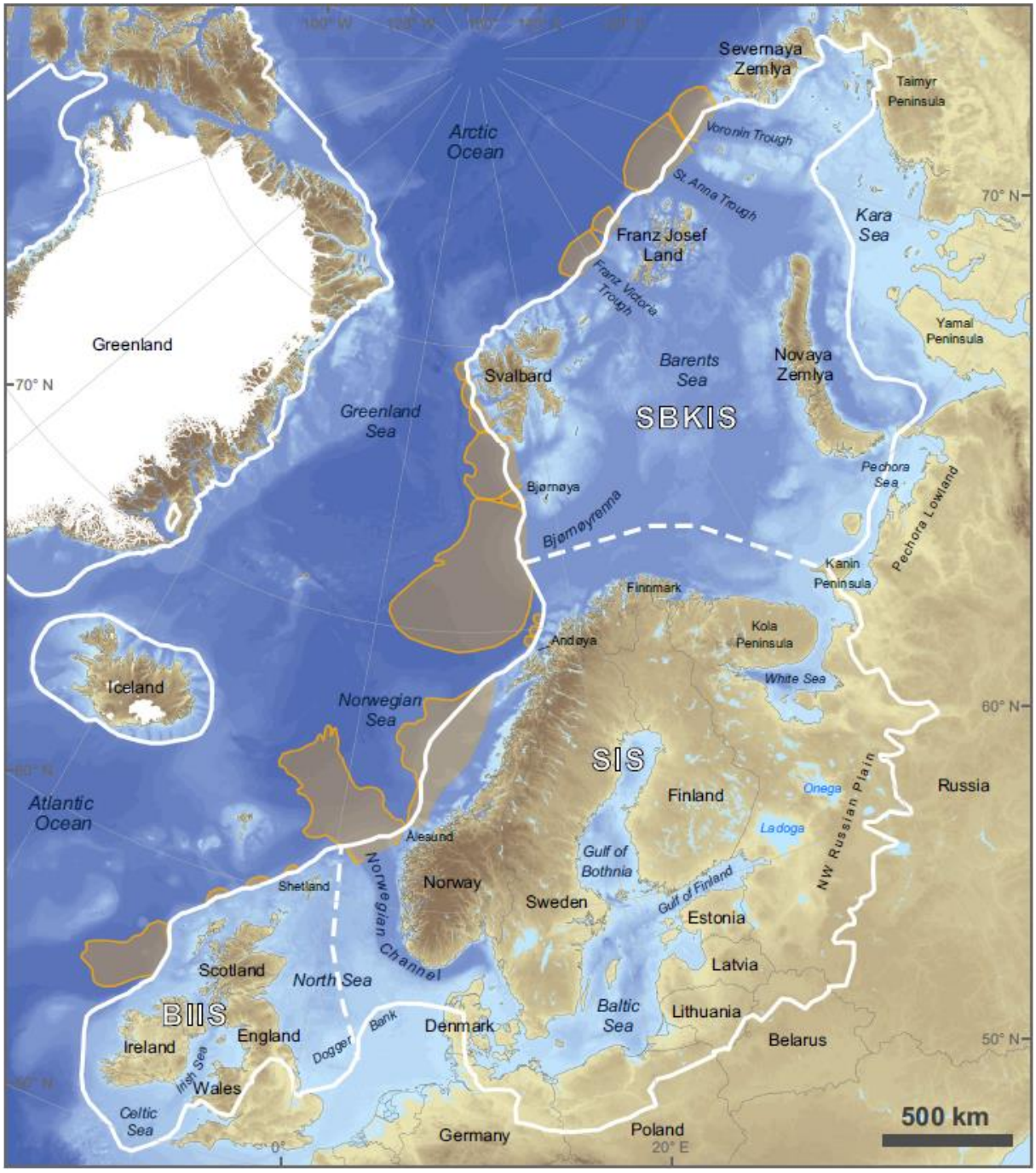

Figure 2.5: Map showing the maximum extent of the ice sheet during the last glacial maxima. Approximate boundaries of the three Eurasian ice-sheets: SBKIS = Svalbard-Barents-Kara Ice Sheet; SIS = Scandinavian Ice Sheet; BIIS = British-Irish Ice Sheet; are shown with dashed lines (Hughes et al., 2016).

Most of Scandinavia was covered by the Scandinavian ice sheet (SIS) during the last glacial maximum (LGM) (Hughes et al., 2016). After the LGM, the SIS retreated, although with some glacial re-advance events which could be dated from marginal moraines, for example, the Tromø-Lyngen (T-L) moraine of northern Norway (Bergstrom et al., 2005), the Herdla-Halsnøy moraine of western Norway (Lohne et al., 2012), and the Ra moraine of southern and eastern

(Ramberg, 2008: 518; Romundset et al., 2019), which all are interpreted to represent the maximum extent of the YD ice re-advance. During the YD relative sea-level stabilized over large parts of Scandinavia, whereas western Norway even experienced a transgression (Lohne et al., 2007), which has resulted in distinct shorelines from this period (Bergstrom et al., 2005). Olsen (2002) found that readvances of the SIS occurred around 22 ^{14}C k BP (LGM), 16 ^{14}C k BP (Oldest Dryas), 12.2 ^{14}C k BP (Older Dryas), and 11-10 ^{14}C k BP (Younger Dryas) in the area northwest of Svartisen, Nordland, northern Norway (located further south of the study area of this research). Hinnøya, located northwest of the study area, was ice-free during the Allerød interstadial (Bergstrom et al., 2005). However, due to the glacial re-advance during the YD, the study area (a bit south of Skånland in figure 2.6) was ice-covered, as can be confirmed from its position inside the margin of the T-L moraine (Bergstrom et al., 2005).

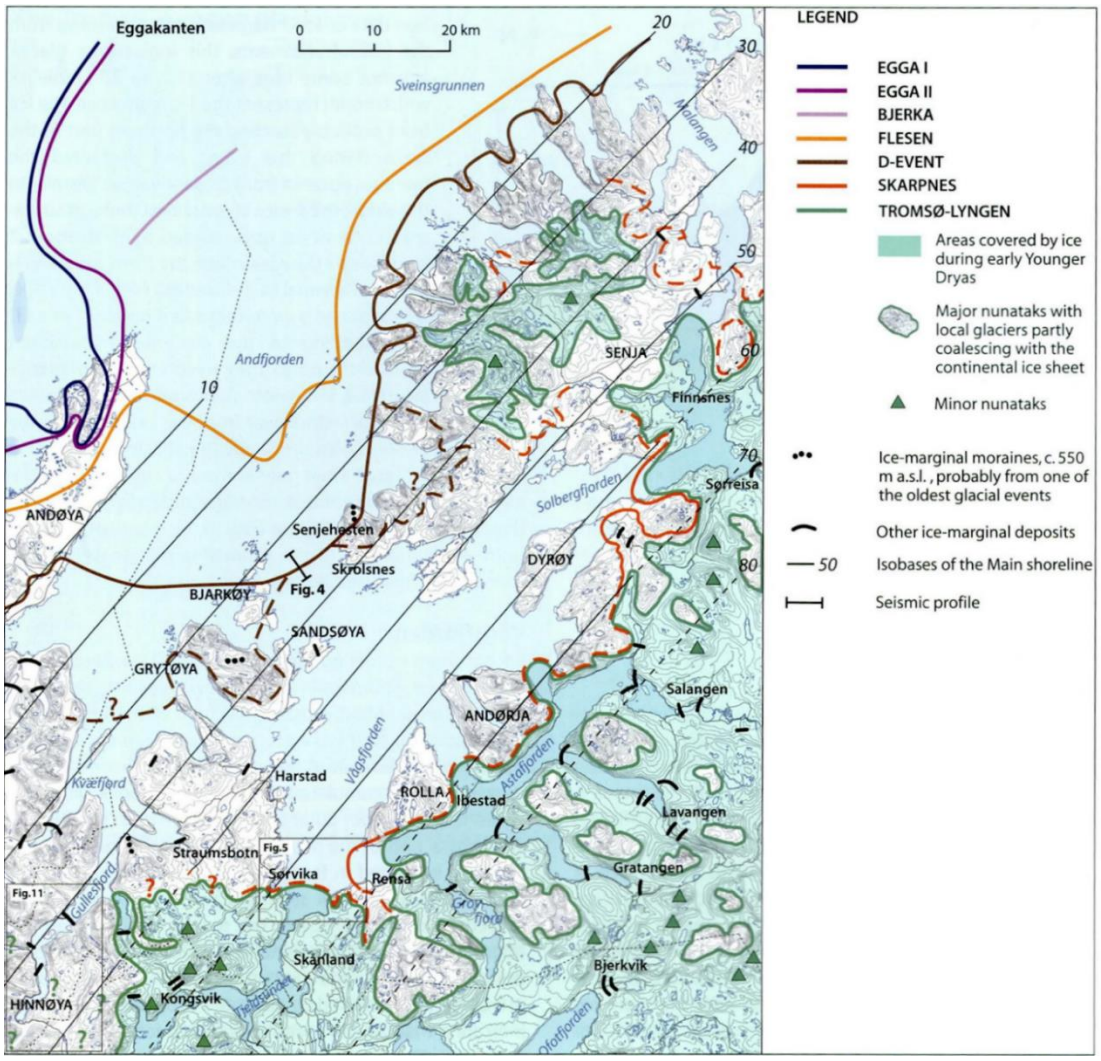

Figure 2.6: Ice-marginal events in the Andfjorden-Vågsfjorden area. The area of interest of the present study is located just under Skånland within the areas covered by ice during the early Younger Dryas (Bergstrom et al., 2005).

With the inception of the Holocene epoch, the area became ice-free rapidly just after the YD, as is evident from the Balsfjord glacier of Troms that quickly retreated from the T-L moraine around 10.4 ^{14}C k BP (Forwick and Vorren, 2002). Throughout the Holocene, the net eustatic sea-level has been rising while the trend of relative sea-level change has been negative for most of Scandinavia due to isostatic rebound. Although the Holocene is considered as a warm interglacial period, there remain some fluctuations in the climate. Cool and maritime climatic conditions prevailed in northern Norway during the Early Holocene, which was interpreted from the dominance of ferns and lycopods in birch woodlands (Vorren and Moe, 1986). A climatic optimum (hypsithermal) occurred in the Middle Holocene when the temperature was higher than present, succeeded by a gradual cooling (Eldevik et al., 2014).

3. Methodology

3.1. Isolation Basin Analysis

Relative sea-level (RSL) change, or shoreline displacement, is the result of vertical adjustment of the sea surface and/or the landmass. After the retreat of the Scandinavian ice sheet and small glaciers, Fennoscandia experienced a glacio-isostatic rebound, and as a result, many isolation basins are found here (figure 3.1). Isolation basins are natural depressions situated below the postglacial marine limit that have been isolated from the sea due to changes in relative sea level (Long et al., 2011; Romundset et al., 2018). The elevation of a basin threshold provides a stable sea-level index point that represents the palaeo-shoreline (mean high-tide sea level) at the time of isolation (Balascio et al., 2011; Romundset et al., 2018). Contrary to sea-level reconstructions from salt marshes (Barnett et al., 2015), sediment compaction does not create any problem in isolation basin studies, as the position of the sea level is associated with the basin threshold (Svendsen and Mangerud, 1987). However, it is recommended to use basins that have an outlet over a bedrock threshold to avoid interpretive problems due to possible erosion of the outlet (Kjemperud, 1986; Svendsen and Mangerud, 1987; Romundset et al., 2018). Moreover, basin stratigraphy can also record any extreme events, e.g., landslides or tsunamis that have occurred in the area (Lohne et al., 2007; Long et al., 2011). It should also be noted that such events can disturb the stratigraphy of an isolation basin, making it more challenging to interpret.

3.1.1 Isolation/Ingression Contact

The term ‘isolation contact’ is widely used by Scandinavian scientists as the boundary in the sediment core representing the time when the lake was isolated from the sea (Kjemperud, 1986). While the Anglo-American scientists often use the term ‘marine/lacustrine boundary’ as a synonym of it, the term ‘isolation contact’ is preferred here as it refers more precisely to the end of the brackish phase that will often be recorded between the marine and lacustrine phase (Kjemperud, 1986). An isolation contact is thus the stratigraphic boundary where marine/brackish sediments are overlain by lacustrine sediments due to the fall of relative sea level. If, on the other hand, the lake is inundated by seawater due to rise of relative sea level, we will get marine sediments deposited on top of lacustrine sediments, and this boundary is called an ingression contact (Lohne et al., 2007; Long et al., 2011; Romundset et al., 2018; Vasskog et al., 2019). Lithostratigraphic indicators are often useful to recognize the isolation-

and ingression contacts; however, for a more precise and robust identification of the transition, biostratigraphic indicators (e.g. diatoms, macrofossils or microscopic phytoplankton) are often required (Vasskog et al., 2019).

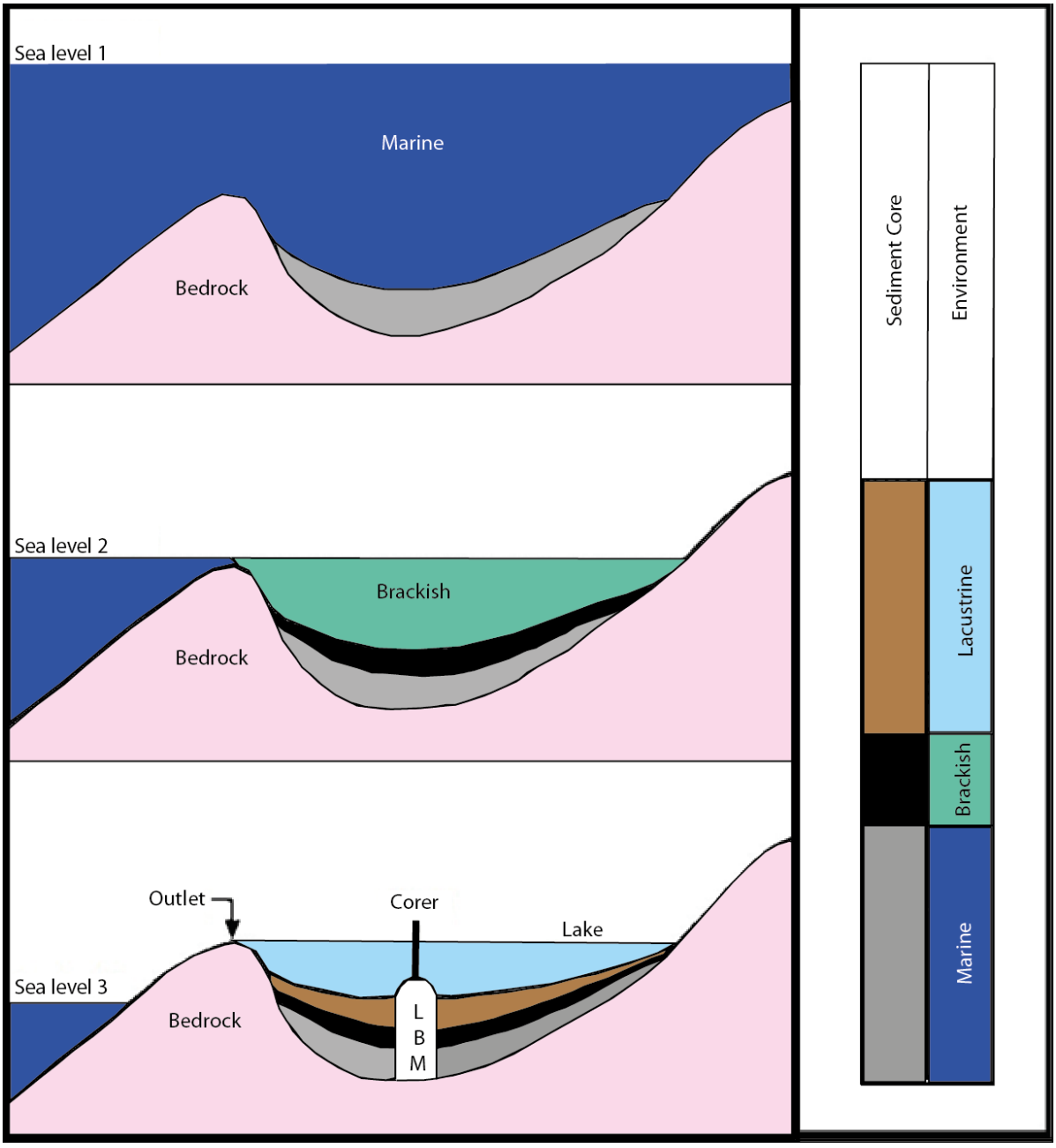

Figure 3.1: Sketches of an isolation basin at three different points in time: (1) sea level was well above the basin threshold, (2) when sea level was at the threshold, (3) when sea level is below the threshold. Right column: a typical core sequence along with depositional environment. Modified from Svendsen and Mangerud (1987).

Kjemperud (1986) developed a conceptual framework of four ‘contacts’ (figure 3.2) in the sediments throughout the process of isolation. Such ‘contacts’ can in principle be slightly separated in time, and therefore also stratigraphically, in a protected lake with minimal storm influence. These are:

The sedimentological isolation contact is the change from a minerogenic mostly allochthonous sediment to a more autochthonous organic deposit. This contact often takes place before other contacts and found below them in the stratigraphic sequence.

The diatomological isolation contact is also more generally known as the phytological isolation contact**.** It occurs when the water in the photic zone, the surface layer of a basin that gets sunlight, becomes fresh. As the photic zone becomes dominant with freshwater, freshwater diatoms and phytoplankton are deposited during that phase, which is helpful to mark a paleoenvironmental horizon.

The hydrological isolation contact describes the total cessation of marine incursions into the basin. This may coincide with diatomological contact as heavier saline water can flow in and out under the photic zone during the high tide.

The sediment/freshwater contact is the boundary when all trapped seawater is cleaned out. Such contact is found in deep basins with trapped seawater, and in some deep lakes of Norway, trapped seawater is even found today (Strøm, 1957).

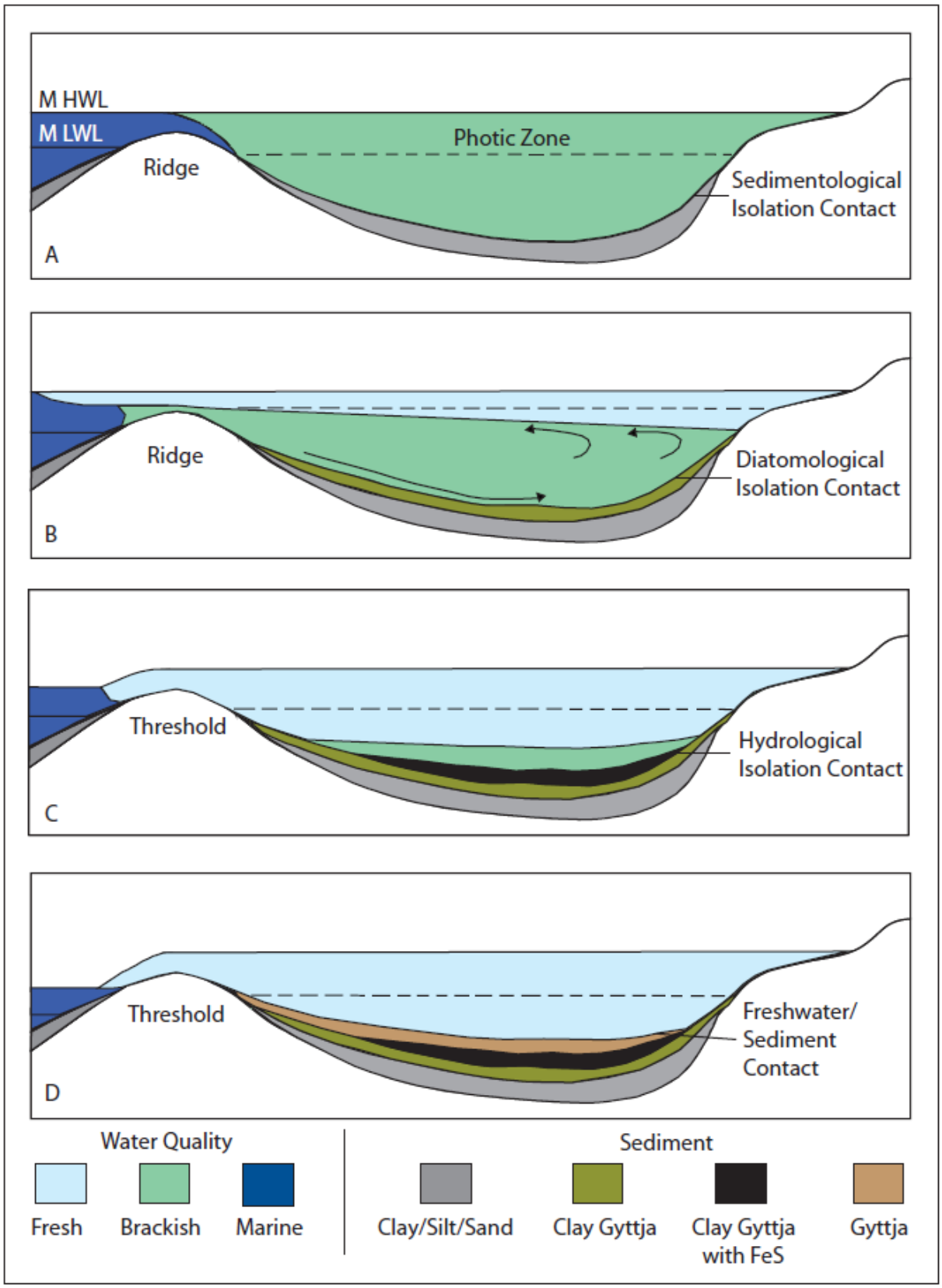

Figure 3.2: A conceptual sketch of the four 'contact' throughout the process of isolation. MHWL = mean high water level, MLWL = mean low water level. Modified from Kjemperud (1986).

3.2 Field Methods

3.2.1. Bathymetric Survey

A bathymetric survey of the lake is a vital part of selecting the most suitable site for the coring. Generally, it is better to collect the sediment sample from the deepest part of the lake as it will usually provide a more high-resolution stratigraphic sequence than the shallow areas. The bathymetric survey was conducted by Pål Ringkjøb Nielsen and Josheph Michael Buckby in the summer of 2018. A Garmin GPSMAP 721xs echo sounder system was used to conduct the survey. An echo sounder measures the round trip time required for a pulse of sound from the vessel to the bottom of a lake (Christ and Wernli, 2014). Based on this two-way travel time, the echo sounder provides depth information for GPS points along transects with a certain sampling interval based on either time or distance. In this case a sampling interval of 5 seconds was used. After the vessel is run over the relevant portion of a lake with sufficient resolution (e.g., GPS tracks in figure 3.3), the depth points are suitable for generating a bathymetric map.

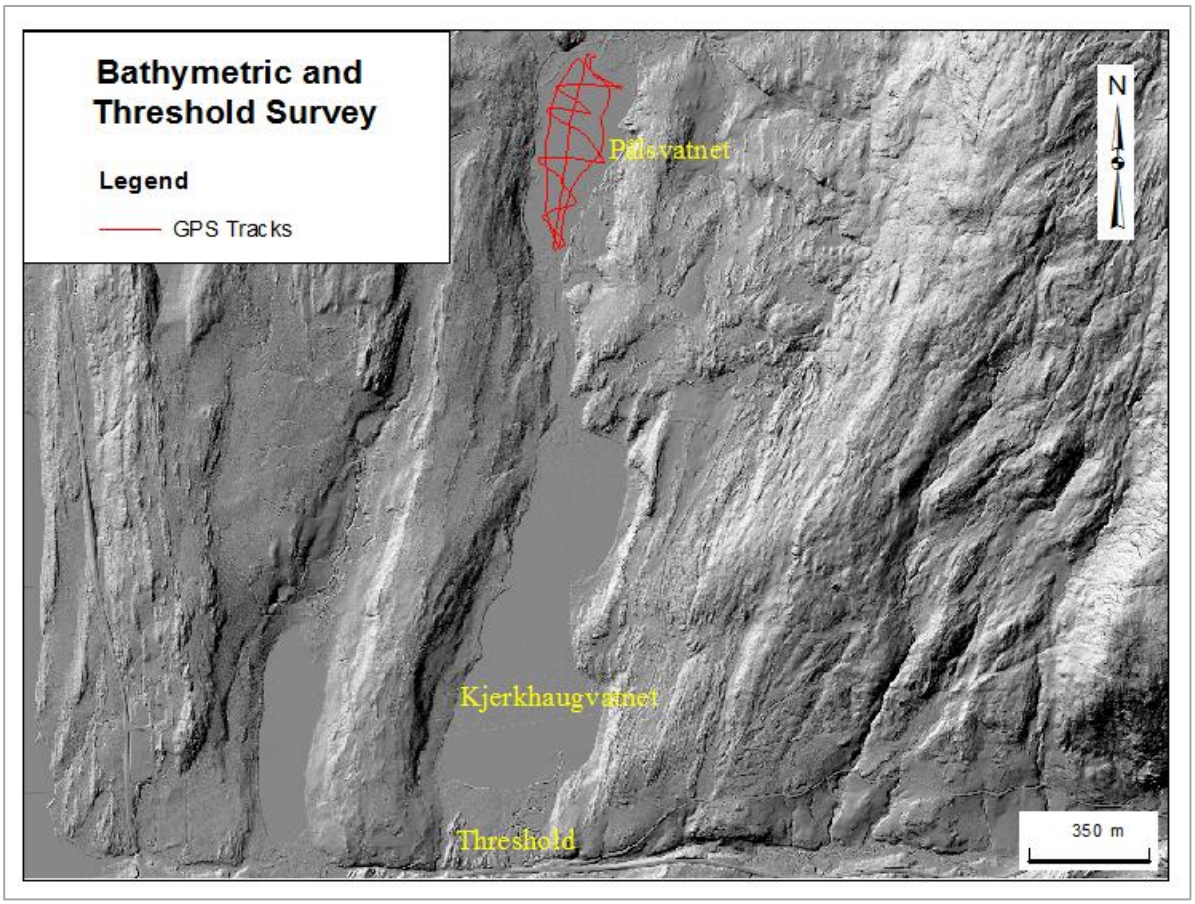

Figure 3.3: GPS tracks of the bathymetric survey of Pålsvatnet. The lake shares the same outlet threshold with the adjacent Kjerkhaugvatnet. The background hillshade map was prepared by using TIFF file of Geodata (2019).

3.2.2. Coring

Two sediment cores (PÅLP – 119 and PÅLP – 219) were retrieved from the deepest part of Pålsvatnet in March 2019. Coring was done by Svein Olaf Dahl, Kristian Vasskog, and Matthew James Jenkin, using a Piston corer from the lake ice (figure 3.4). The piston coring system (Nesje, 1992) that was used to retrieve the sediment cores, is able to collect cores up to 6 m in length. The retrieved cores were around 240 cm (PÅLP-119) and 310 cm (PÅLP-219) long, and the distance between the coring sites was about 50 m.

Figure 3.4: Lake Coring with piston corer (Photo: Kristian Vasskog).

3.2.3. Lake Outlet Threshold

The lake outlet threshold is essential for constructing the sea-level displacement curve as it gives us the altitude of the sea-level index point. A survey of the overall situation of the lake threshold was performed in August 2019. First, it was looked for the outlet threshold in the southern end of Pålsvatnet and discovered that the river between Pålsvatnet and Kjerkhaugvatnet (figure 3.3) is so deep that the actual threshold is located downstream of the next lake. An echo sounder was used to monitor the shallowest point of the river between the lakes to confirm that there was no local threshold out of Pålsvatnet. We then proceeded to look

for the outlet of the downstream Kjerkhaugvatnet. Boulders are sticking up at the outlet of Kjerkhaugvatnet (figure 3.5), and a stick was penetrated to measure the depth in between the boulders. The altitude of the boulder threshold is 24.3 m a.s.l., and we could penetrate the stick up to 32 cm; thus, the lowest altitude of the boulder threshold is 23.98 m a.s.l. Just downstream from the boulders, the water is flowing over bedrock (figure 3.5). The bedrock threshold is located approximately 49 m south from the boulder threshold. The altitude of the bedrock is 23.5 m a.s.l. The altitudes were determined from the LiDAR data using the points registered by GPS during the survey.

Figure 3.5: Boulders at the outlet of the Kjerkhaugvatnet (left), and lake threshold on bedrock (right) (Photo: Mohib Billah).

3.2.4. Mapping

The area around the lake was not mapped in detail, as there were no clear geomorphological indicators of sea level near the lake. The mapping area was selected because of the interesting deposits that indicate sea level. Geomorphological mapping of the area was done with a combination of aerial photographs (Norgeskart, 2019), LiDAR data (figure 3.6), and field data. The ESRI ArcMap version 10.6 software was used to combine information from these methods to reproduce a Quaternary geological map.

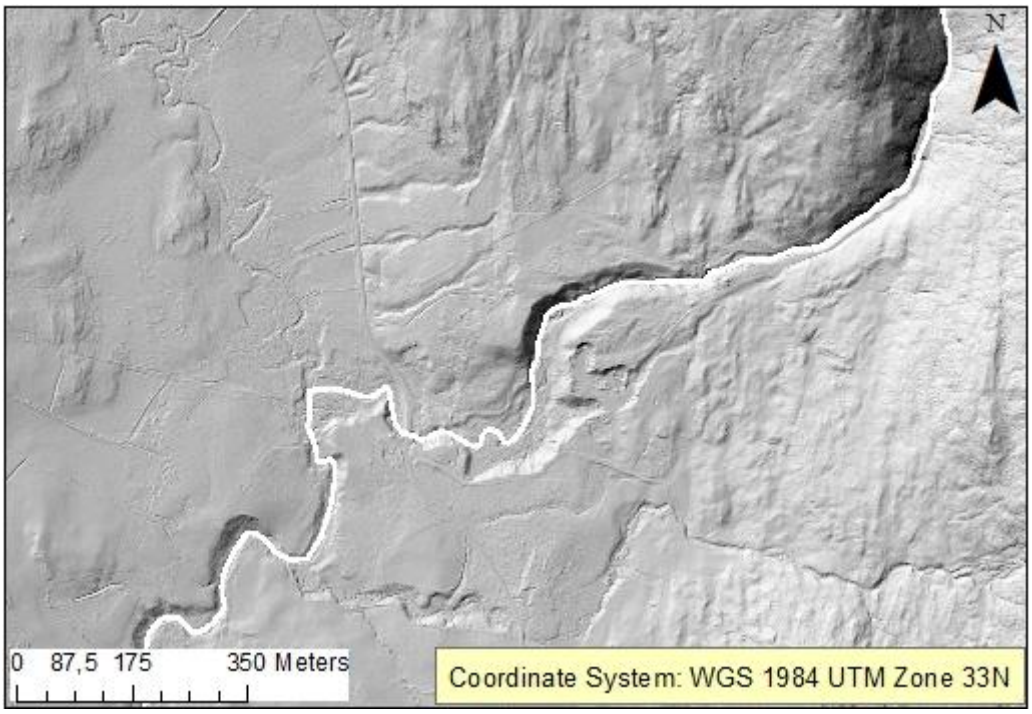

Figure 3.6: Hillshade map of the area included for mapping in the present study. TIFF file retrieved from Geodata (2019) was used to reproduce the hillshade map.

3.3. Laboratory Methods

3.3.1. X-Ray Fluorescence (XRF)

X-ray fluorescence (XRF) has been widely used for Earth and environmental sciences research as the involvement of its use has risen exponentially in research papers published since 2005 (Croudace and Rothwell, 2015). XRF core scanners have the capability to record high-resolution data, typically in the range from Aluminum (atomic number 13) to Uranium (atomic number 92), rapidly and non-destructively with minimum user intervention and very little preparation before analysis (Croudace and Rothwell, 2015). For this study, an ITRAX sediment core scanner, manufactured by Cox Analytical Systems, Mölndal, Sweden, at the sediment laboratory at EARTHLAB, University of Bergen, was used for the analysis of geochemical composition.

The ITRAX scanner also provides a high-quality RGB digital image using an optical camera (Croudace et al., 2006). After the core returned to the home position, 6µm polypropylene film was used to protect the core from drying during the analysis and the procedure was done after the core had reached room temperature to prevent moisture formation between the plastic film

and the sediment surface. The voltage and current was adjusted until the outgoing count rate was as close as possible to 30,000 cps, which in the case of PÅLP-119 core was 28 kV and 28 mA. Before starting the final scan, Batch analysis mode needs to be entered to define the core name and to review instrument count time and scan limits (Croudace et al., 2006). After the scan was completed, the data was processed with Qspec spectral analysis software for the ITRAX core scanner. The output data of ITRAX core scanner is considered semi-quantitative in nature as the outputs are normally the counts of different elements, not the actual concentration of the elements (Croudace et al., 2006).

One of the split halves of core PÅLP-119 was loaded onto the track of the machine with the top positioned towards the X-ray tube, and scanning was started with the help of software. The surface scan is done be defining kV and mA setting for the X-ray tube and core dimension to be scanned. With the help of a surface laser scan, it is ensured that the XRF detector follows closely sediment surface for any subsequent positioning of the XRF detector (Croudace et al., 2006).

3.3.2. Magnetic Susceptibility (MS)

Volume magnetic susceptibility is the measurement of the concentration of magnetizable material per unit volume which refers to how easily a substance can be magnetized, and this is a dimensionless parameter (Gunn and Best, 1998; da Silva and Boulvain, 2006). The volume magnetic susceptibility (k) is defined as:

$$k = \frac{\mathrm{M}}{\mathrm{H}}$$

Here, M is the magnetization intensity per unit volume generated by providing a magnetic field H (Gunn and Best, 1998; da Silva and Boulvain, 2006). k-values can be both negative and positive, where negative values reflect diamagnetic material, whereas paramagnetic materials have small positive values, and ferrimagnetic and ferromagnetic materials show up with medium and large positive values, respectively (Gunn and Best, 1998; da Silva and Boulvain, 2006). Commonly, increased MS values are seen in marine conditions where there is more supply of minerogenic sediments and less input of biogenic materials (Strunk et al., 2018). However, MS will vary with sediment source, and this changes when the basin changes from marine to lacustrine. On the basis of mineral composition of marine and lacustrine sediments, the MS value may therefore increase or decrease either way. It is also possible to measure mass-

specific magnetic susceptibility (χ) which is expressed in m^3/kg (da Silva and Boulvain, 2006; Gunn and Best, 1998), although this requires samples to be extracted from the core. In this study, volume magnetic density was used since we preferred the non-destructive scanning method.

Measurement of MS was done in the magnetic susceptibility laboratory of the Department of Earth Science, University of Bergen. An MS2E point sensor was used for the open sediment cores covered with plastic film (Dearing, 1999). It was ensured that the core reached room temperature before scanning, as this can reduce the sensor drift significantly (Dearing, 1999). The measurements were done at 5 mm downcore intervals.

3.3.3. Radiocarbon Dating

Sample preparation for radiocarbon dating (Bradley, 2014: 59) was done at the EARTHLAB, University of Bergen. A total of six samples were collected from PÅLP-119 core, and sent to Poznan Radiocarbon Laboratory, Poland. While collecting samples, it was preferred to pick terrestrial macrofossil samples to avoid the calibration problem with marine reservoir age and hard water effect (MacDonald et al., 1987). This is particularly important due to the carbonate-rich bedrock in the field area (Chapter 2). The surface of the sediment core was cleaned before picking out a slice of 1cm thickness into a jar of water. Then the jar was placed in a shaker so that the sediment dissolved in the water. Afterward, sieving was done with 250µm and 125µm sieve sizes to pick the macrofossils. Finally, with the help of a stereo-microscope, the material was identified, and terrestrial macrofossils were kept for dating. After drying the sample overnight in the oven, the final weight measurement was done. The minimum weight required for radiocarbon dating varies depending on the type of sample. However, the Poznan Radiocarbon Laboratory, Poland, can provide robust radiocarbon dates from samples containing 1 mg or more of pure carbon, whereas uncertainties increase with a smaller amount of sample (PRL, 2020). If there were not enough terrestrial material from one single centimeter, another slice of one centimeter was added from above or below that point until enough material was found. The dating material includes *Betula pubescens* fruit, *Alnus glutinosa* fruit, *Betula nana* female catkin scale, *Pinus sylvestris* bud scale, leaf fragments, wood fragments, and twigs (Table 3.1) (figure 3.7). The datable materials which are not from terrestrial sources (e.g., *Daphnia* eggs, *Cristatella*, *Ruppia maritima* fruits) are excluded from dating; however, they are good indicators of depositional environment.

Table 3.1: Material collected for radiocarbon dating; species usually found in lacustrine sediment are referred with 'L' and species deposted during barckish/marine phase are referred with 'BM'.

Vial No.	Weight of dry sample	Depth	Included material	Other (not included)
1	10.5 mg	177.5 – 181.5	*Betula pubescens* fruit, *Alnus glutinosa* fruit, *Betula nana* female catkin scale, Leaf fragments, Wood fragments, Twig, *Conifer* needles	*Daphnia* eggs (L), *Cristatella* (L)
2	10.7 mg	221.5 – 223.5	*Betula pubescens* fruit, *Alnus glutinosa* fruit, *Betula nana* female catkin scale, *Pinus sylvestris* bud scale, Leaf fragments, Wood fragments	*Daphnia* eggs (L), *Cristatella* (L)
3	3.7 mg	229.5 – 230.5	*Betula pubescens* fruit, *Betula nana* female catkin scale, Leaf fragments, Wood fragments	*Cristatella* (L)
4	8.0 mg	233.5 – 234.5	*Betula pubescens* fruit, *Alnus glutinosa* fruit, Leaf fragments	*Ruppia maritima* fruits (BM)
5	3.0 mg	235.5 – 237.5	*Betula pubescens* fruit, *Alnus glutinosa* fruit, *Betula nana* female catkin scale, Leaf fragments, Wood fragments, Twig	*Ruppia maritima* fruits (BM)
6	3.7 mg	238.5 – 239.5	*Betula pubescens* fruit, *Alnus glutinosa* fruit, Leaf fragments, Twig	*Ruppia maritima* fruits (BM)

After getting the results of radiocarbon dating from the Poznan Radiocarbon Laboratory, Poland, the calibration was done using IntCal13, a terrestrial calibration curve of Reimer et al. (2013), and modelled with the 'clam' package of R software (Blaauw, 2010). To avoid the hard water effect, samples were selected with a terrestrial origin; as a result the reservoir effect was not required to take into consideration. According to the laboratory report from Poznan, all samples contained more than 1 mg of pure carbon.

a. *Betula pubescens* fruit

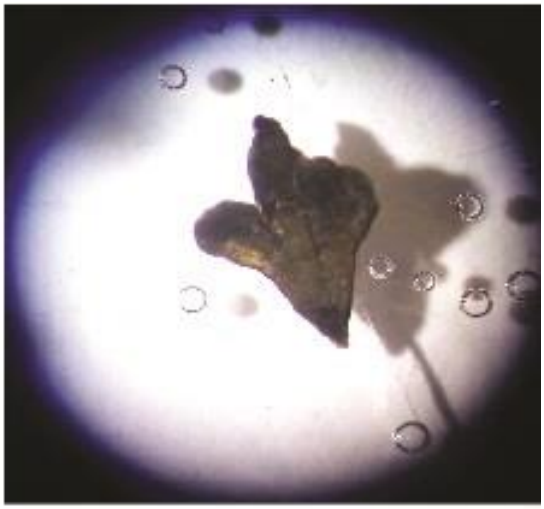

b. *Betula pubescens* female catkin scale

c. *Pinus sylvestris* bud scale

d. Leaf fragment

e. Twig

f. Conifer needles

Figure 3.7: Photographs of some of the terrestrial macrofossils included for dating (Photo: Mohib Billah)

3.3.4. Loss on Ignition (LoI)

Loss on Ignition (LoI) is a method applied to measure the amount of organic content and carbonate mineral in a sample (Heiri et al., 2001). LoI was done at EARTHLAB, the sediment laboratory of the Department of Earth Science, University of Bergen. 1 cm^3 samples were collected with a syringe from each centimeter from the PÅLP-119 sediment core. For PÅLP-219, no samples were collected below 250 cm of the sediment core as the grain size becomes large and irregular after that, and it is possible that they were deposited by the Storegga tsunami (see Discussion). The crucibles were weighed both empty and after placing the sample in them. Then, the samples were kept in an oven at 105ºC temperature overnight to get rid of water content (figure 3.8). After cooling and weighing them again, the samples were put in the oven and burned at 550ºC temperature. The burnt samples were kept in an airtight glass container with a desiccant for one and a half hours to let them cool without the samples absorbing moisture from the air. Finally, they were weighed again. Every result from weighing was recorded in a spreadsheet and the LoI was calculated using the following equation:

$$LoI_{550} = ((DW_{105} - DW_{550})/DW_{105})*100$$

where LoI_{550} is the percentage weight loss on ignition at 550ºC temperature, and DW_{105} and DW_{550} represent the dry weight of the sample before and after combustion, namely (Heiri et al., 2001). Generally, lower LoI values are expected under marine conditions in an isolation basin compared to under lacustrine conditions (Shennan et al., 2015; Romundset et al., 2018).

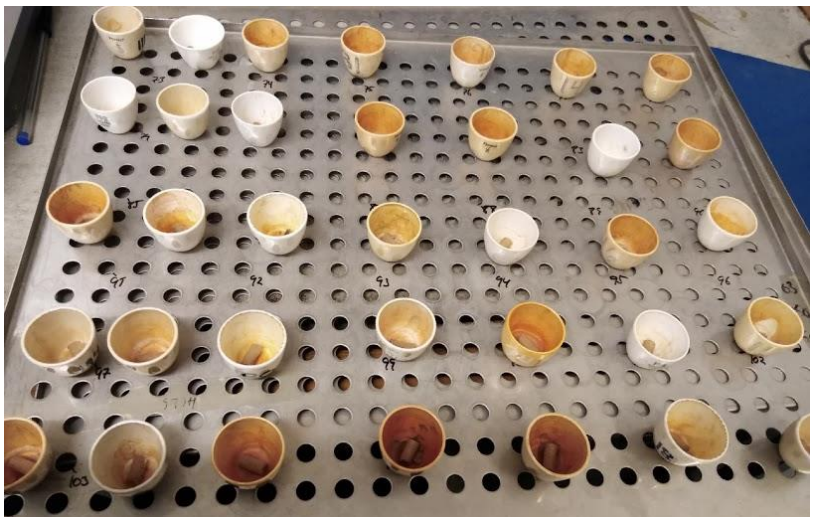

Figure 3.8: Crucibles filled with samples after keeping them in an oven at 105ºC temperature overnight while doing the LoI experiment. Photo: Mohib Billah

3.3.5. Phytoplankton Analysis

The isolation contact can be reconstructed from the change in a depositional environment using phytoplankton (Tjemsland, 1983; Kaland, 1984; Vasskog, 2006; Lid, 2019; Vasskog et al., 2019). Phytoplanktons are photosynthetic algae living in suspension in open water, as they need light to perform photosynthesis, and they dwell in the photic zone (Reynolds, 2006). Dinoflagellate cysts are generally considered indicators of marine environment, while the presence of green algae (mainly of the group *Chlorococcales*) with lower salinity tolerance (Table 3.2) indicates a gradual change from marine to the freshwater environment. Diatom analysis (Kjemperud, 1981; Lohne et al., 2007) is one of the most recognized methods to detect changes in salinity, but due to the high level of species richness, this method requires much more time than the type of phytoplankton analysis applied here (Kaland, 1984; Vasskog et al., 2019).

Table 3.2: Salinity groups used to divide phytoplanktons according to salinity tolerance. Salinity groups are suggested after Vos and de Wolf (1993) and Vasskog et al. (2019).

Salinity Group	Environment	Salinity Tolerance
Polyhalobous	Marine only	> 30‰
Mesohalobous	Brackish Water	0.2‰ – 30‰
Oligohalobous halophilous	Brackish water/freshwater (mostly brackish)	may vary
Oligohalobous indifferent	Brackish water/freshwater (mostly fresh)	may vary
Halophobous	Freshwater only	0 – 0.2‰

3.3.5.1 Preparation of Samples

Phytoplankton samples were prepared in the cosmo laboratory (Earthlab Cosmosgenic Nuclide Preparation Facility) of the Department of Earth Science, University of Bergen. A total of eight samples (1 cm^3 each) were picked across the expected isolation boundary of the core based on visual interpretation, from the results of LoI, and the non-destructive methods (XRF and MS). Phytoplankton sample preparation was done following the same procedure used for pollen sample preparation described by Fægri et al. (1989).

The main objective of the phytoplankton sample preparation is to remove the unwanted material (e.g., minerogenic material, humic acid, cellulose) and embedding in a suitable medium to present the microfossil as visible as possible (Fægri et al., 1989). The phytoplankton (algae) and pollen are kept protected throughout these removal processes as they have Sporopollenin layers in their cell walls (Jankovská and Komárek, 2000). In order to calculate the concentration of phytoplankton in each sample, three *Lycopodium* spore tablets (Batch No. 177745) were added (Stockmarr, 1972). Each *Lycopodium* spore tablet contains 18584 ± 370 spores. As the *Lycopodium* spore tablets were added before doing other procedures, they got the same treatment as the sample material. Thus the influx (deposition over time) of the phytoplankton can be calculated by counting the number of phytoplankton and *Lycopodium* remaining at the end of all treatments combined with the age model of the sediment core. During the process, 10% hydrochloric acid (HCL) was added to remove Calcium Carbonate ($CaCO_3$) and dissolve the *Lycopodium* tablets, and 10% potassium hydroxide (KOH) was added to remove humic acid (requires boiling to dissolve the samples) from the sample. Hydrofluoric acid (HF) treatment was done to remove siliceous matter by adding the acid and boiling it at 100ºC for two hours and keeping it in the fume hood overnight. Afterward, heating with 10% HCL (without boiling) was done to remove colloidal SiO_2. The mixture of acetic acid (A_2O) and concentrated sulphuric acid (H_2SO_4) in a ratio of 9:1 was added to remove cellulose in a process called acetolysis. KOH treatment was done once again at the end of the procedure. In between the treatments, samples were washed with distilled water and centrifuged in a centrifuge. Color (fuchsin) was added during the last wash so that the phytoplankton becomes more visible under a microscope. Then, samples were transferred to small 2 ml storage glasses, and glycerol was added as a mounting medium. Finally, the samples in the storage glasses were placed on a hot plate to remove water by drying.

3.3.5.2 Microscopic Examination of Slides

The microscopic analysis was conducted in the Pollen Laboratory of Department of Biology, University of Bergen. A ZEISS light microscope (63x/1.4 lens) was used for the analysis.

The slides were prepared by putting a small drop of a well-mixed sample on each slide. It was ensured to distribute the sample evenly over the slide. Finally, a glass cover was fixed on top of it, and nail varnish was used around it to protect it from any further displacement over the slide. Information on the samples was labeled on the edge of the slides.

Using the 63x/1.4 lens of the microscope requires putting a drop of immersion oil on top of the slide. Usually, the counting was started from one corner of the slide and counted across sideways. After reaching the other end of the slide, the slide was moved 1 mm vertically. For each phytoplankton specimen observed in the sample, a taxonomic key was used to identify it to the lowest possible taxonomic level. The taxonomic key of Jankovská and Komárek (2000) was mostly used for the identification. The samples were analyzed until at least 100 phytoplankton specimens were counted for each depth. For the top two slides, the density of the phytoplankton was so sparse that it required more slides to examine for each depth than the samples picked up from the lower part of the core.

The basic principle of the phytoplankton analysis is calculating the number of phytoplankton found in each level following the salinity group (Table 3.3). As the isolation contact of the sediment core is strongly related to the salinity changes of the lake, the accumulation of phytoplankton also changes with it. High salinity tolerant phytoplankton is usually found in the marine part of the sediment core, whereas the least salinity tolerant phytoplankton deposited in the lacustrine part of the core. Different species/genera of phytoplankton found in this study are described here.

Dinoflagellate cysts (figure 3.9) are mainly marine-dwelling and therefore considered as polyhalobous here. The shape of the cysts may vary between round and oval shapes. But, the most dominating feature to identify this is the T-shaped horns. With the reduction of salinity, the abundance of *Dinoflagellate* cysts reduces significantly.

Pediastrum praecox (figure 3.9) is one of the morphological variants of *Pediastrum*, but it is uncertain whether it should be categorized as a separate species as it could be a malformation of *Pediastrum boryanum*. In this work, it is classified as oligohalobous halophilous, as it is usually found in brackish conditions (Vasskog, 2006).

Scenedesmus spp. (figure 3.9) has a maximum salinity tolerance level up to 8‰, but can be found them in large quantities in weak salinity levels up to 4.2‰ to 6.4‰, and with high nutrient and high pH values, the conditions prevailing during the isolation phase (Tjemsland, 1983). Thus, the genus is kept under the oligohalobous halophilous salinity group. It is only identified to the genus level as the morphological criteria to distinguish them are often broken while preparing the sample, and it is difficult to see them in a regular microscope (Vasskog, 2006).

They are usually seen as four elongate cells sticking together, but the number of cells may vary (Vasskog, 2006). Many species have two long horns on the border cell (Vasskog, 2006), which were not seen with the light microscope in the current study.

Table 3.3: Different phytoplankton taxa observed in the PÅLP-119 sediment core. Salinity groups are suggested after *Vos and de Wolf (1993)* and *Vasskog et al. (2019).*

Phytoplankton taxa	**Salinity Group**
Dinoflagellate	Polyhalobous
Pediastrum praecox	Oligohalobous halophilous
Scenedesmus spp.	Oligohalobous halophilous
Tetraedron minimum	Oligohalobous halophilous
Botryococcus braunii	Oligohalobous indifferent
Pediastrum integrum	Oligohalobous indifferent
Pediastrum boryanum	Oligohalobous indifferent
P. boryanum var longicorne	Oligohalobous indifferent
Pediastrum orientale	Oligohalobous indifferent
Pediastrum tetras	Oligohalobous indifferent
Pediastrum braunii	Halophobous

Tetraedron minimum (figure 3.9) is a single-celled alga. Tjemsland (1983) found that the abundance of this species can increase dramatically just after an isolation, and it is categorized as Oligohalobous halophilous as it can tolerate salinity up to 3‰ (Lid, 2019).

Botryococcus braunii (figure 3.9) is easy to distinguish as it looks reddish as a result of absorbing color added during the preparation of the sample. The cells of *Botryococcus braunii* remain in a cluster, which makes it difficult to separate one cell from another (Tjemsland, 1983). The species may tolerate a salinity range of 0 – 7.8‰ (Tjemsland, 1983); therefore, it is categorized under the oligohalobous indifferent salinity group.

Pediastrum boryanum is the most common *Pediastrum* species with many variants. Among the variants, *Pediastrum boryanum var longicorne* (figure 3.9) were most common in the current study. The colony of species has a round shape, typically with two horns in each border cell, and small warts on the surface. The most significant difference between *Pediastrum boryanum*

and *Pediastrum boryanum var. longicorne* is that *Pediastrum boryanum var. longicorne* has longer-horns than the regular one. *Pediatrum boryanum* is found in a wide range of environmental conditions, which make it a weak indicator of environmental change (Vasskog, 2006). This species is classified as eutrophic and alkaline since it is found at an optimum level, given relatively high nutrients and pH (Jankovská and Komárek, 2000). *Pediastrum boryanum* is found mostly below 2.7‰ – 3‰, with a maximum salinity tolerance of about 8‰ (Tjemsland, 1983; Kaland, 1984). Therefore, it is categorized under oligohalobous indifferent salinity group.

Pediastrum integrum (figure 3.9) has a colony of circular shaped cells with no gaps in between. The horns are tiny, and the surface is smoother than the *Pediastrum boryanum* (figure 3.9). Both the species are usually found in the same level, but *Pediastrum integrum* is more salinity tolerant, and usually less in number than *Pediastrum boryanum* (Lid, 2019).

Pediastrum orientale (figure 3.9) has a flat coenobia (cell colony) with no hole in between the cells, externally rounded marginal cells, short cylindrical processes (horns), and distinctly regular granulated cell walls (Jankovská and Komárek, 1995; Turner et al., 2014). The distribution of *Pediastrum orientale* is confined to clear and cold water biotopes (Jankovská and Komárek, 1995). The abundance of the species has been observed to increase during the warming climate of the early Holocene together with the increase of other *Pediastrum*, e.g., *Pediastrum boryanum var longicorne* (Sarmaja-Korjonen et al., 2006; Jankovská and Komárek, 2000; Turner et al., 2014). Thus, it is categorized under the oligohalobous indifferent salinity group.

Pediastrum tetras (figure 3.9) has several cells, in a colony, which are connected without having a gap in between. The cell border has an incision with two pointed horns. The species is so small that it may be overlooked under the light microscope. It is slightly less salinity tolerant than *Pediastrum boryanum* (Tjemsland, 1983).

Pediastrum braunii (figure 3.9) has a circular outline with a 25 - 40 µm dimension where cells are close together with no holes between the cells, the outer margin is almost straight without any incision, and the cell wall is evenly granular. (Komárek and Jankovská, 2001). Ecologically, this species is found in cold and clear swampy localities. Tjemsland (1983) and Vasskog (2006) found this species as a good indicator of freshwater condition. Thus, this species is categorized under halophobous salinity group.

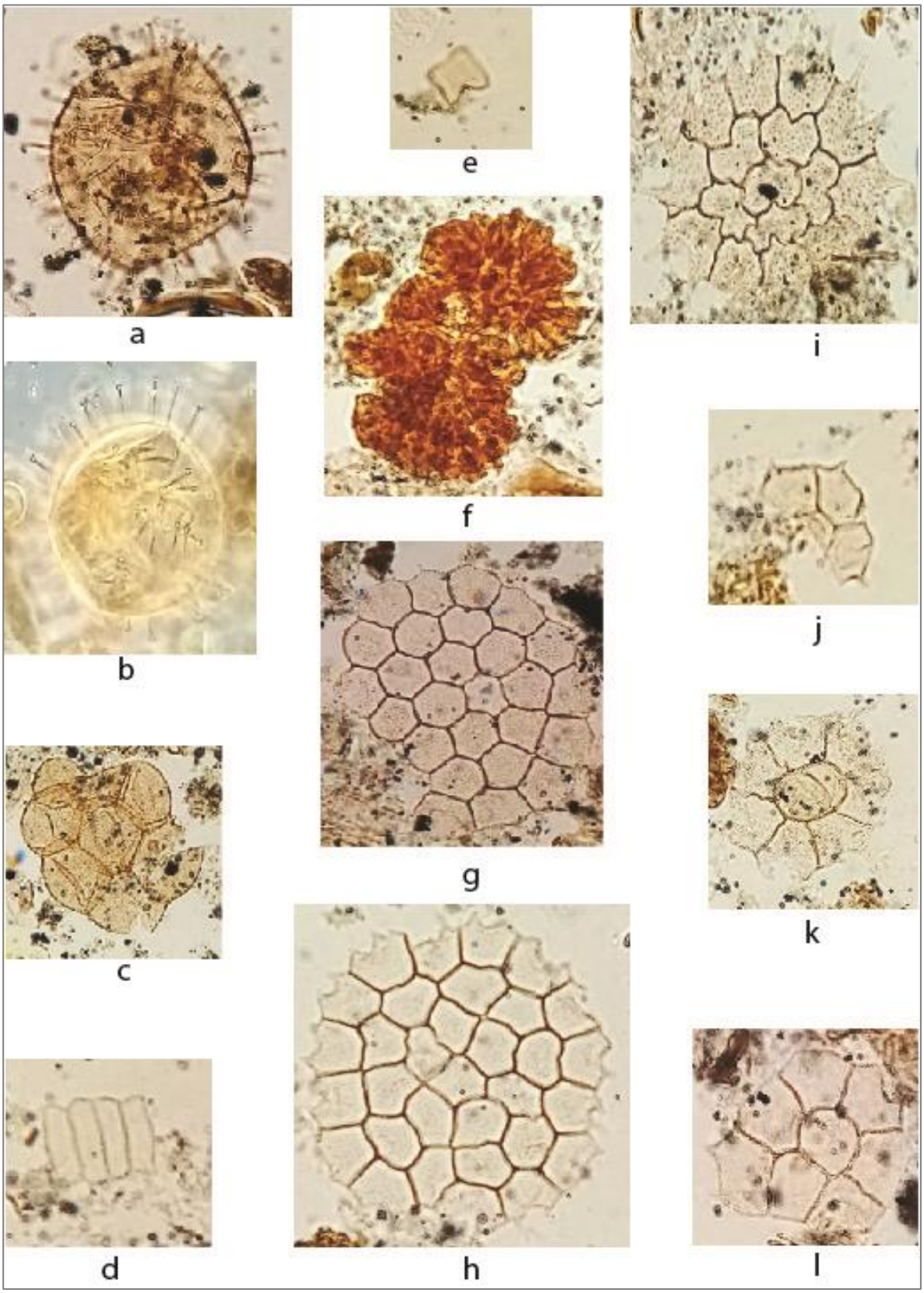

Figure 3.9: Photographs of phytoplankton found in the present study: a-b: *Dinoflagellate* cyst, c: *P. praecox*, d: *Scenedesmus spp*., e: *T. minimum*, f, *B. braunii*, g: *P. intergrum*, h: *P. boryanum*, i: *P. boryanum var longicorne*, j: *P. orientale*, k: *P. tetras*, l: *P. braunii*. (Photo: Mohib Billah)

3.3.5.3 Phytoplankton Diagram

After completing the counting, the data was analyzed in Rstudio and the Tilia software. Before adding the data in Rstudio, the phytoplankton numbers are converted into percentages for the each particular depth. In Rstudio, the "rioja" package, designed for the analysis of Quaternary science data (Juggins, 2017), was used to plot the diagram of the percentage of phytoplankton assemblage according to the depth. The default 'strat.plot' function was used except defining the y-axis and different colors for different phytoplankton groups. Cluster analysis was done by applying 'chclust' function of 'vegan' package of Rstudio (Oksanen et al., 2019). In addition, Tilia software, designed for plotting paleontological and stratigraphic data, was used to plot the influx rate.

4. Results

4.1. Quaternary Geological Mapping

4.1.1. Glaciofluvial Delta

UTM coordinates: UTM33 7603704N 572518E (one of the points of measurements)
Height: 74.37 m
Area: 0.066 km^2

During the fieldwork, an around 88 m long exposed section (figure 4.1) was found in a human-made gravel pit within the study area (figure 4.2). From the exposed section, two main sedimentary units were recognized: a 1-2 m thick top layer that was almost horizontal, and underlying layers that were tilted with a relatively steep gradient (figure 4.3). The grain sizes of the exposed section were well sorted. The dominant grain sizes were sand and gravel. However, larger gravels and cobbles were embedded into the matrix-supported top unit, whereas, the grain sizes vary between sand and fine gravel in the layers (from a few cm to some tens of cm thickness) of the underlying bottom unit. In addition, the entire landform has a flat top with channel forms that can be seen in the LiDAR image (chapter 3, figure 3.6).

Figure 4.1: The exposed portion of the Gilbert type glaciofluvial delta. Photo: Mohib Billah

The characteristics of the deposits were found similar to a Gilbert type delta (Dabrio et al., 1991). Based on the channel forms on the surface of the top, the upper unit is interpreted as the topsets that are usually formed by glaciofluvial meltwater rivers on top of the delta. On the basis

of the gradient and grain sizes, the lower unit is interpreted as the foreset of the delta. The boundary between the topset and foreset of such delta can provide the altitude of the former sea level (Dabrio et al., 1991). Such deltas usually form in tectonically active areas of high relief, glacier-marginal setting, and fjord settings (Corner et al., 1990), the one found in the study area is assumed to have formed in a glacier-marginal setting during the last deglaciation.

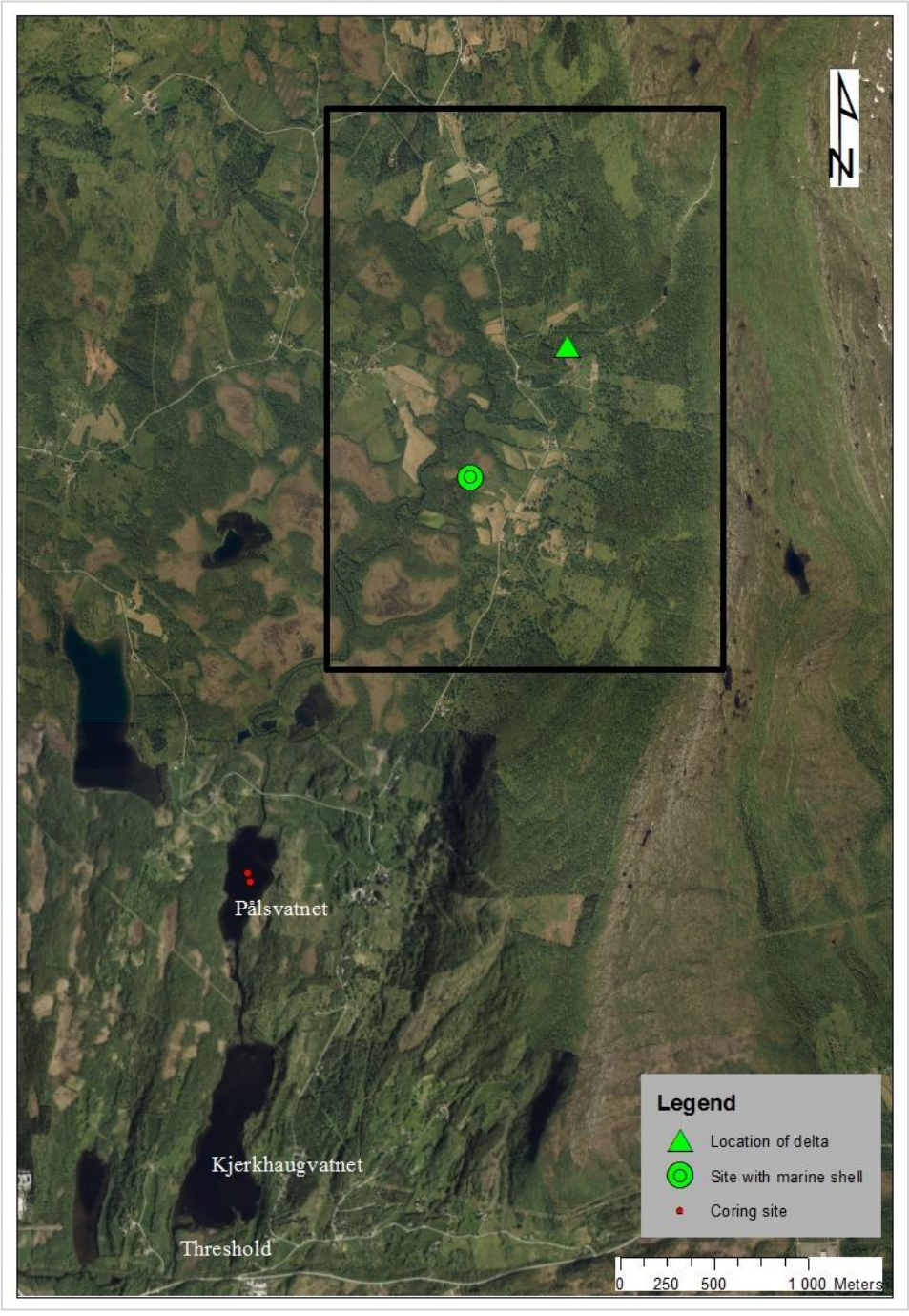

Figure 4.2: The location of the gasciofluvial delta, the site with marine shells, and Pålsvatnet along with its threshold. The Quaternary geological mapping area is marked with the rectangle. The background aerial photo is from Geonorge (2020).

Figure 4.3: Large grain sizes were embedded into the topset (left), Tilted layers of fine grained sediments of the foreset underlying the topset (right). Photo: Mohib Billah

4.1.1.1 The Altitude of the Delta

The altitude of the delta surface (figure 4.4) was measured by LiDAR, before the height of the transition between topset and foreset was found by deducting the thickness of the topset (table 4.1). The average height of this transition was 74.49 m. The altitude of the intertidal flat of the delta does not reflect the high-water level (Hori et al., 2001) like an isolation basin threshold do, since sediments stored temporarily on the delta during high tide can be removed during low tide (Eilertsen et al., 2011). The mean low water spring tide (MLWST) is considered a more likely tidal level corresponding to the sedimentary transition between topset and foreset when the delta formed, and the indicative meaning of this feature is therefore interpreted to represent the MLWST. Because of this, the measured altitude was adjusted by subtracting the local present-day MLWST for the study area, which is a negative value of -1.34 m. Thus, the final altitude used in the sea-level curve of this study is 75.83 m for the delta. The error limit of the altitude of topset-foreset boundary of the glaciofluvial delta will be discussed in chapter 5.

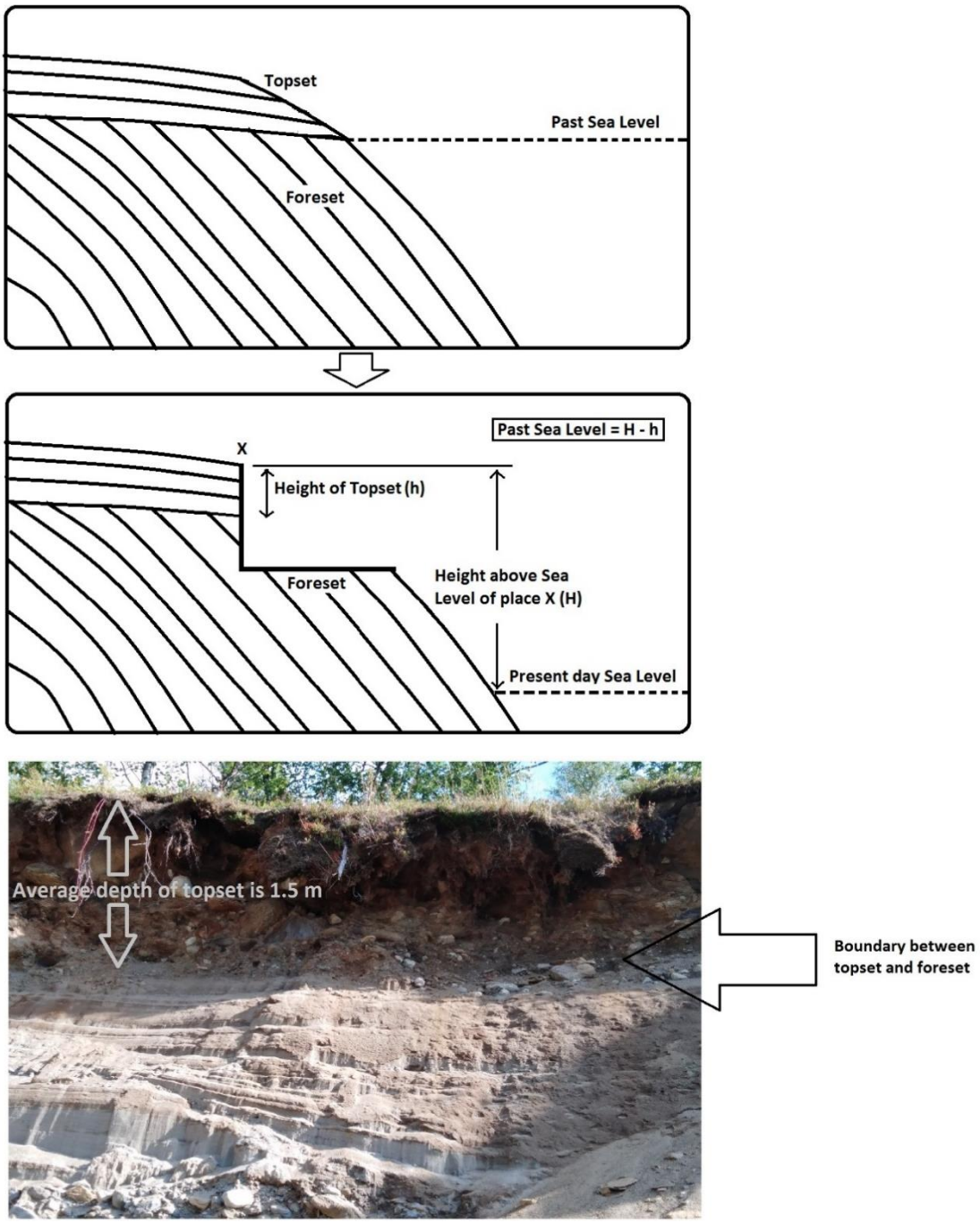

Figure 4.4: Schematic diagram of topset measurement (top), and topset measurement of the glaciofluvial delta (bottom). Photo: Mohib Billah

Table 4.1: Altitude measurement of glaciofluvial delta: altitude of the delta (column 4) is calculated by subtracting the height of topset from the altitude found in the LiDAR, and the mean low water spring tide (column 6) has been subtracted from the average altitude (column 5) of the topset-foreset boundary of the glaciofluvial delta.

Coordinate of measurement point	Altitude in LiDAR (m)	Height of topset (m)	Altitude of delta (m)	Average (m)	MLWST (m)	Altitude after adjusting tidal limit (m)
1	2	3	4	5	6	7
UTM33 7603704N 572518E	75.05	1.5	73.55	74.49	-1.34	75.83
UTM33 7603705N 572537E	77.1	1.5	75.6			
UTM33 7603696N 572542E	76.56	1.8	74.76			
UTM33 7603684N 572543E	75.19	1.1	74.09			

4.1.2. Site with Marine Shells

UTM coordinates: UTM33 7602985N 572115E (an excavated ditch in the study area)
Height: 40.27 m
Area: 0.81 km^2

Large amounts of marine shells (figure 4.5) were observed in a ditch excavated in a field between Myrnes and Storelva (location marked with a star in figure 4.2). The marine shells were distributed all the way along the excavated ditch. The grain size of the field was dominated by silt and sand.

Figure 4.5: Marine shells found in an excavated ditch. Photo: Mohib Billah

Based on the large amount of marine shells and the fine-grained sediments, this area is interpreted as a marine deposit formed at a water depth well below the intertidal zone. The elevation of the site is below the marine limit, and the surrounding area is therefore marked as marine in the Quaternary geological map.

The Quaternary geological map (figure 4.6) surrounding area of the delta was prepared through field observation and cross-matching with other published materials, as mentioned in chapter 3. The area mapped as weathered material in the map of the Geological Survey of Norway is here re-interpreted as till based on the assumption that the area was covered by an erosive ice sheet prior to the last deglaciation. However, it is possible that some amount of weathered material has been produced in the relatively short period following deglaciation, as carbonate-rich bedrock in the area can be easily weathered. The outer limit of the presumed till deposits were determined based on the presence of dense vegetation coverage in the aerial photographs.

Due to budget and time constraints, it was not possible to investigate every unit presented in the map in the field. NGU symbology was used to develop the map.

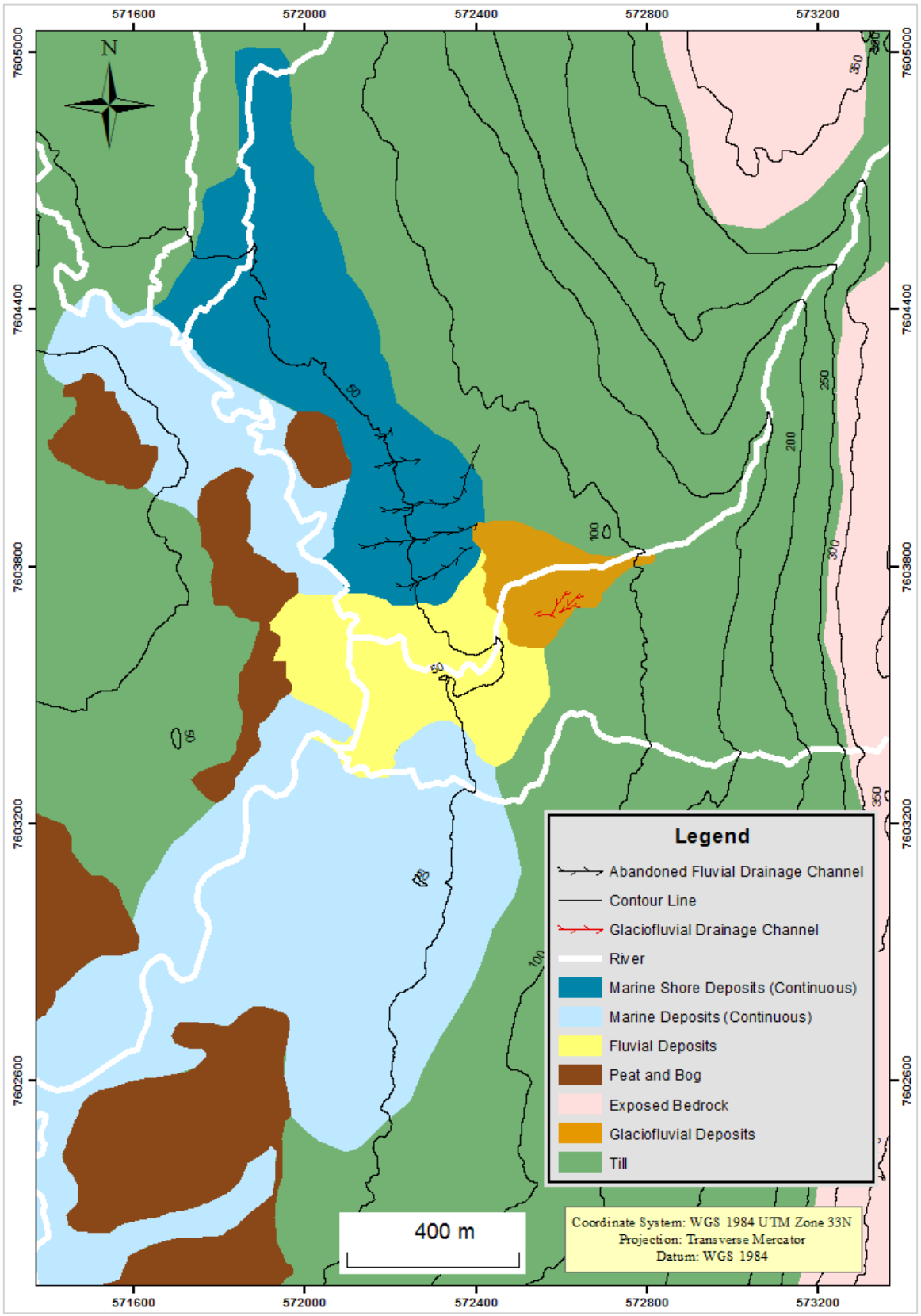

Figure 4.6: The Quaternary geological map of the delta and its surrounding area.

4.2. Pålsvatnet

UTM coordinates: UTM33 7600928N 570823E (Coring site of PÅLP-119)
Threshold height: 23.62 m
Area: 0.114 km^2

Pålsvatnet has an area of 0.13 km^2 with a maximum depth of 13.2 m (figure 4.7), and the water surface is 24.3 m above sea level. The lake is located in the Evens Municipality of Nordland county of northern Norway, approximately 2.65 km northeast from the Harstad-Narvik airport. The water drains out from Pålsvatnet towards the south into the next downstream lake, Kjerkhaugvatnet. An aerial view (figure 4.2) of the lake and its surrounding area shows that a substantial amount of the surrounding land is covered by marshland and forest. The bedrock of the area is dominated by lime, and the bedrock containing lime may often cause a hard water effect in lakes. The threshold of the lake, which is shared with Kjerkhaugvatnet, is formed in bedrock, and as mentioned in chapter 3, it is a great advantage of having a bedrock threshold when using the isolation basin method. LiDAR data of Høydedata (2019) was used to determine the threshold of the lake.

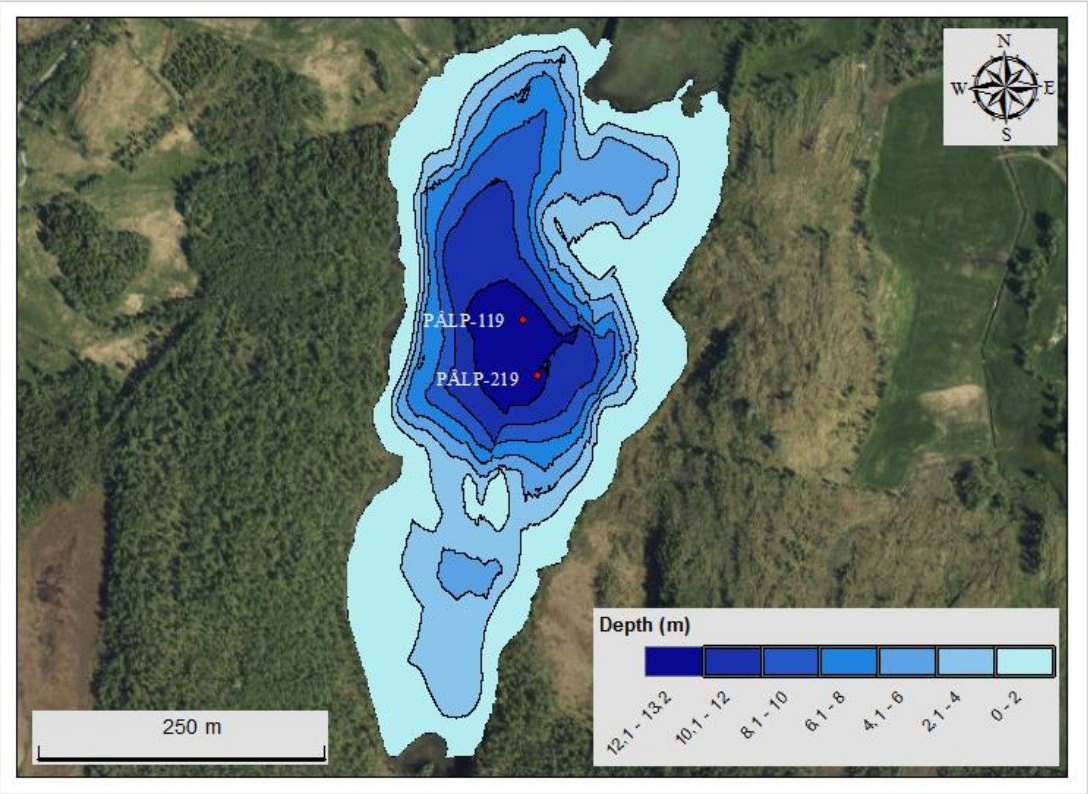

Figure 4.7: Bathymetric map of Pålsvatnet. The coring sites are marked with red dots. The background aerial photo is from Geonorge (2020).

As mentioned in the previous chapter, the bathymetric data was collected with a Garmin GPSMAP 721xs echo sounder system. Using the data, the bathymetric map (figure 4.7) was generated with the help of ArcMap software. From the bathymetric map, it is seen that the lake becomes deeper from its margin to the center, and the deepest part of the lake is around 13.2 m from where the two sediment cores were collected for this study.

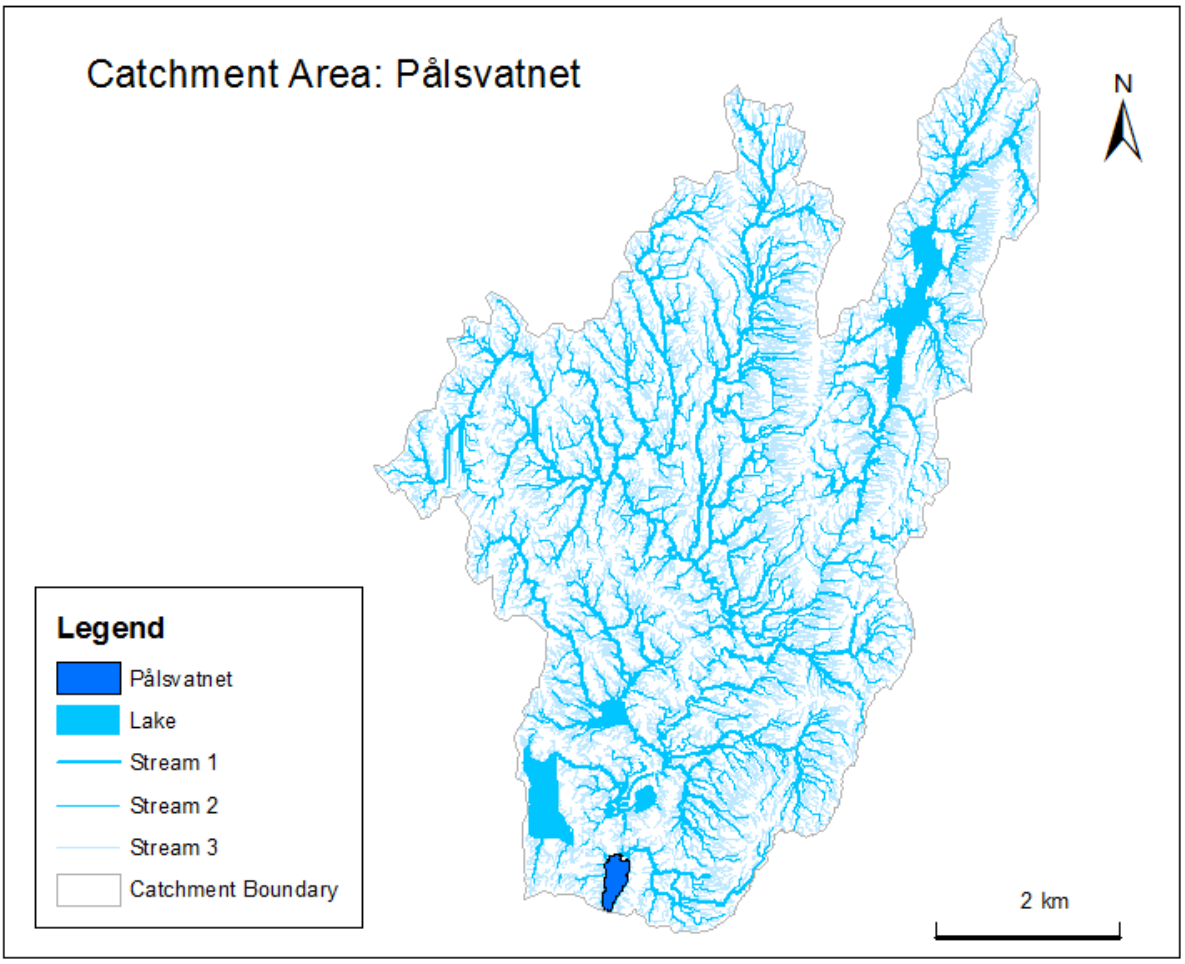

Figure 4.8: The catchment area of Pålsvatnet. The lake is marked with dark blue in the map.

A lake catchment includes the surrounding area from where water from precipitation will reach in the lake. The catchment area of Pålsvatnet is about 35.5 km^2 (figure 4.8). The catchment boundary is cross matched with the published catchment boundary of (NVE, 2020).

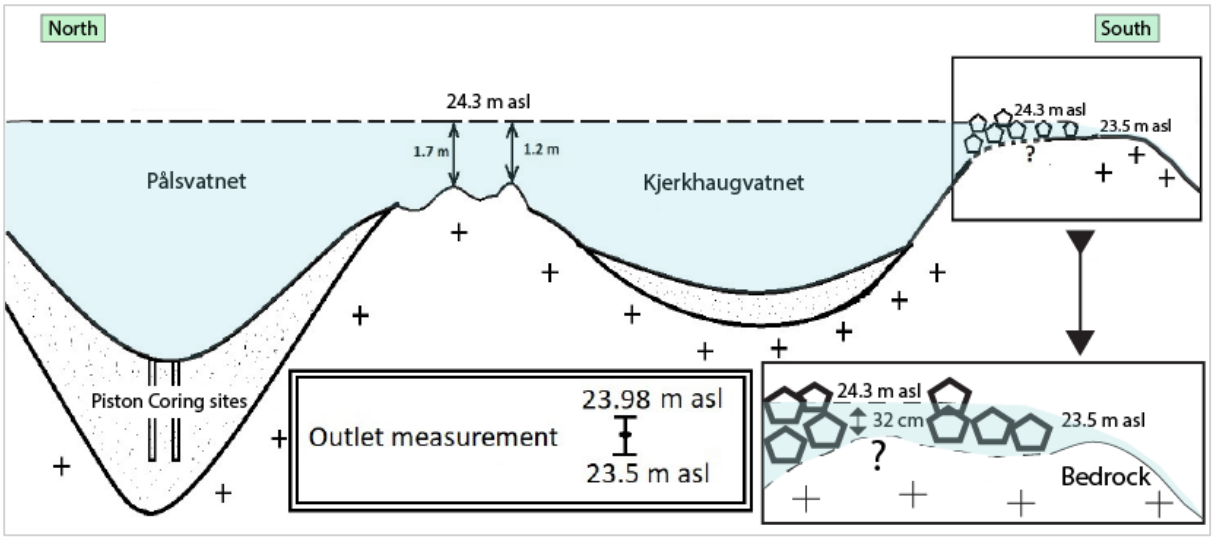

Figure 4.9: Schematic diagram of the measurement of the lake threshold.

4.2.1. Lake Threshold

The altitude of the threshold was measured to 23.74 m (table 4.2), based on the two possible lowest points of the threshold. This includes an area close to Kjerkhaugvatnet that was covered by boulders, where the lowest point between the boulders was measured to 32 cm below the water level, and a downstream point where the water flows across a bedrock threshold, at 23.5 m (figure 4.9). From the average of the two points of measurement, the altitude was adjusted according to the local mean high water spring tide (MHWST). The altitude of the threshold after adjusting MHWST is 22.4 m. The error limit of the basin threshold will be treated in the discussion chapter.

Table 4.2: Altitude measurement of the threshold of Pålsvatnet: altitude of the threshold (column 4) was calculated by subtracting the depth between boulders (in case the bedrock was not seen) (column 3) from the altitude found in the LiDAR (column 2), and altitude of the high water spring tide (column 6) has been subtracted from the average altitude (column 5) of the basin threshold.

Coordinate of measurement point	Altitude in LiDAR (m)	Depth between boulders (m)	Altitude of threshold (m)	Average (m)	MHWST (m)	Altitude after adjusting tidal limit (m)
1	2	3	4	5	6	7
UTM33 7698915N 570451E	24.3	0.32	23.98			
UTM33 7598807N 570434E	23.5	-	23.5	23.74	1.34	22.4

4.2.2. Lithostratigraphy

From the analysis of PÅLP-119 and PÅLP-219, five stratigraphic units were identified from the lake. The units were marked with 'P' (for Pålsvatnet) and an integer from 1 to 5 (from the lowermost to the uppermost). The units are described here:

P1

P1 is the lowermost unit extracted from the lake. This unit extends from the bottom of the core (310 cm) to around 248 cm depth in PÅLP-219 (figure 4.10). However, PÅLP-119 did not penetrate deep enough to capture this unit. The color of this unit is grey to light grey. Sand and gravel are the two prominent grain sizes of the unit. However, three large cobbles are also found in the unit. Marine shells are also common throughout the unit. No significant lamination is observed. LoI examination for this part of the core was not done because of the large grain sizes. However, the unit obviously has a very low organic content. The magnetic susceptibility of the unit is very irregular, with a lot of spikes.

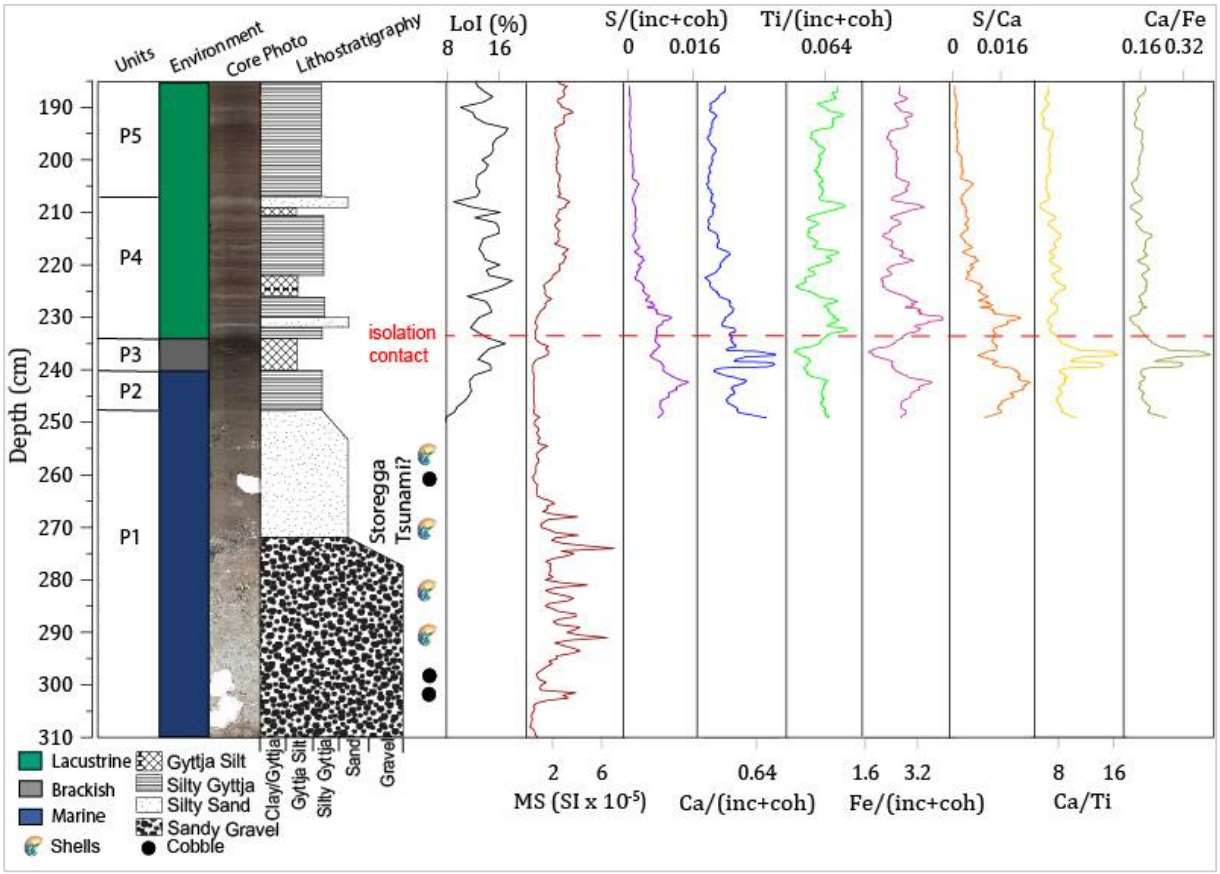

Figure 4.10: Overview of the lithostratigraphy of PÅLP-219 along with the results of LoI, MS, and XRF.

Because of the presence of more minerogenic particles and marine shells, the layer could be considered as a purely marine layer. The existence of the large and irregular grain sizes is hard to explain from regular marine processes, however, and one possibility is that the unit could represent the Storegga tsunami (see Discussion).

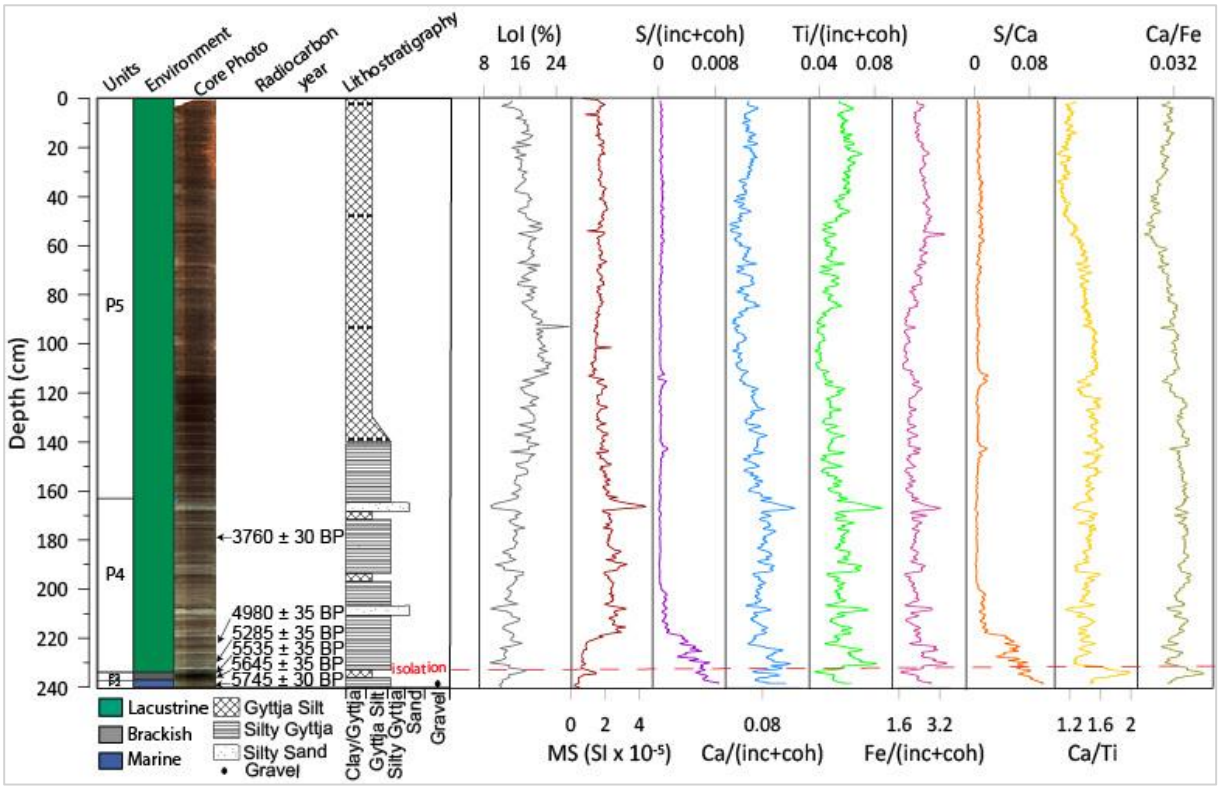

Figure 4.11: Overview of the lithostratigraphy of PÅLP-119 core along with the results of LoI, MS, and XRF.

P2

This unit is found in both the cores, from around 248 cm to 240 cm in PÅLP -219 (figure 4.10), and from the bottom to around 236 cm in PÅLP-119 (figure 4.11 and figure 4.12). The color of the section is dark grey with some visible layers. The texture of the unit is mainly silty gyttja. In addition, the organic content of the unit is also comparatively low (~12%) with low magnetic susceptibility.

Based on the texture and the organic content of the unit, in addition to the occurrence of marine shells in unit P1 from the adjacent core, unit P2 is interpreted as marine sediments. The combination of low LoI values and low MS is unusual, as a higher minerogenic content usually gives higher MS. One possible explanation could be that the bedrock of the area is dominated by carbonate rock (calcium carbonate), which is diamagnetic. In addition, due to marine

conditions, more carbonate could have been deposited from marine shells and other marine materials. As a result, this could explain low magnetic susceptibility found in this unit.

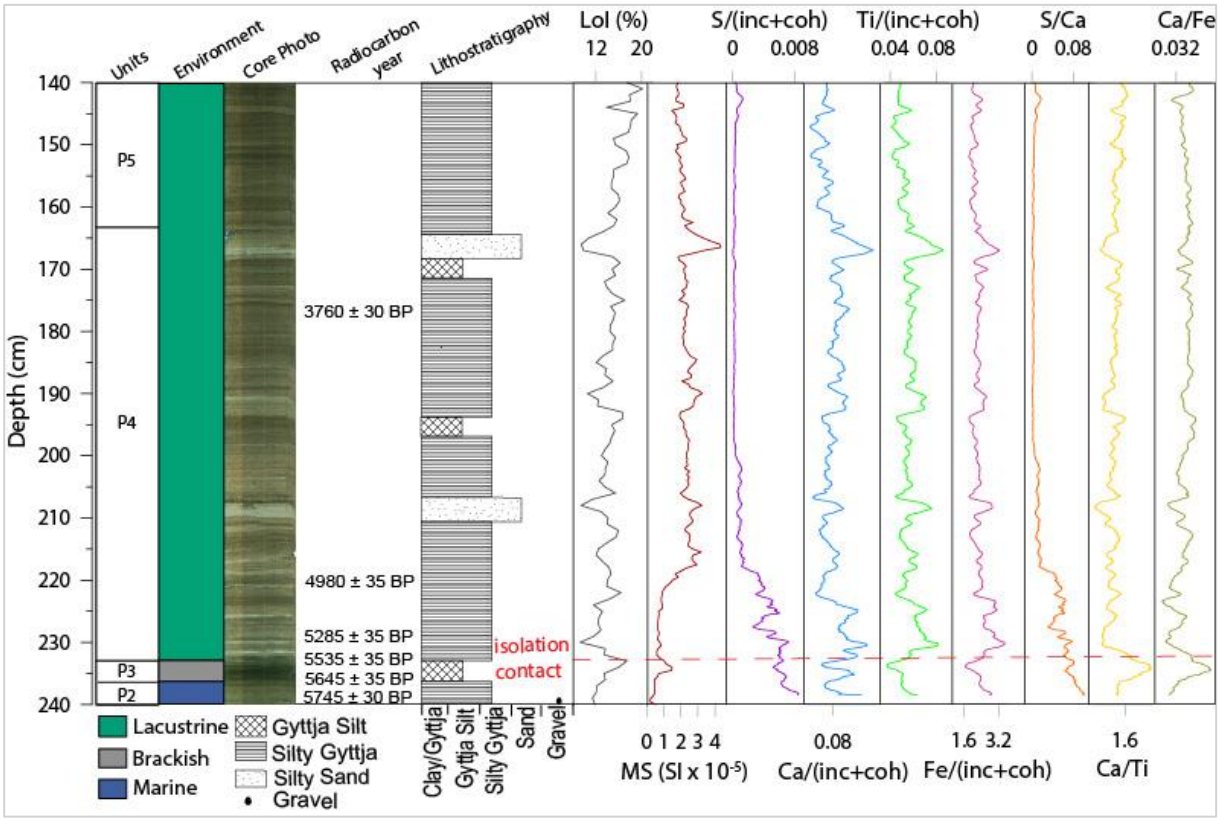

Figure 4.12: Overview of the lithostratigraphy of the lower part of PÅLP-119 core along with the results from LoI, MS, XRF.

P3

Unit P3 extends from 236 cm to 233 cm in PÅLP-119 (figure 4.11 and figure 4.12) and 234 cm to 247 cm in PÅLP-219 (figure 4.10). The color of the unit is dark, almost black, and it is the darkest part of the core. The texture of the unit is mainly gyttja silt with dark-colored laminations. Organic contents are higher in this unit than unit P2. Magnetic susceptibility of this unit is also slightly higher than the previous unit.

Unit P3 is interpreted as a brackish phase associated with isolation of the lake on the basis of dark-colored laminations. Such laminations are very common for the sediments deposited during an isolation phase. When freshwater remains on top of saline water, the water column tends to be stratified during this period. As a result, an anoxic bottom conditions prevents disturbance of lamina from bioturbation, and precipitation of sulphur can occur (Kjemperud,

1986; Balascio et al., 2011; Romundset et al., 2018; Vasskog et al., 2019). The increase in magnetic susceptibility could also be explained in relation to the isolation phase, as the oxic-anoxic transition in the water column is a preferred habitat of magnetotactic bacteria (Bazylinski et al., 1991), which could probably contribute to the increase of MS value.

P4

The depth of unit P4 is marked from 233 cm to 163 cm in PÅLP-119 (figure 4.11 and figure 4.12) and 234 cm to 207cm in PÅLP-219 (figure 4.10). The unit has some clear layers, where the color varies from grey to dark grey. The dominant texture is silty gyttja. However, in between, there are some layers of silty sand. In general, the organic content in the unit is lower than unit P3, and the magnetic susceptibility of this unit is comparatively higher than the previous units.

As it is observed a sharp change in the sediment core just above P3 to a more brownish color, unit P4 is interpreted to have developed during a lacustrine phase after the lake became isolated. Both the results from LoI and MS indicate a high amount of minerogenic content that could be interpreted as in-washed minerogenic material from the surrounding area when vegetation coverage was not that prominent. Low organic and high magnetic grey layers could be explained by natural events like floods or longer periods of increased runoff.

P5

Unit P5, the top most unit of the cores, extends from 163 cm to the top of the PÅLP-119 (figure 4.11 and figure 4.12) and from 207 cm to the top of PÅLP-219 (figure 4.10). The color of this unit is dark grey to brown, and the texture is mainly silty gyttja. The unit is layered, although with less prominent layers than unit P4. In terms of organic content, this unit is the most organic rich unit of the cores. The magnetic susceptibility of the unit is slightly lower than its previous unit.

Based on the color, texture, organic content, and magnetic susceptibility value, the unit is interpreted as the lacustrine phase of the core with no marine influence on the lake. This unit represents a continuation of the lacustrine sediments, but with gradually lower input of silt in the lake. One explanation of higher organic content could be correlated with the development of vegetation around the lake. This could also be happened due to a warming climate or less input of sediment from erosion.

On the basis of lithostratigraphic analysis, the sedimentological isolation contact is interpreted to correspond to the upper limit of unit P3.

4.2.3. XRF Analysis

The geochemical counts from ITRAX-XRF analysis has been used for studying isolation basins in previous studies (Balascio et al., 2011; Strunk et al., 2018; Vasskog et al., 2019). From the high-resolution (500 µm) data, the results of some geochemical elements and their ratios are shown with the corresponding graph in figure 4.10, figure 4.11, and figure 4.12. Sulphur (S), Calcium (Ca), Titanium (Ti), Iron (Fe), and their ratios with Ca are studied along with the stratigraphic units to see if they could be used to identify marine conditions (Balascio et al., 2011; Croudace and Rothwell, 2015; Strunk et al., 2018). From the results of S and S/Ca, high counts are observed in unit P2 and P3, and the counts become gradually lower after unit P3. On the other hand, the counts of Ca, Ti, and Fe were found almost similar throughout the core. These three elements had slightly lower counts in unit P2 and P3, but, at unit P4, they had some peaks when the supply of silt increased. Interestingly, the ratios of Ca/Ti and Ca/Fe has a distinguishable peak in unit P3.

Change of Ca and Ca/Fe are considered to reflect the change of sedimentation environment, and usually higher counts are observed when the basin environment is marine or brackish (Strunk et al., 2018). Based on this explanation, it could be interpreted that the basin transitioned from brackish to lacustrine conditions after P3. On the basis of low Ti count, unit P3 could also be interpreted as brackish since the input of minerogenic sediments was lower, which resulted in low Ti count (Bakke et al., 2010). Higher S content and S/Ca ratio at unit P3 could be interpreted as the brackish phase of the lake, because, S could be increased due to anoxic bottom environment and stratification of the water column (Balascio et al., 2011; Vasskog et al., 2019).

4.2.4. Phytoplankton Analysis

The main purpose of the phytoplankton analysis is to confirm and refine the determination of the isolation contact in the core that is suggested from the lithostratigraphic analysis. As different phytoplankton types have different levels of salinity tolerance, species composition (table 4.3) also changes accordingly to salinity changes. Figure 4.13, and 4.14 are generated with the data (table 4.3) of phytoplankton analysis.

The percentage composition of the phytoplankton assemblage (figure 4.13) should respond to the salinity condition of the basin. In other words, the phases of isolation could be retrieved from the percentage of phytoplankton assemblage as per the salinity groups. From 239 cm to 232.5 cm depth of the core, *Dinoflagellates* are the dominant taxa in the basin. Some other species are also found, e.g. *Pediastrum praecox*, *Scenededmus spp*., *Botrycoccous braunii*, and some other *Pediastrum* (except *Pediastrum orientale* and *Pediastrum braunii*) from 239 cm to 232.5 cm deapth. From depth 232.5 cm to 231 cm, *Scenededmus spp*. is the most common phytoplankton. However, there is a sharp drop in the percentage of *Dinoflagellate*, while *Botrycoccous braunii*, and other *Pediastrum* (except *Pediastrum orientale* and *Pediastrum braunii*) are gradually increasing between 23.5 cm and 231 cm depths. From 231 cm *Scenededmus spp*. decreases, while *Botrycoccous braunii*, and other *Pediastrum* (except *Pediastrum praecox*) are moderately becoming more dominant in the lake.

Table 4.3: Summary of phytoplankton taxa counted using ZEISS light microscope.

Depth (cm)	*Dinoflagellate*	*P. praecox*	*Scenedesmus spp.*	*T. minimum*	*Botryococcus braunii*	*P. integrum*	*P. boryanum*	*P. boryanum var longicorne*	*P. orientale*	*P. tetras*	*P. braunii*	Unidentified *Pediastrum*	*Lycopodium*
224	0	2	1	1	41	14	29	4	1	2	3	26	827
228	3	4	2	1	63	7	15	3	0	0	0	7	589
230	1	3	24	1	31	7	18	7	0	1	2	10	249
232	1	6	90	5	17	8	20	6	0	0	0	13	101
233	324	8	16	14	25	32	51	20	0	2	0	35	155
234	173	11	28	1	4	58	48	13	0	0	0	49	155
236	59	5	0	1	7	18	11	3	0	0	0	31	145
239	86	0	1	0	0	6	2	0	0	0	0	16	100

The relative frequency (figure 4.11) shows that the abundance of less salinity tolerant species increases as the lake transitioned from a marine basin to a freshwater lake. Here, unidentified *Pediastums* are categorized under oligohalobous indifferent salinity group since most of the *Pediastrum* species are found in this salinity group. Below 232.5 cm of the core, the percentage of polyhalobous phytoplankton dominates. The oligohalobous halophilous salinity group, which prefer brackish/freshwater conditions, are mainly found around 232.5 cm. Although Oligohalobous indifferent (mostly fresh, but also found in brackish/freshwater) are found below 232.5 cm, they are more prominent above 232.5 cm. Most importantly, halophobous, the freshwater salinity group, are only seen above 230 cm.

Based on the phytoplankton assemblages and relative frequency diagram (figure 4.13), 232.5 cm depth is interpreted as the phytological isolation contact for the lake. Because polyhalobous taxa decreases sharply in the basin, this is a clear indication of the initial salinity changes in the basin, from marine to brackish. Furthermore, the presence of *Pediastrum braunii* confirms fully the freshwater conditions in the lake since this kind of *Pediastrum* has a very low tolerance (halophobous) to salinity (Vasskog et al., 2019). There is always a chance of finding freshwater phytoplankton in marine environments because they can be washed out into the ocean with streams. This may also happen because some species may tolerate a bit more or less salinity than the salinity range of the group they belong to, for example, *Pediastrum boryanum* can live in a weak salinity region even though they are mostly found in the freshwater region (Tjemsland, 1983).

Based on figure 4.13, it is found clear that at the level 232.5 cm, the phytological isolation started, which is the main point in the context of the paleoenvironment.

From the influx analysis diagram (figure 4.14), almost the same result is found. The influx of polyhalobous (most salinity tolerant group) is dominant up to 233 cm of the core. After this level, it has a very low influx rate. For oligohalobous halophilous, the phytoplankton group that is usually found in the brackish phase of a lake, influx is higher between 234 cm and 232 cm. However, except *Botrycoccous braunii* and *Pediastum tetras*, all other species from oligohalobous indifferent salinity group, has a higher influx at 234 cm. *Botrycoccous braunii* had a high influx rate all the way up to 224 cm. The halophobous, fully freshwater phytoplankton, has a higher influx rate from 224 cm to 230 cm.

In between 232 cm and 233 cm, the influx rate of the polyhalobous taxa drops sharply (figure 4.14). That is the most important reason to determine the phytological isolation contact at 232.5 cm. Moreover, oligohalobous halophilous species shows a high influx at around 233 cm, which is a significant indication of the brackish zone. Most importantly, the influx of halophobous started after 232 cm; and thus, this level is interpreted as deposited during the lacustrine phase of the lake. The higher influx rate at 234 cm for most of the species could be explained by the higher rate of sedimentation during that phase of the lake.

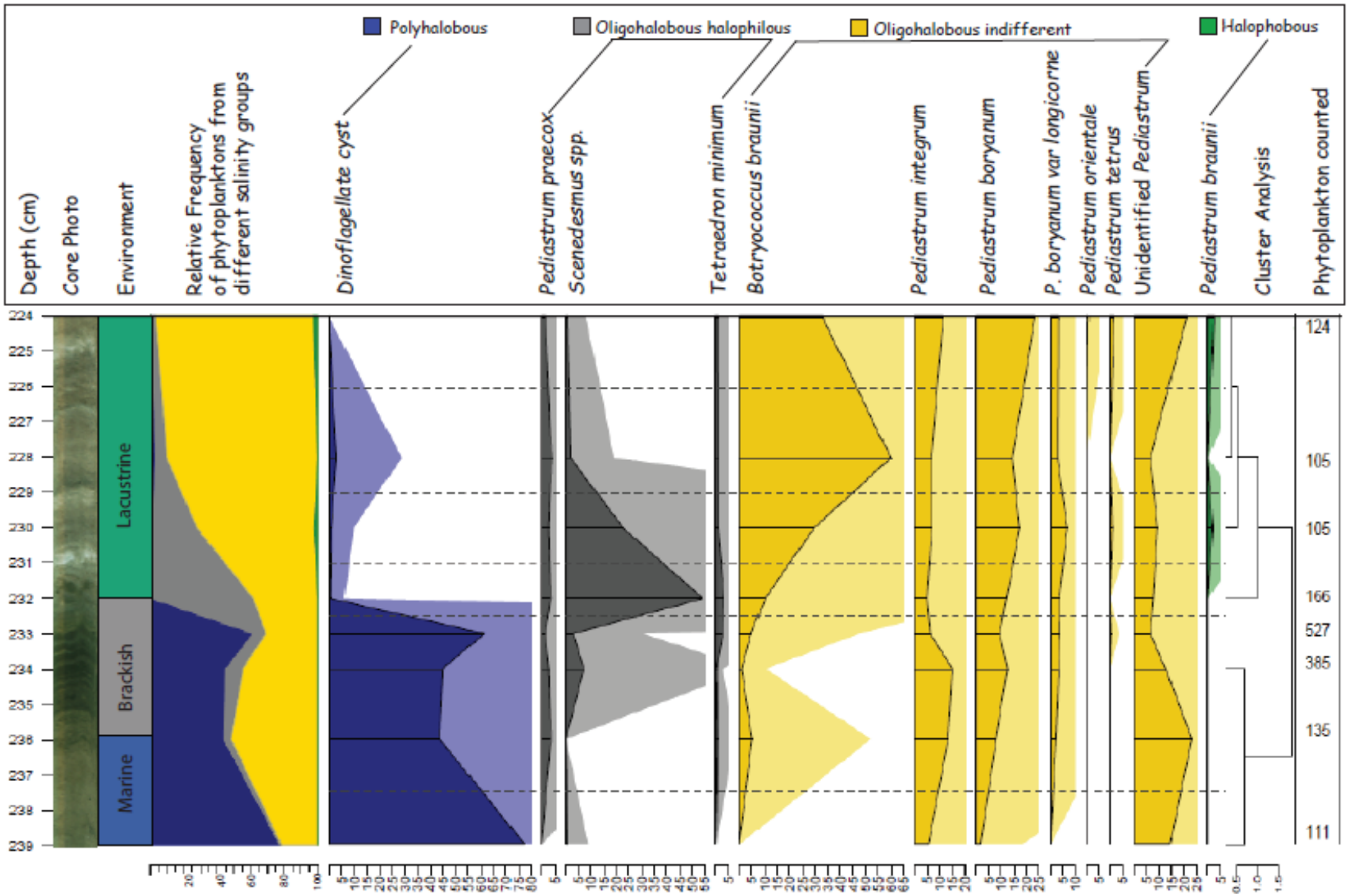

Figure 4.13: Phytoplankton analysis of PÅLP-119. The relative frequency of different salinity tolerant species shows that less salinity tolerant species are more common above the isolation contact (232.5 cm depth). On the right margin of the diagram, the number of phytoplankton found in each depth point is shown.

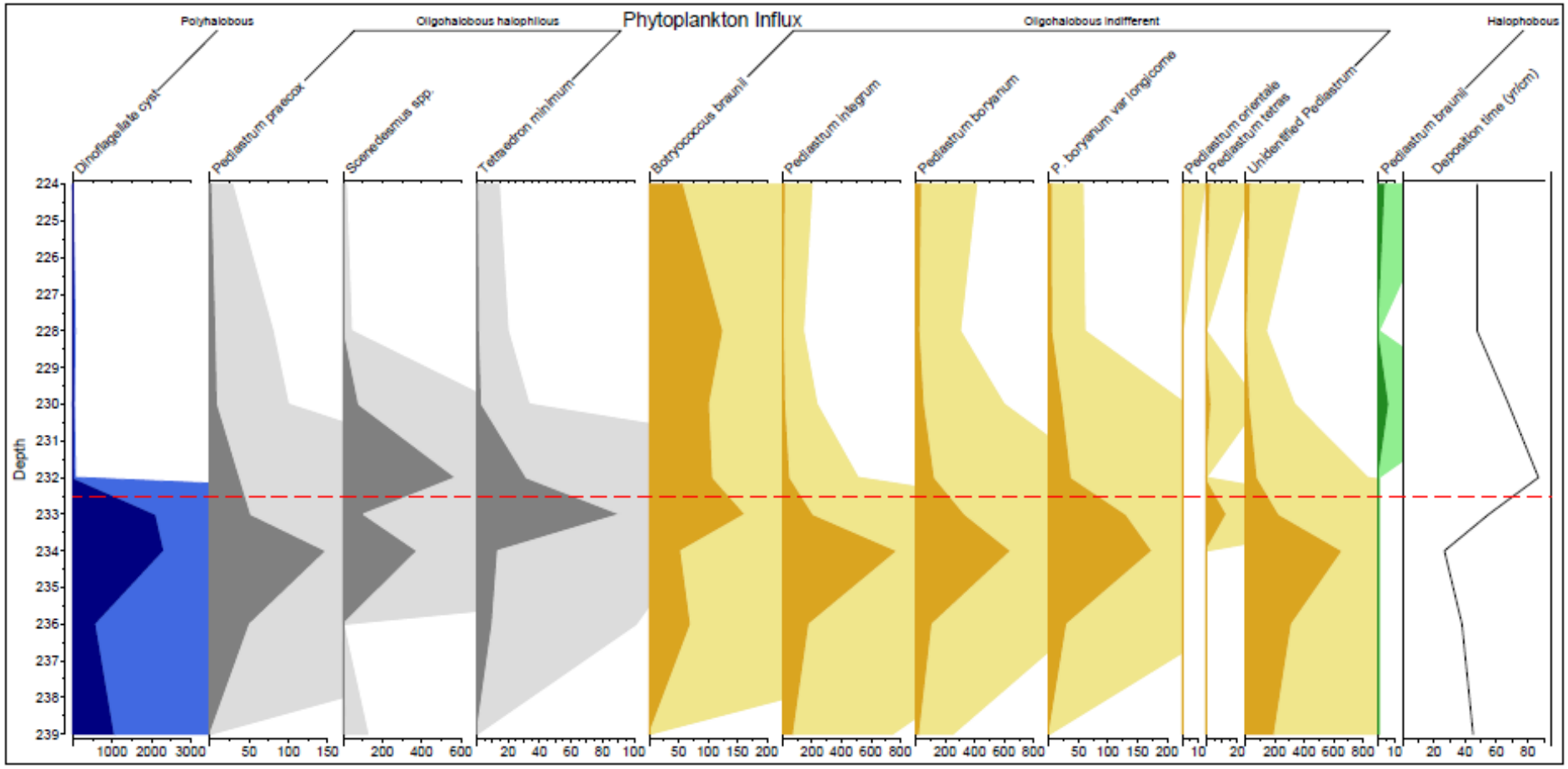

Figure 4.14: Phytoplankton influx analysis of PÅLP-119 shows the number of phytoplankton deposited per 1 cm^3 over time. Influx rate is exaggerated ten times. The exaggerated influx rate is represented here with lighter color along with the dark-colored influx rate for each phytoplankton. The deposition rate (yr/cm) is shown in the right margin of the diagram. The isolation contact is marked with the dotted red line at 232.5 cm depth of the core.

4.2.5. Radiocarbon Dating

The overview of all the results of radiocarbon dating is shown in table 4.4. Both the age range with 68% confidence interval (1σ) and 95% confidence interval (2σ) are shown in table 4.4, but the calibrated dates used in this study are based on the age range of the 95% confidence interval.

Table 4.4: The summary of all radiocarbon dates used in the present study are listed here. In case of depth the median of the sample collection length is mentioned.

PÅLP-119 Depth (cm)	Lab ID	Content in the sample	^{14}C Date (BP)	Calibrated Date (cal BP) 1 σ	Calibrated Date (cal BP) 2 σ	Calibrated Mean (cal BP) 2 σ
179.5	Poz-119828	*Betula pubescens* fruit, *Alnus glutinosa* fruit, *Betula nana* female catkin scale, Leaf fragments, Wood fragments, Twig, *Conifer* needles	3760 ± 30	4085 - 4156	4075 - 4184	4130 ± 55
222.5	Poz-119829	*Betula pubescens* fruit, *Alnus glutinosa* fruit, *Betula nana* female catkin scale, *Pinus sylvestris* bud scale, Leaf fragments, Wood fragments	4980 ± 35	5657 - 5736	5639 - 5753	5695 ± 55
230	Poz-119832	*Betula pubescens* fruit, *Betula nana* female catkin scale, Leaf fragments, Wood fragments	5285 ± 35	6076 - 6117	5987 - 6182	6085 ± 100
234	Poz-119833	*Betula pubescens* fruit, *Alnus glutinosa* fruit, Leaf fragments	5535 ± 35	6292 - 6323	6287 -6398	6340 ± 55
236.6	Poz-119834	*Betula pubescens* fruit, *Alnus glutinosa* fruit, *Betula nana* female catkin scale, Leaf fragments, Wood fragments, Twig	5645 ± 35	6400 - 6474	6387 - 6494	6490 ± 105
239	Poz-119835	*Betula pubescens* fruit, *Alnus glutinosa* fruit, Leaf fragments, Twig	5745 ± 30	6492 - 6566	6467 - 6637	6550 ± 85

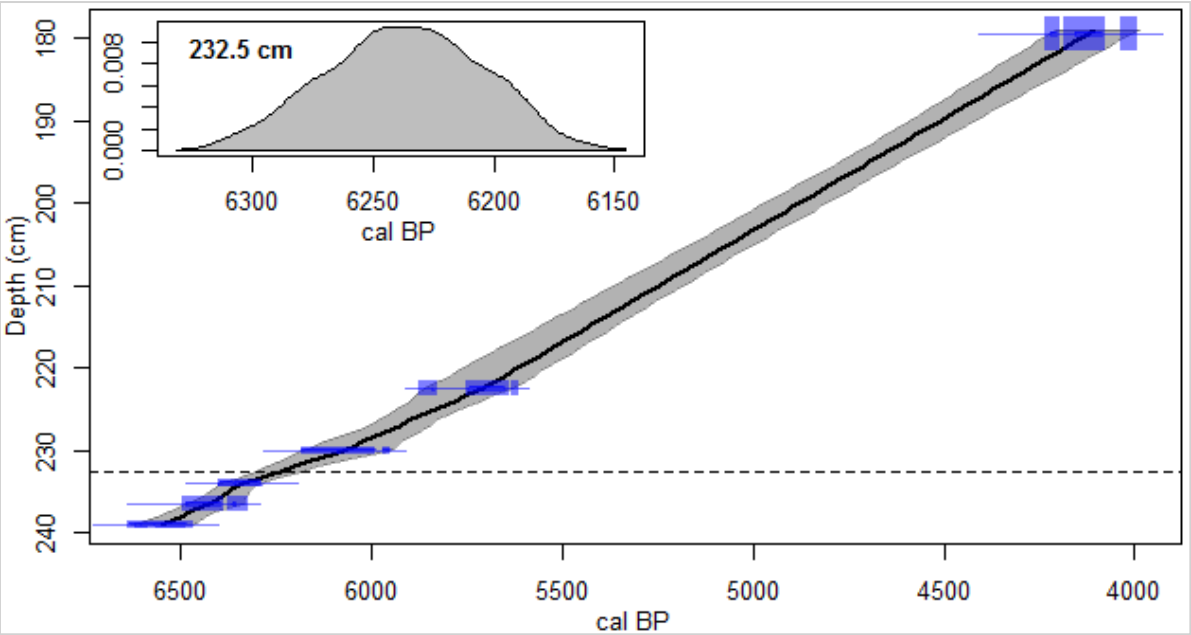

Figure 4.15: The age of the isolation contact found using the age-depth model of Pålsvatnet.

All of the radiocarbon dates were in the right stratigraphical order, so none of the samples were interpreted as outliers. The age-depth model for the lake was developed using a linear interpolation between neighboring levels in the 'clam' package of R (Blaauw, 2010) to get the age of the isolation contact (figure 4.15). Other types of interpolation methods were also tested, but they did not give significantly different results from the linear interpolation model.

As discussed in the previous section, the phytological isolation contact, which represents the most precise brackish-lacustrine transition, was found at a depth of 232.5 cm of the core. The best age of the phytological contact of the basin is found to be 6240 cal BP with a 95% confidence range (average 120 years) from 6300 to 6180 cal BP.

5. Discussion

5.1. Marine Limit

The marine limit is the highest level that the sea reached after deglaciation occurred in an area. The marine limit map (figure 5.1) constructed by the Geological Survey of Norway (NGU), indicates an altitude of around 75 m in the study area (NGU, 2020a). Marthinussen (1962) found shells (and fragments of shells), e.g., *Macoma calcarea* and *Mya truncate*, from different altitudes in the Sandstrand area (located in adjacent Skånland municipality of Evenes), which dated to Allerød interstadial period, and those cannot reflect the postglacial marine limit. The study area is located between the 60 m and 80 m Younger Dryas (YD) isobases (Møller, 1989); however, these isobases only provide a maximum estimate for the marine limit, as the area was deglaciated around 600 years after the YD (Forwick and Vorren, 2002; Lid, 2019), and there has probably been some 'restrained rebound' during this time interval (Benn and Evans, 2013: 237). Thus, the marine limit is expected to be slightly lower than the YD shoreline shown by the isobases.

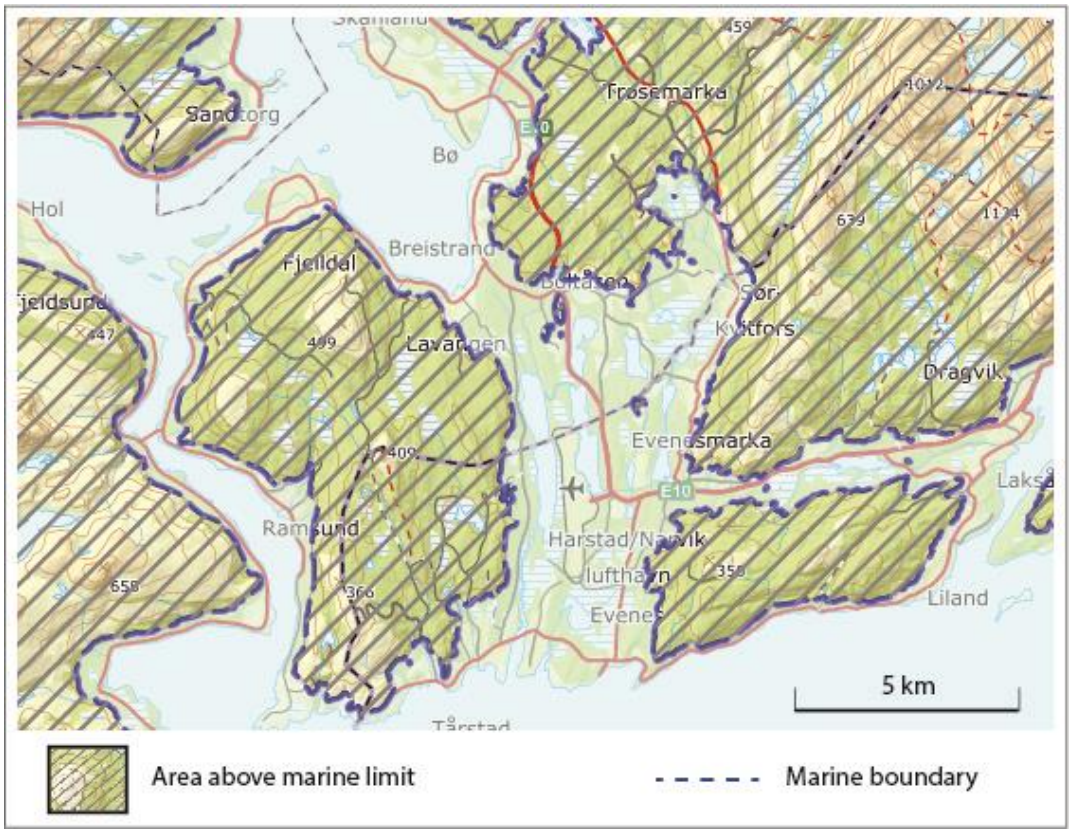

Figure 5.1: The marine limit map from the study area where the places above the marine limit are marked with parallel lines pattern. Map modified from NGU (2020a)

The glaciofluvial delta discovered in the study area, located at the edge of the marine boundary proposed by NGU (2020a), could represent the marine limit of the area more precisely. After adjusting for the tidal influence, the average altitude of the topset-foreset boundary of the delta is found at 75.83 m a.s.l., which is here interpreted as the marine limit of the area. The age of the marine limit (and deglaciation) comes from a basal date (10965 ± 205 cal BP) in Store Trøsevatnet (Lid, 2019), which provides a minimum age of deglaciation of the area. As Store Trøsevatnet is located close to the delta, this date may also represent the time when the delta was formed.

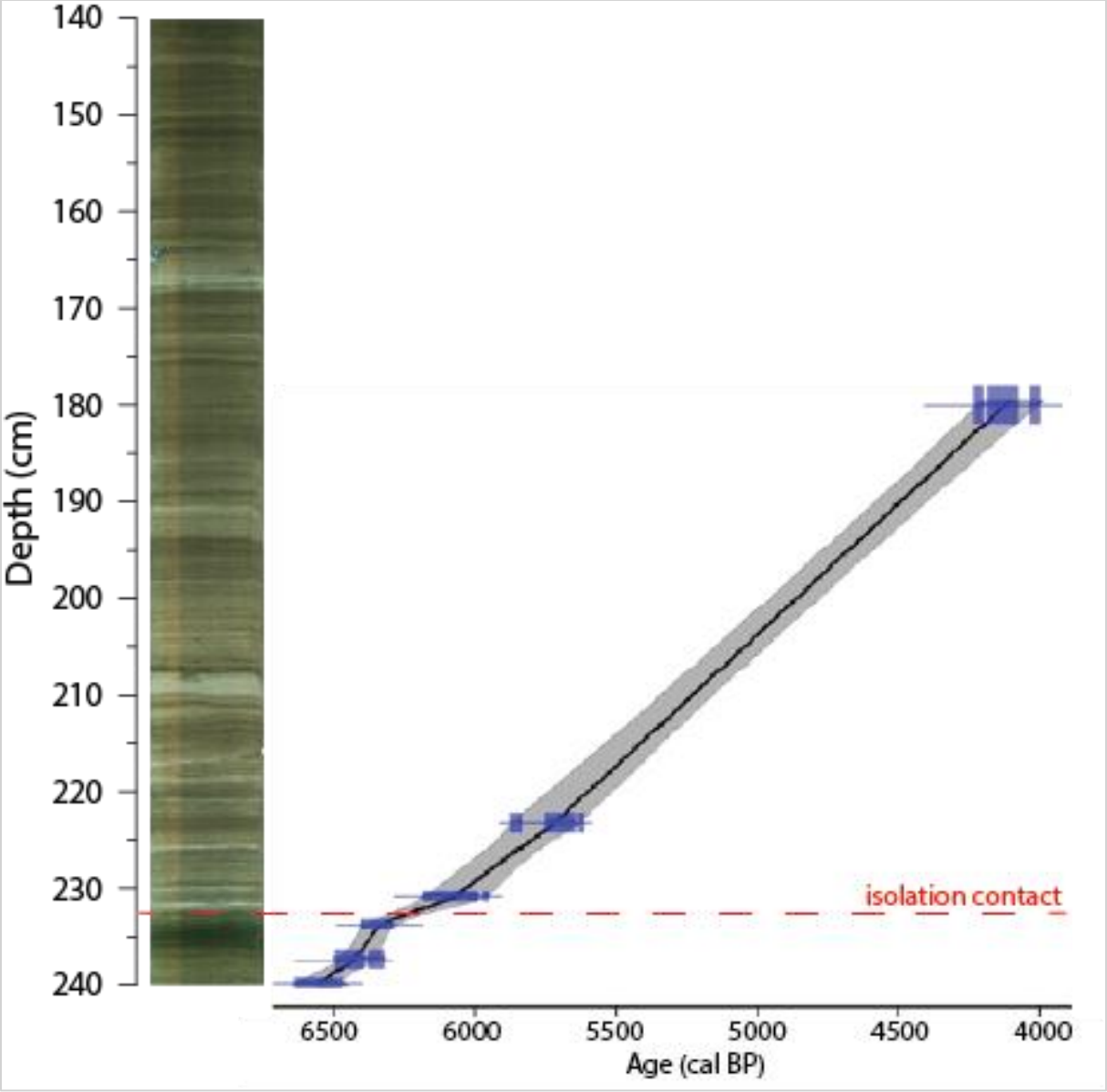

Figure 5.2: Age-depth mode of Pålsvatnet. The default interpolation setting, linear interpolation between neighboring levels, of 'clam' package (Blaauw, 2010) of R found it best fitting for the lake.

5.2. Age-depth Model

The age-depth model (figure 5.2) of Pålsvatnet represents the overall picture of the sedimentation rate the basin experienced throughout the dated range. The lake experienced a typical high sedimentation rate (figure 5.3) during the marine and brackish phase, whereas the sedimentation rate decreased after it became lacustrine.

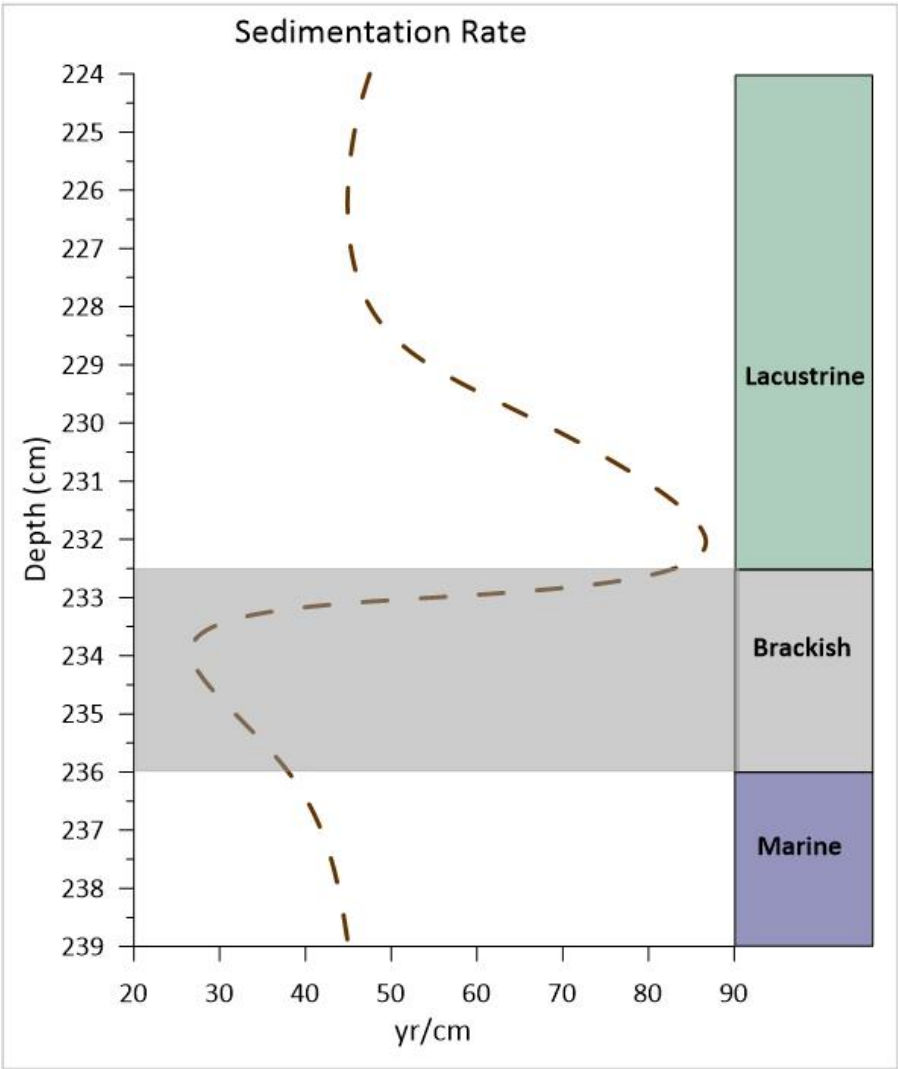

Figure 5.3: The sedimentation rate of Pålsvatnet. A high rate of sedimentation is observed during the brackish phase of the lake. Data is extracted from influx analysis in the Tilia software.

5.3. Relative Sea-level Curve

A relative sea-level (RSL) curve can be improved by adding more sea-level index points, and a dated isolation contact can thus provide one additional data point in a sea-level curve. To reconstruct a better representative RSL curve for Evenes, the results from previous sea-level studies from the same region are incorporated along with the outcome of this study. The distances between different sites (table 5.1) measured perpendicular to the isobases (figure 5.4), the imaginary contour lines between the places of uniform emergence over the same time scale (Svendsen and Mangerud, 1987), are used to correct for tilted uplift. The curve needs to be drawn with reference to one of the study sites, in this case, Pålsvatnet, and the altitude of the other sea-level index points are therefore adjusted based on the distance from the reference site perpendicular to isobases and estimated tilt of the shoreline at the time corresponding to the age of the sea-level index point.

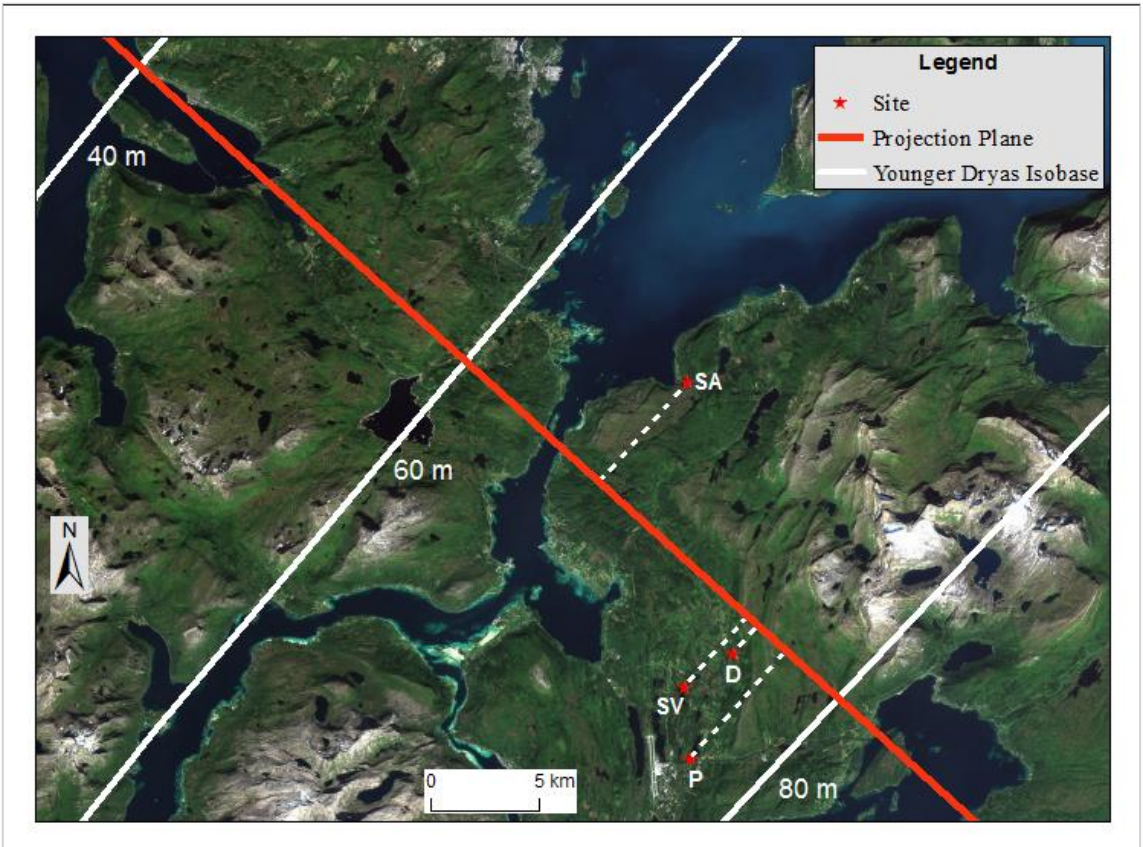

Figure 5.4: Location of different sites ('D' = glaciofluvial delta, 'SV' = Svartvatnet, 'P' = Pålsvatnet, and 'SA' = Sandstrand) used to draw the RSL curve and their location along with the projection plane drawn perpendicular to isobases. The distances between sites are measured in terms of their position in the projection plane. The isobases are traced from Møller (1989). The background aerial photo is from Geonorge (2020).

The RSL curve (figure 5.5) is drawn according to the reference site of the Pålsvatnet basin threshold, using the altitude and age of isolation from this study. In the curve, three other sea-level index points are also included: 1) the topset of the glaciofluvial delta in Kvitfors, 2) the isolation of Svartvatnet (Lid, 2019), and 3) a marine terrace in Sandstrand (Møller, 1989).

As discussed in chapter 4, the altitude of the topset-foreset boundary of the glaciofluvial delta is found at 74.49 m a.s.l., and the altitude was required to be adjusted according to the tidal influence. Because a glaciofluvial delta usually gets more temporary sediment during high tide, and deposits are removed during low tide (Eilertsen et al., 2011), high tide is not corresponding to the intertidal flat of delta (Hori et al., 2001). The indicative meaning of the topset-foreset boundary is therefore considered here to be the mean low water spring tide (MLWST), in contrast to an isolation basin, where the indicative meaning of the isolation contact is considered to be mean high water spring tide (MHWST) (Vasskog et al., 2019). The MLWST of the study area is 1.34 m lower than the present mean sea level (Kartverket, 2020), and by adding this, the altitude of the glaciofluvial delta is calculated to 75.83 m a.s.l., which will then represent the paleo mean sea level. In terms of the projection plane of the isobases, the distance between Pålsvatnet and the glaciofluvial delta is calculated to 1.91 km (table 5.1). This altitude is adjusted considering a gradient of 0.86 m/km for the tilted shoreline where the gradient was calculated by dividing the altitude difference by the measured distance (23.3 km) between the YD isobases along the projection plane (figure 5.4). The final altitude for this sea-level index point, corrected for tidal levels and tilted uplift, is thus 74.30. As no radiocarbon dating was done from the glaciofluvial delta, the age of the glaciofluvial delta sea-level index point was incorporated from the Store Trøsevatnet (figure 2.2, chapter 2) from the study of Lid (2019). Store Trøsevatnet is a bog located 73.5 m above mean sea level where no marine phytoplankton was found, which means the lake is located above the marine limit. Because this only gives rough maximum value for the marine limit, Lid (2019) used around ± 5 m uncertainty for the altitude for that sea-level index point in the sea-level curve of Skånland, the municipality located adjacent north of the Evenes municipality. As Store Trøsevatnet is located only a few kilometers away from the delta, the basal radiocarbon dating result of Store Trøsevatnet is used for the minimum age of deglaciation and thus also the sea-level index point of the glaciofluvial delta, which is considered to have formed just after deglaciation. The calibrated age of the radiocarbon dating is 10965 ± 205, where the error range covers two standard deviations of the dating result (Lid, 2019).

Svartvatnet is an isolation basin that is located 37.6 m a.s.l. (altitude of the threshold), and the altitude needs to be adjusted for the tilted shoreline to the reference point at Pålsvatnet. In terms of the projection plane drawn perpendicular to the isobases (figure 5.4), the distance between the thresholds of Pålsvatnet and Svartvatnet is measured to 2.39 km. Using both terrestrial and marine materials (shells) the age of isolation was calculated to 9315 ± 100 cal BP (Lid, 2019), meaning that the tilt of the shoreline at that time was certainly larger than for the Tapes shoreline. In the absence of no previous studies for shoreline gradient of this period the average gradient between the YD shoreline (0.86 m/km) and Tapes shoreline (0.14 m/km) for Lofoten and Vesterålen (Møller, 1984) was used to adjust the tilt of Svartvatnet sea-level index point, i.e., a gradient of 0.50 m/km (table 5.1).

Table 5.1: Measurements and adjustments of altitudes of the sea-level index points. The adjustment for the tilted shoreline is done on the basis of the location of a site in the context of Pålsvatnet.

Site	Altitude (m a.s.l.)	Distance from Pålsvatnet (km)	Gradient (m/km)	Adjusted altitude for the sea-level curve (m a.s.l.)
Glaciofluvial delta	75.83	1.78	0.86	74.30
Svartvatnet	37.6	2.39	0.50	38.80
Pålsvatnet	22.4	-	-	22.4
Sandstrand	12	11.71	0.14	13.64

The age and altitude of the Pålsvatnet sea-level index point are found from this study. As discussed in chapter 4, the elevation of the basin threshold needs to be adjusted for tidal influence. For isolation basins, the high tide is usually considered as the indicative meaning of an isolation contact, because, even after a basin is elevated above mean sea level, it can get input of saline water during high tide (Kjemperud, 1986; Svendsen and Mangerud, 1987; Lohne et al., 2007; Long et al., 2011; Romundset et al., 2018; Vasskog et al., 2019). The mean high water spring tide (MHWST) of the area of 1.34 m (Kartverket, 2020), is therefore subtracted here to adjust for the tidal influence. The final adjusted altitude for this sea-level index point is 22.4 m above mean sea level. The basin was isolated 6240 ± 60 cal BP, and this is used as the age of this sea-level index point.

Sandstrand is located in Skånland municipality, located around 11.71 km distance from Pålsvatnet towards the coast perpendicular to the isobases. For the Sandstrand sea-level index point, the data from Møller (1989) is used (figure 5.4). The sea-level index point of Sandstrand

comes from a terrace located around 16.5 m above mean sea level. As the terrace was interpreted as a storm deposit and the corresponding sea level was estimated to be 4 - 5 m lower than this level, the sea-level index point was fixed at 12 m above sea level in the Sandstarnd curve (Møller, 1989). Considering 12 m above mean sea level as altitude for the Sandstrand sea-level index point, the height is also adjusted considering the distance (11.71 km) perpendicular to isobases between the sites (Pålsvatnet and Sandstrand) (figure 5.4), and Tapes shoreline gradient (0.14 m/km) for Lofoten and Vesterålen (Møller, 1984). Thus the final altitude for this index point in the relative sea-level curve of Evenes is 13.64 m above mean sea level (table 5.1). A marine shell (*Arctica islandica*) was collected and dated for the age of the terrace, and which was found to be 4010 ± 80 ^{14}C BP. The local offset from the global marine reservoir age, known as ΔR, for this area is estimated to 71 ± 21 years (Mangerud et al., 2006). Considering the global marine reservoir age and the local ΔR, the date was calibrated to 3940 ± 115 cal BP (Lid, 2019). The same age is used for this sea-level index point in the relative sea-level curve of this study.

5.3.1. Altitudinal Error

Following the below-mentioned equation (1) from the supporting information of Vasskog et al. (2019), the altitudinal error limit is calculated to ± 0.56 m and ± 0.39 m for the glaciofluvial delta and the threshold of Pålsvatnet respectively (table 5.2).

$$\text{Error} = \sqrt[2]{(measurement\ error)^2 + (tilted\ shoreline)^2 + (indicative\ meaning)^2} \quad \ldots (1)$$

Here, measurement error is considered to be half of the one standard deviation of all measurements, and the error of tilted shoreline is 15% of the tilt given in table 5.1, following Vasskog et al. (2019). To allow for an uncertainty in the interpretation of the indicative meaning, an error of half of the difference between the lowest astronomical tide (LAT) and the mean low water spring tide (MLWST) of the area is added for the glaciofluvial delta. For the lake threshold, this is calculated as half of the difference the highest astronomical tide (HAT) and the mean high water spring tide (MHWST), instead of the difference between LAT and MLWST.

Table 5.2: Measurements of errors associated with the delta and the outlet investigated in the present study. Total vertical error is calculated using the equation (1).

Sea-level Index Point	Measurement Error (m)	Tilted Shoreline (m)	Indicative Meaning (m)	Total Error (m)
Glaciofluvial Delta	0.45	0.29	0.25	± 0.58
Pålsvatnet	0.24	-	0.31	± 0.39

For Svartvatnet and Sandstrand sea-level index points, the error limits are ± 1.3 m and ± 2.5 m, respectively, keeping them the same as from the previous studies (Møller, 1989; Lid, 2019).

5.3.2. Regression Rate

Four index points are plotted, and the curve is drawn by connecting them in the best possible way to reflect a gradual change in the rate of relative sea-level change. The regression rate (R), which represents how fast the relative sea-level fell during a specified period, is calculated as the average rate between two consecutive sea-level index points considering the change of altitude and time. From 10965 ± 205 cal BP to 9314 ± 100 cal BP, the relative sea-level of Evenes dropped by around 36.36 m with an average regression rate of 2.15 cm/yr. From 9314 ± 100 cal BP to 6240 ± 60 cal BP, the fall of relative sea level was comparatively slower (R = 0.53 cm/yr) than the period just after deglaciation. The higher rate of eustatic sea-level rise and a gradually lower rate of land uplift contributed to Tapes transgression in many coastal areas of northern Norway during the same period of time (Vorren and Moe, 1986; Rasmussen et al., 2018). Being located a bit further inland in the context of the former ice-sheet margin, the Evenes area had a slower rate of fall instead of experiencing a transgression during this period. The rate of relative sea-level fall gradually became slower after 6240 ± 60 cal BP. The rate of fall was 0.38 cm/yr from 6240 ±60 cal BP to 3940 ± 115 cal BP. The regression rate drops to 0.35 cm/yr after 3940 ± 115 cal BP to the present time. The relative sea-level curve of Evenes reflects the gradual fall in sea-level after the area became ice-free mainly due to the gacio-isostatic rebound. Note, however, that these regression rates are only the average values between index points, which assumes linear interpolation. In figure 5.5, the RSL curve has been drawn with gradual changes that are considered to be more realistic, and from this, it is indicated that the minimum regression rate could possibly have occurred just prior to the isolation of Pålsvatnet, at the time that areas further west experienced a transgression.

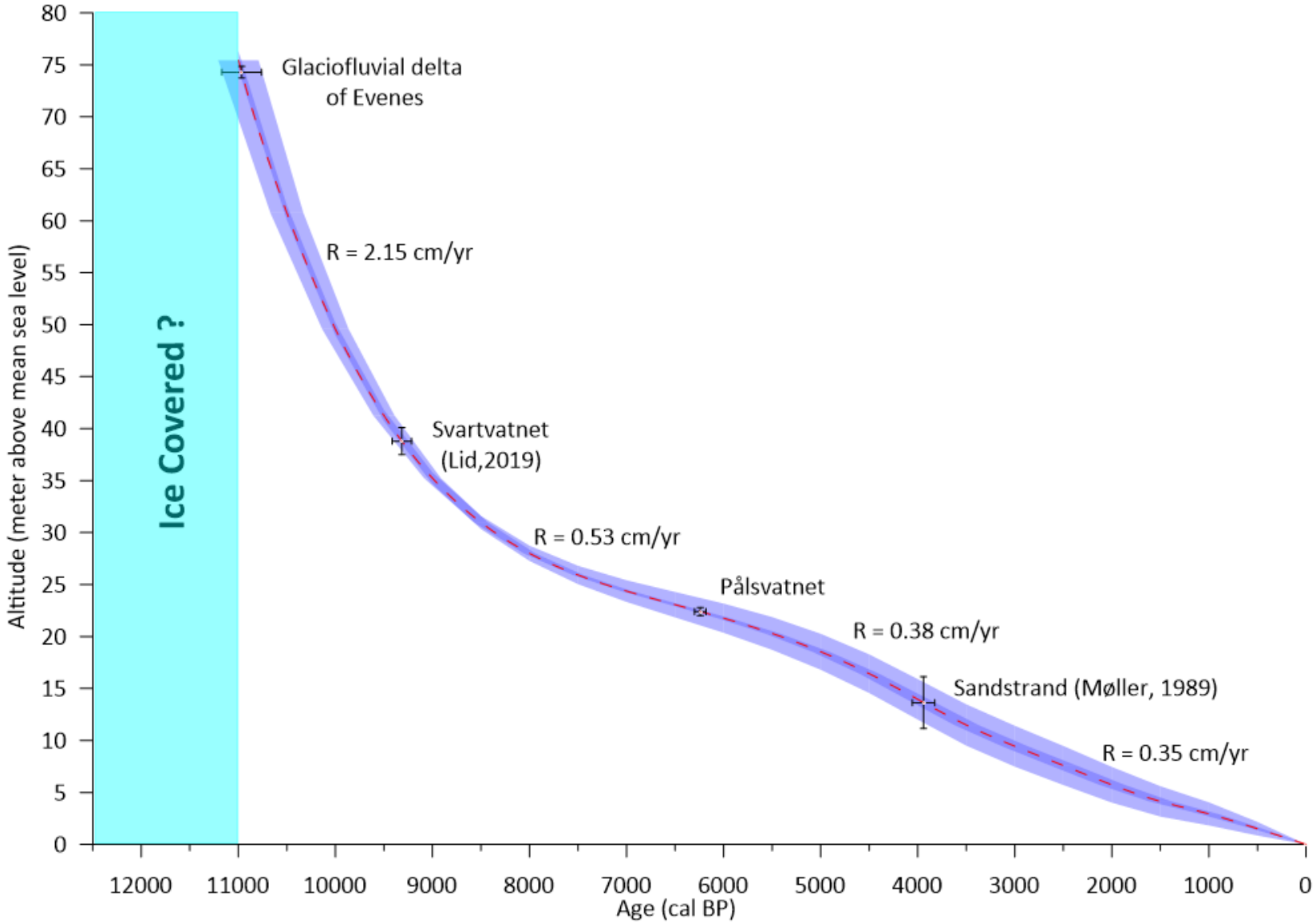

Figure 5.5: The RSL curve of Evenes; the regression rate is calculated based on two consecutive sea-level index points, and errors are interpolated from the reconstructed ones.

5.4. Factors Contributing to Relative Sea-level Change

For the relative sea-level change, vertical land movement due to isostatic/tectonic movement contributes most apart from the contribution from the eustatic sea-level change (Mörner, 1976; Shennan et al., 2015). If the eustatic contribution to the relative sea-level change can be separated, the contribution of glacio-isostatic rebound (vertical land movement) and geoidal changes can be inferred (Lohne et al., 2007). The contributions from a glacio-isostatic rebound and geoidal changes cannot be separated empirically (Vasskog et al., 2019). However, the contribution from gravitational changes was probably very small following the YD (Tarasov, 2013), so the residual curve after subtracting eustatic sea level could roughly be considered as the contribution of land uplift. Lambeck et al. (2014) calculated the eustatic sea-level change from the last glacial maximum to the Holocene. The 500-year resolution data (table 5.3) of Lambeck et al. (2014) was subtracted from the data of this study, and the residual curve was termed as the inferred land uplift during the same period (figure 5.6). The same principle was also used to estimate the approximate contribution of local land uplift to relative sea-level change in Sotra, western Norway (Lohne et al., 2007), and southern Karmøy, south-west Norway (Vasskog et al., 2019).

The inferred land uplift curve indicates around 130 m postglacial land uplift that the area has experienced throughout the Holocene (figure 5.6). It also reflects high land uplift from the beginning of the Holocene (figure 5.6), due to glacio-isostatic rebound as a response to the high rate of melting. A high rate of eustatic sea-level rise during the meltwater pulse 1C (MP1C) (Gornitz, 2013: 132-133), may reduce the impact of land uplift; resulting in a reduced rate of relative sea-level fall around 8000 cal BP compared to the period just after the start of the Holocene (figure 5.4). Meltwater pulses are periods of rapid global sea-level rise when ocean levels may have climbed several meters within a few hundred years; MP1C is the most recent meltwater pulse and occurred from ~8200 cal BP to ~7600 cal BP, when global sea-level rose by ~ 6 m (Cronin et al., 2007). After the disappearance of the Laurentide ice sheet at ~ 8000 cal BP (Bryson et al., 1969), the eustatic contributions to the relative sea-level change has been reducing gradually since then. As the Scandinavian ice sheet melted before the Laurentide ice sheet (Carcaillet et al., 2012), the contribution from the glacio-isostatic rebound has been diminishing gently since the area became ice-free.

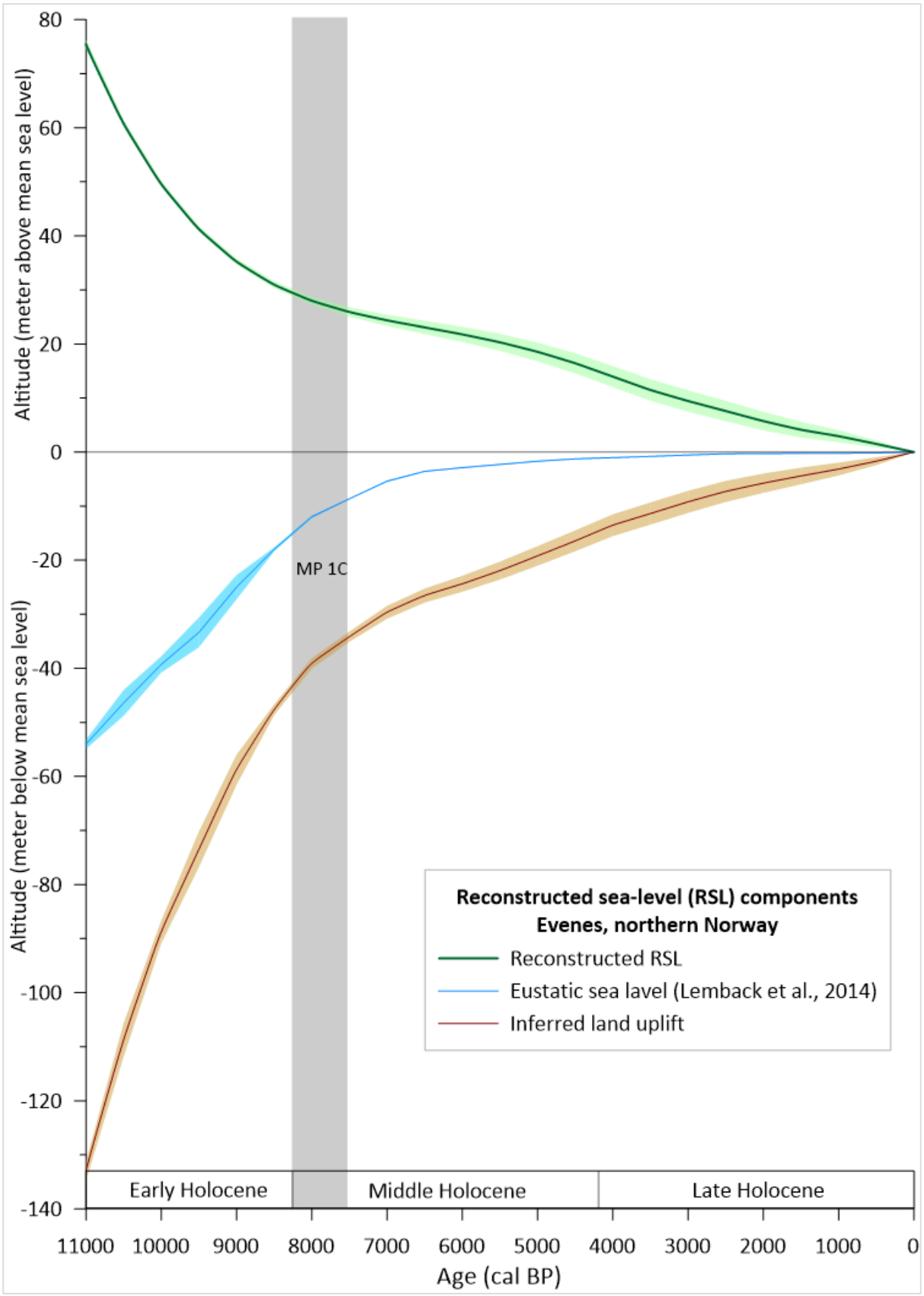

Figure 5.6: The contribution of the inferred land uplift rate for the relative sea-level change of the area is extracted by subtracting the eustatic sea-level change from the relative sea-level of the area.

Table 5.3: Reconstructed sea-level (RSL) components of Evenes, northern Norway; inferred land uplift is calculated subtracting the mean eustatic sea-level contributions from the reconstructed relative sea-level change.

Age	Reconstructed relative sea-level change		Mean Eustatic sea level, Lambeck et al. (2014)		Inferred land uplift	
(cal BP)	Reconstructed (m)	Error ± (m)	Mean Eustatic sea level (m)	Error ± (m)	Inferred (m)	Error ± (m)
0	0	0	0	0	0	0
500	1.51	0.65	-0.17	0.07	-1.68	0.72
1000	2.94	1.11	-0.2	0.07	-3.14	1.18
1500	4.14	1.46	-0.23	0.07	-4.41	1.53
2000	5.73	1.72	-0.26	0.07	-5.75	1.79
2500	7.59	1.88	-0.32	0.07	-7.28	1.95
3000	9.45	1.97	-0.54	0.07	-9.20	2.04
3500	11.33	1.99	-0.8	0.07	-11.37	2.06
4000	13.81	1.95	-1.02	0.07	-13.53	2.02
4500	16.24	1.86	-1.25	0.07	-16.42	1.93
5000	18.45	1.73	-1.69	0.07	-19.20	1.80
5500	20.35	1.58	-2.28	0.07	-21.92	1.65
6000	21.90	1.41	-2.88	0.07	-24.36	1.48
6500	23.16	1.23	-3.56	0.07	-26.54	1.30
7000	24.31	1.05	-5.39	0.14	-29.64	1.19
7500	25.50	0.88	-8.64	0.07	-34.14	0.95
8000	27.38	0.74	-11.97	0.22	-39.11	0.96
8500	30.11	0.63	-17.99	0.36	-47.66	0.99
9000	34.27	0.55	-24.99	2.23	-58.76	2.78
9500	40.38	0.54	-33.35	2.74	-73.48	3.28
10000	48.95	0.58	-39.28	1.51	-88.75	2.09
10500	60.43	0.70	-46.39	2.38	-108.71	3.08
11000	75.18	0.90	-54.02	0.87	-132.94	1.77

5.5. Shoreline Diagram

To construct an equidistant shoreline diagram of an area, there are three prerequisites: (1) isobase direction should be known, (2) the isobases must be parallel within the area, and (3) isobase direction was unchanged for the period shorelines were drawn (Svendsen and Mangerud, 1987). The Younger Drays isobases (figure 5.7) were found almost parallel (Møller, 1989). Moreover, the Holocene Tapes isobases (Møller, 1989) also remain well aligned to the Younger Dryas isobases. Based on the projection plane (figure 5.7), the distance between the sites with RSL curves could be measured perpendicular to the isobases.

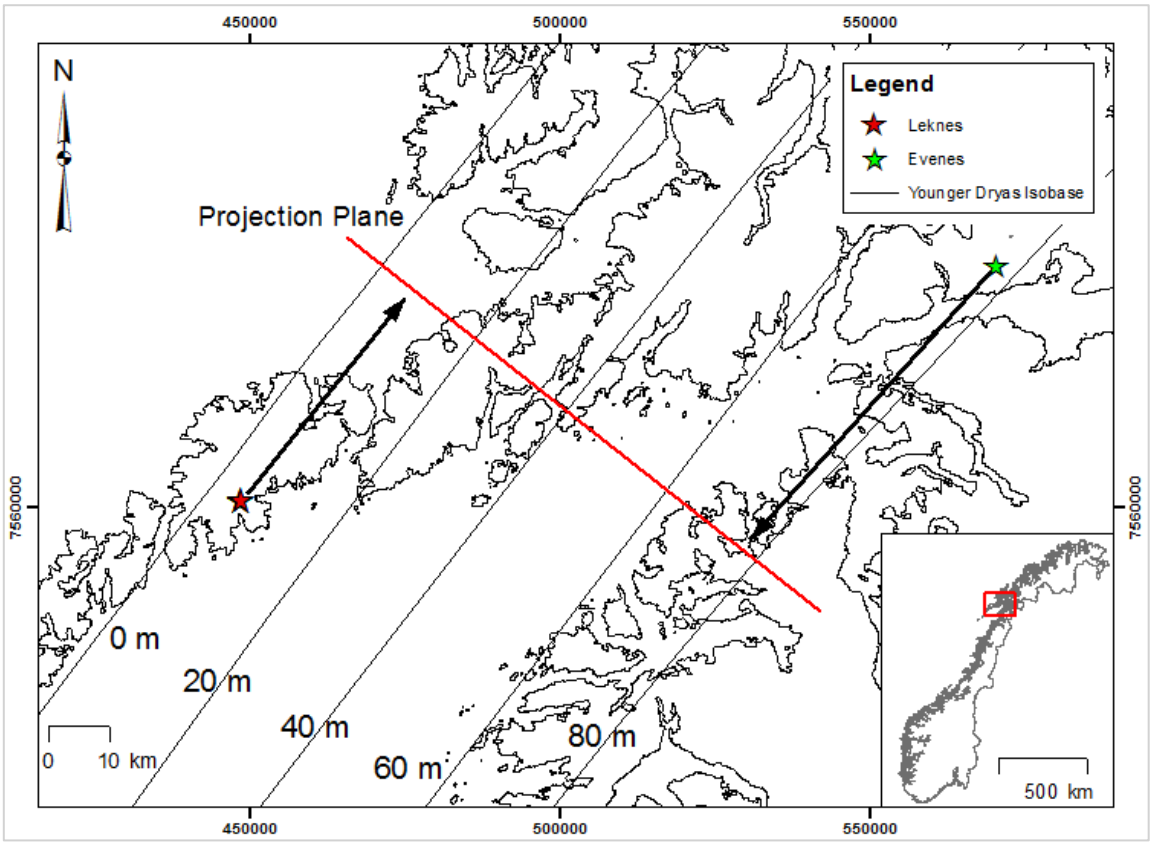

Figure 5.7: Map of the area from Leknes and Evenes with a keymap of Norway. Younger Dryas isobases are traced from Møller (1989). The distance perpendicular to isobases between the two sites is 67.89 km. Shapefile of Norway was downloaded from (Hijmans, 2020).

There needs to be at least two RSL curves available from the region where a shoreline diagram is to be constructed. Here, the relative sea-level curve from Leknes (Midtun, 2019) and the relative sea-level curve of this study (figure 5.5) are used to construct a shoreline diagram (figure 5.8). The distance between the sites perpendicular to the isobases was measured to 67.89 km, and shorelines for ten distinct periods (from 10,000 cal BP to 1000 cal BP) were drawn. The intersection between an older shoreline and a younger shoreline represents a transgression for the corresponding area outside the intersection. It could be said from the shoreline diagram that there was no Holocene Tapes transgression that occurred beyond around 40 km distance towards the mainland from Leknes. The Tapes transgression reached its maximum at 6000 ^{14}C BP (~7000 cal BP) at Vesterålen, northern Norway (Møller, 1986). From the shoreline diagram (figure 5.8), it is seen that the 7000 cal BP shoreline intersects by the 8000 cal BP, the 9000 cal BP and the 10,000 cal BP shorelines within around 25 to 50 km distance from Evenes towards the sea, which represents those areas experienced Tapes transgression around 7000 cal BP. Dividing the difference between the sea-levels of the sites for a particular age by the distance between the sites, the gradients (m/km) of shorelines can also be calculated. Based

on the constructed shoreline diagram, shoreline gradients between Leknes and Evenes are calculated to 0.79 m/km, 0.54 m/km, 0.37 m/km, 0.24 m/km, 0.22 m/km, 0.20 m/km. 0.15 m/km, 0.10 m/km, 0.06 m/km and 0.04 m/km for the periods 10,000 cal BP, 9000 cal BP, 8000 cal BP, 7000 cal BP, 6000 cal BP, 5000 cal BP, 4000 cal BP, 3000 cal BP, 2000 cal BP, and 1000 cal BP, respectively.

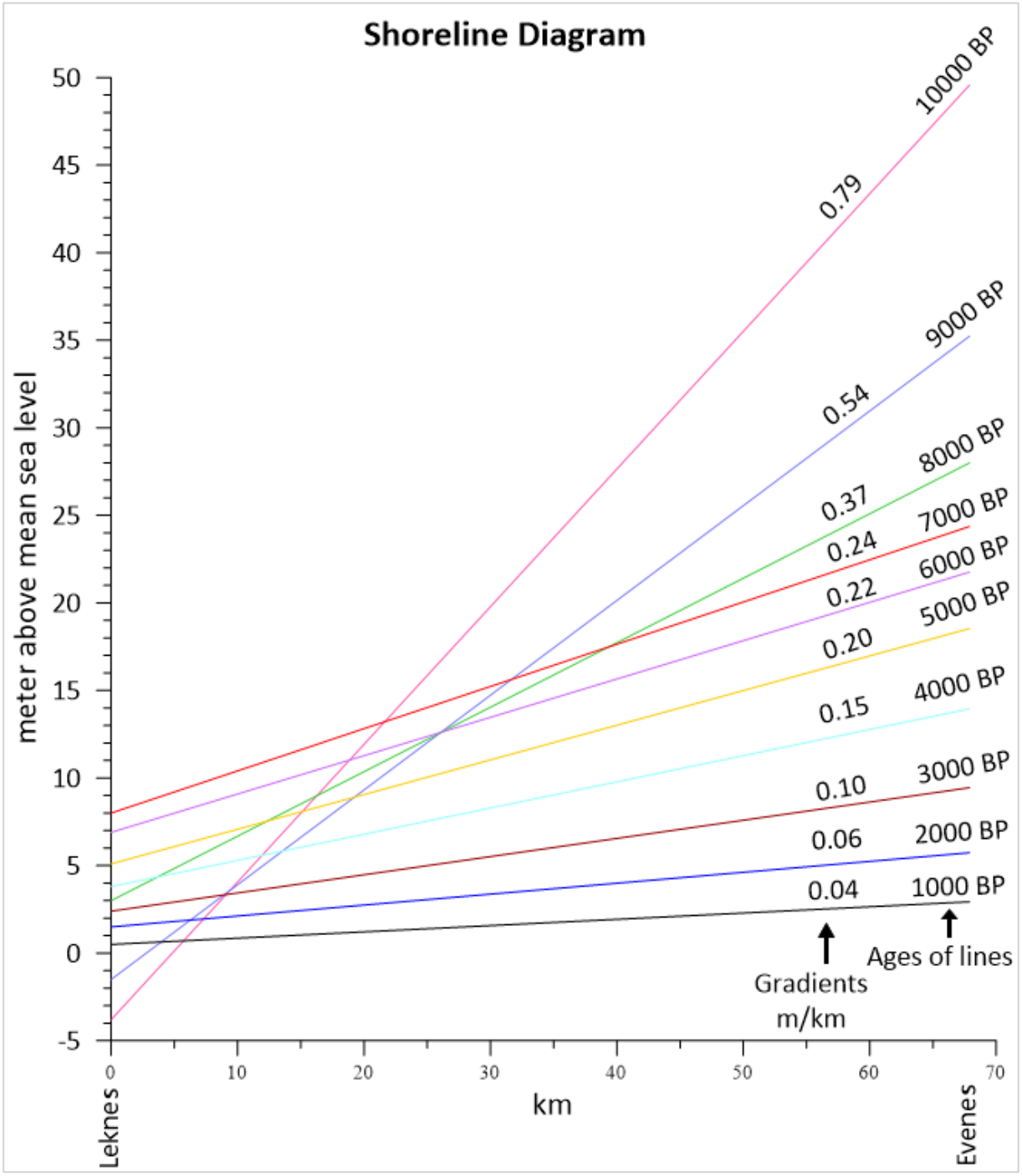

Figure 5.8: Shoreline diagram is developed for the area between Leknes and Evenes using the sea-level diagram study of Midtun (2019) and the sea-level curve of this study (figure 5.4). Calibrated ages are represented here.

The shoreline diagram can be used to calculate rough RSL curves for all areas located along the projection plane within the diagram. Following the same principle used by Svendsen and Mangerud (1987) for western Norway, a total of six relative sea-level curves (figure 5.9) are derived from the shoreline diagram (figure 5.8). The sea-level curves are constructed for every 10 km from Leknes along the projection plane by reading off the altitude of the shoreline of different ages. This diagram (figure 5.9) can simply be used to foresee the different histories of sea-level along the profile of the shoreline diagram (figure 5.8).

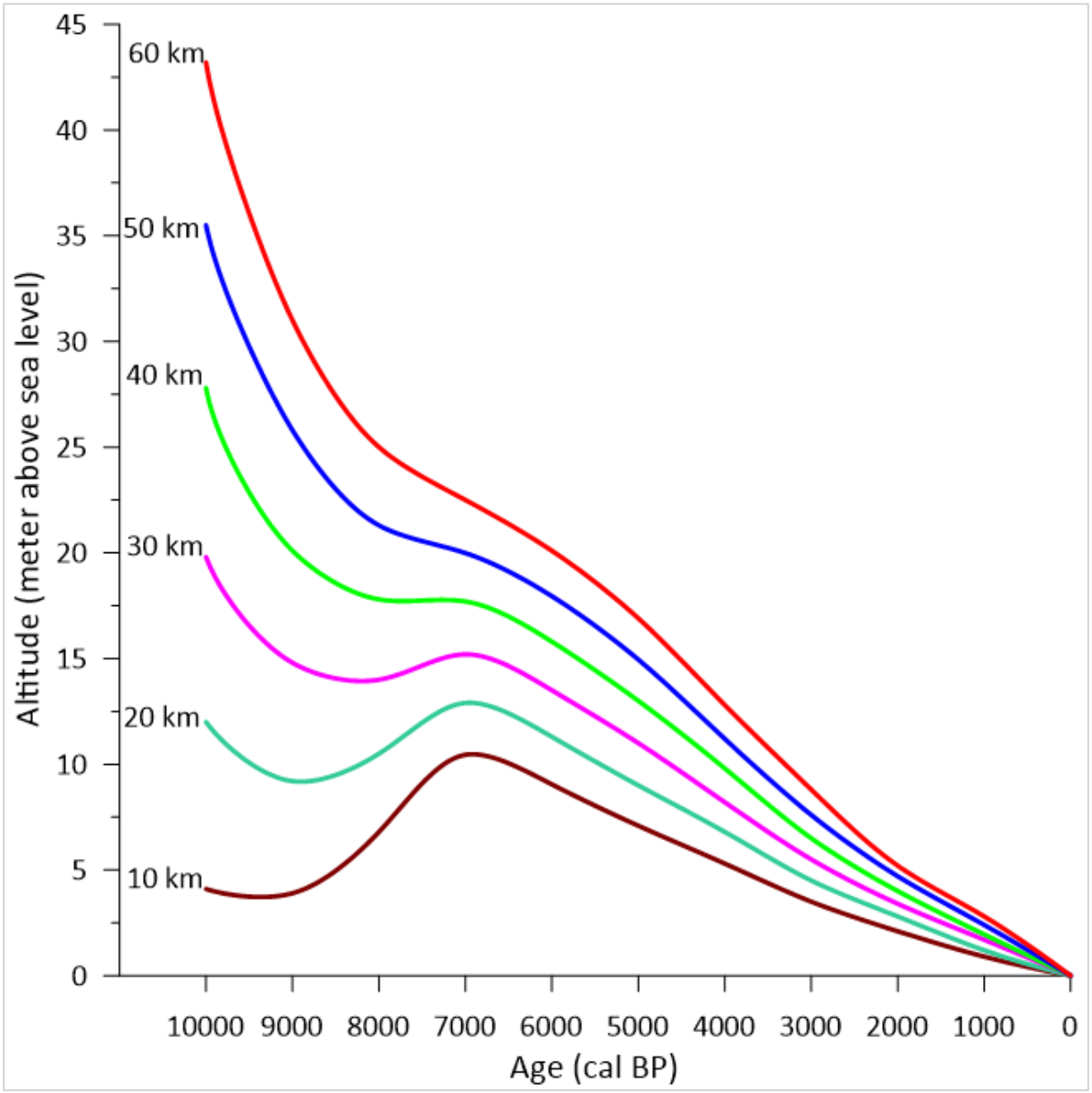

Figure 5.9: A total of six sea-level curves is constructed along the profile of the shoreline diagram (figure 5.8) for every 10 km from Leknes.

5.6. The Storegga Tsunami

The Storegga tsunami was triggered by a submarine slide (Haflidason et al., 2005), which is the largest known Holocene slide on the Earth's surface (Bondevik et al., 2012). From the deposits of the event, the tsunami has been reconstructed from coastal areas of the Norwegian sea (figure 5.10), Scotland, Greenland, Faroe islands and Shetland islands (Svendsen and Mangerud, 1990; Haflidason et al., 2004; Bondevik et al., 2005; Haflidason et al., 2005; Bondevik et al., 2012; Vasskog et al., 2013; Rasmussen et al., 2018). The Storegga slide covered the vast extent (95 000 km^2) of the affected area and displaced a massive amount of deposits (2400 – 3200 km^3 sediments) that made the event distinctly recognizable and found useful as a stratigraphic marker (Haflidason et al., 2005; Bondevik et al., 2012). Because of the giant wavelength of about 600 – 800 km, the Storegga tsunami deposits have been identified in marine basins and lakes along the coast of Norway (Vasskog et al., 2013). Radiocarbon dating from above and below the tsunami layer in terrestrial archives gave a precise age estimate for the event of 8120 -8175 years before 1950 AD (Bondevik et al., 2012). The Storegga tsunami wave reached up to more than 20 m above the mean sea level of that time in the Shetland islands (Bondevik et al., 2012). The minimum and maximum range of run-up height relative to the mean sea level at the corresponding time has been calculated for several sites around the North-Atlantic (Bondevik et al., 2012) and is depicted in figure 5.8.

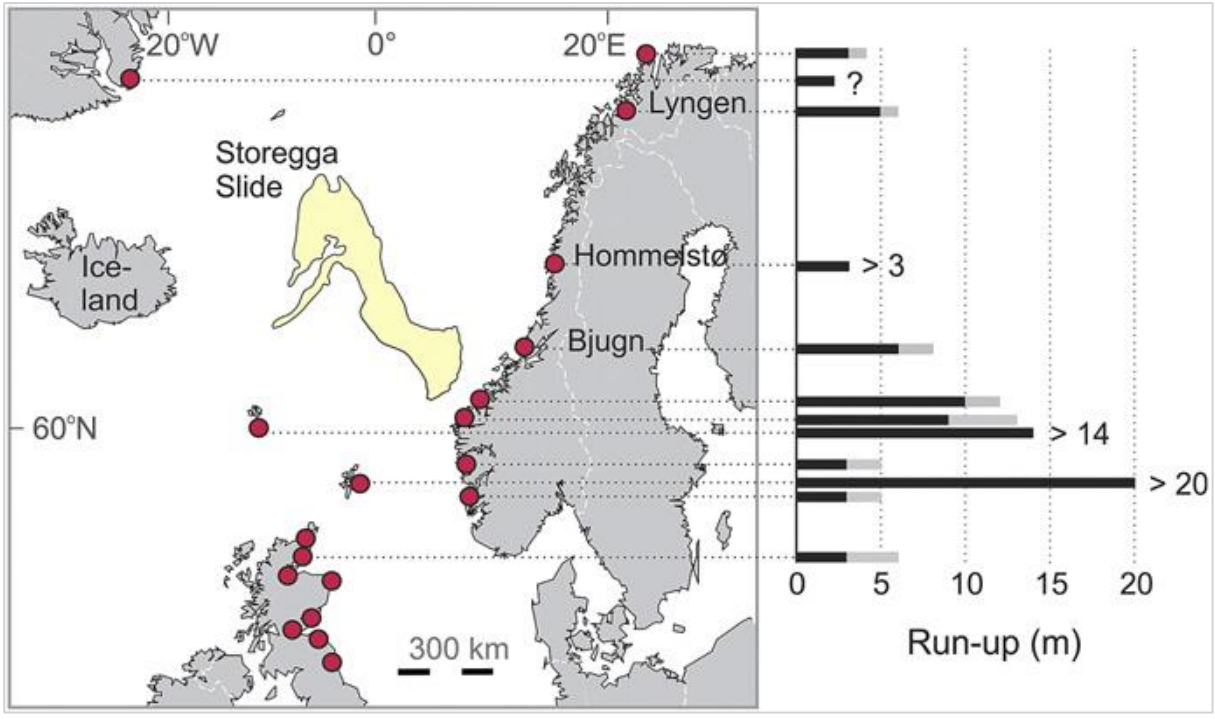

Figure 5.10: Red dot shows the places giant Storegga tsunami deposit in Norwegian sea (left); reconstructed run-up heights (black line = minimum, grey line = maximum) from different field experiences (Bondevik et al., 2012)

5.6.1. The Storegga Tsunami at Pålsvatnet

Between the two cores retrieved from Pålsvatnet, PÅLP-119 only contained a short marine section, whereas PÅLP-219 recovered a more extended portion of marine sediments. After splitting the lowermost section of PÅLP-219, the P1 unit found in the deepest part of the core, revealed that it consisted of a diamicton that made it distinctly different from the rest of the core (figure 4.10, chapter 4). Marine shells were found all the way through this unit in the core. Moreover, unit P1 had two distinct sections, i.e., the lower one with comparatively larger grain sizes than the upper one. There was no distinct layering found in this unit.

As the unit was found in the deepest part of the core, and the lower boundary was not recovered, there are several possible interpretations. It could be formed as a result of slumping caused by an extreme event like an avalanche or tsunami. Because of the almost completely flat topography around the lake, the most plausible explanation for this slumping could be a result of an extreme high-energy wave during a sudden natural event like a tsunami (Svendsen and Mangerud, 1990). No matter if the lake was located above or below the shoreline during a tsunami event, the tsunami deposits could be found both below and above the shoreline (Lohne et al., 2007). Theoretically, both the thickness and grain sizes decrease gradually in a tsunami deposit, although the succession can be repeated if there are several consecutive waves (Bondevik et al., 2005). Unit P1 of the core reflected facies similar to that which could be deposited by a tsunami. Moreover, the presence of a considerable amount of marine shells in the core has made it more certain that the sediments are marine in origin. The reconstructed maximum run-up of the Storegga tsunami was 6 – 7 m above mean sea level in Lyngen, northern Norway (Rasmussen et al., 2018). According to the relative sea-level curve of this study, the lake was located around 9 m below mean sea level during the Storegga tsunami event. Thus, it seems likely that deposits from the Storegga tsunami could be found in the basin. In addition to visual stratigraphic interpretation, there was a plan to conduct a CT-scan to confirm the tsunami event; however, this was not possible because of lockdown due to the coronavirus pandemic.

The reported date of the Storegga tsunami along the Norwegian coast is 7300 ^{14}C year BP or 8150 cal BP (Bondevik et al., 2005). The highest age found from the marine part of this study was 6550 ± 85 cal BP. No dating was conducted from the unit of the core interpreted as a tsunami deposit itself, but from the stratigraphic position of the interpreted tsunami layer, it is possible to say that the event occurred before 6550 ± 85 cal BP that corresponds with the reported date of the Storegga tsunami event.

6. Conclusion

- Based on the previous studies, the Evenes area was deglaciated a few hundred years after the Younger Dryas, around 10965 ± 205 cal BP.
- The altitude of the topset-foreset boundary of the glaciofluvial delta found in the study area (75.83 m above the mean sea level after adjusting the tidal range), is thought to reflect the marine limit.
- Most probably, Storegga tsunami deposits are preserved at the bottom of the lake core stratigraphy, which is shown here older than 6550 ± 85 cal BP.
- Pålsvatnet was isolated around 6240 ± 60 cal BP.
- The average regression rate of the sea level was higher before the period the lake isolated, and it became slower afterward. However, the lowest regression rate probably occurred just prior to the isolation, at the time as areas further west experienced a transgression.
- The area experienced around 130 m postglacial land uplift throughout the Holocene.
- Based on a constructed shoreline diagram, shoreline gradients between Leknes and Evenes were calculated to 0.79 m/km, 0.54 m/km, 0.37 m/km, 0.24 m/km, 0.22 m/km, 0.20 m/km. 0.15 m/km, 0.10 m/km, 0.06 m/km and 0.04 m/km for the periods 10,000 cal BP, 9000 cal BP, 8000 cal BP, 7000 cal BP, 6000 cal BP, 5000 cal BP, 4000 cal BP, 3000 cal BP, 2000 cal BP, and 1000 cal BP, respectively.
- Based on the shoreline diagram, the mid-Holocene Tapes transgression could be found up to around 40 km inland from Leknes, where the 8000 cal BP and 7000 cal BP shorelines intersect.

7. Recommendations for Further Research

- Isolation basins are somewhat more reliable than a glaciofluvial delta for obtaining a precise sea-level index point. Isolation basins located close to the altitude of the glaciofluvial delta should therefore be analyzed to get a more precise sea-level index point for the marine limit. This would also make it possible to get a more precise minimum age of deglaciation for the area.
- More isolation basins should be studied at different altitudes to make the curve more precise.
- The inland extent of the Tapes transgression suggested from the shoreline diagram can be tested by coring isolation basins situated at the right distance along the projection plane.
- The layer interpreted as the tsunami deposit should be studied in more detail and dated to establish its possible relation to the Storegga tsunami.
- Mapping the Storegga tsunami at different altitudes can be done to calculate the run-up heights of the tsunami of the area.

8. References

ANUNDSEN, K. & FJELDSKAAR, W. Observed and theoretical late Weichselian shore-level changes related to glacier oscillations at Yrkje, south-west Norway. Late-and postglacial oscillations of glaciers: glacial and periglacial forms Colloquium, 1983. 133-170.

BAKKE, J., DAHL, S. O., PAASCHE, Ø., SIMONSEN, J. R., KVISVIK, B., BAKKE, K. & NESJE, A. 2010. A complete record of Holocene glacier variability at Austre Okstindbreen, northern Norway: an integrated approach. *Quaternary Science Reviews,* 29**,** 1246-1262.

BALASCIO, N. L., ZHANG, Z., BRADLEY, R. S., PERREN, B., DAHL, S. O. & BAKKE, J. 2011. A multi-proxy approach to assessing isolation basin stratigraphy from the Lofoten Islands, Norway. *Quaternary Research,* 75**,** 288-300.

BARD, E., HAMELIN, B., ARNOLD, M., MONTAGGIONI, L., CABIOCH, G., FAURE, G. & ROUGERIE, F. 1996. Deglacial sea-level record from Tahiti corals and the timing of global meltwater discharge. *Nature,* 382**,** 241-244.

BARNETT, R. L., GEHRELS, W. R., CHARMAN, D. J., SAHER, M. H. & MARSHALL, W. A. 2015. Late Holocene sea-level change in Arctic Norway. *Quaternary Science Reviews,* 107**,** 214-230.

BAZYLINSKI, D. A., FRANKEL, R. B., GARRATT-REED, A. J. & MANN, S. 1991. Biomineralization of iron sulfides in magnetotactic bacteria from sulfidic environments. *Iron biominerals.* Springer.

BENN, D. & EVANS, D. J. 2013. *Glaciers and glaciation*, Routledge.

BERGLUND, M. 2004. Holocene shore displacement and chronology in Ångermanland, eastern Sweden, the Scandinavian glacio-isostatic uplift centre. *Boreas,* 33**,** 48-60.

BERGSTROM, B., OLSEN, L. & SVEIAN, H. 2005. The Tromso-Lyngen glacier readvance (early Younger Dryas) at Hinnoya-Ofotfjorden, northern Norway: a reassessment. *NORGES GEOLOGISKE UNDERSOKELSE,* 445**,** 73.

BILLS, B. G. & RAY, R. D. 1999. Lunar orbital evolution: A synthesis of recent results. *Geophysical Research Letters,* 26**,** 3045-3048.

BLAAUW, M. 2010. Methods and code for 'classical' age-modelling of radiocarbon sequences. *Quaternary Geochronology,* 5**,** 512-518.

BLOOM, A. L., BROECKER, W. S., CHAPPELL, J. M. A., MATTHEWS, R. K. & MESOLELLA, K. J. 1974. Quaternary sea level fluctuations on a tectonic coast: New 230Th234U dates from the Huon Peninsula, New Guinea. *Quaternary Research,* 4**,** 185-205.

BONDEVIK, S., MANGERUD, J., DAWSON, S., DAWSON, A. & LOHNE, Ø. 2005. Evidence for three North Sea tsunamis at the Shetland Islands between 8000 and 1500 years ago. *Quaternary Science Reviews,* 24**,** 1757-1775.

BONDEVIK, S., STORMO, S. K. & SKJERDAL, G. 2012. Green mosses date the Storegga tsunami to the chilliest decades of the 8.2 ka cold event. *Quaternary Science Reviews,* 45**,** 1-6.

BRADLEY, R. S. 2014. *Paleoclimatology : reconstructing climates of the quaternary,* London, Elsevier.

BRYSON, R. A., WENDLAND, W. M., IVES, J. D. & ANDREWS, J. T. 1969. Radiocarbon isochrones on the disintegration of the Laurentide Ice Sheet. *Arctic and Alpine Research,* 1**,** 1-13.

CARCAILLET, C., HÖRNBERG, G. & ZACKRISSON, O. 2012. Woody vegetation, fuel and fire track the melting of the Scandinavian ice-sheet before 9500 cal yr BP. *Quaternary Research,* 78**,** 540-548.

CHAPPELL, J. 1983. Evidence for smoothly falling sea level relative to north Queensland, Australia, during the past 6,000 yr. *Nature,* 302**,** 406-408.

CHRIST, R. D. & WERNLI, R. L. 2014. Chapter 2 - The Ocean Environment. *In:* CHRIST, R. D. & WERNLI, R. L. (eds.) *The ROV Manual (Second Edition).* Oxford: Butterworth-Heinemann.

CORNER, G., NORDAHL, E., MUNCH-ELLINGSEN, K. & ROBERTSEN, K. 1990. Morphology and sedimentology of an emergent fjord-head Gilbert-type delta: Alta delta, Norway. *Coarse-grained deltas.* International Association of Sedimentologists, Special Publication 10.

CRONIN, T., VOGT, P., WILLARD, D., THUNELL, R., HALKA, J., BERKE, M. & POHLMAN, J. 2007. Rapid sea level rise and ice sheet response to 8,200-year climate event. *Geophysical Research Letters,* 34.

CROUDACE, I. W., RINDBY, A. & ROTHWELL, R. G. 2006. ITRAX: description and evaluation of a new multi-function X-ray core scanner. *Geological Society, London, Special Publications,* 267**,** 51-63.

CROUDACE, I. W. & ROTHWELL, R. G. 2015. Chapter 1 Micro-XRF Studies of Sediment Cores: A Perspective on Capability and Application in the Environmental Sciences. *In:* CROUDACE, I. W. & ROTHWELL, R. G. (eds.) *Micro-XRF Studies of Sediment Cores : Applications of a non-destructive tool for the environmental sciences.* 1st ed. 2015. ed. Dordrecht: Springer Netherlands : Imprint: Springer.

DA SILVA, A.-C. & BOULVAIN, F. 2006. Upper Devonian carbonate platform correlations and sea level variations recorded in magnetic susceptibility. *Palaeogeography, Palaeoclimatology, Palaeoecology,* 240**,** 373-388.

DABRIO, C. J., BARDAJÍ AZCÁRATE, T., ZAZO CARDEÑA, C. & GOY GOY, J. L. 1991. Effects of sea-level changes on a wave-worked Gilbert-type delta (Late Pliocene, Aguilas Basin, SE Spain). *Cuadernos de geología ibérica*.

DEARING, J. A. 1999. Environmental Magnetic Susceptibility: using the Bartington MS2 System. *Chi Pub. Kenilworth*.

DESCHAMPS, P., DURAND, N., BARD, E., HAMELIN, B., CAMOIN, G., THOMAS, A. L., HENDERSON, G. M., OKUNO, J. I. & YOKOYAMA, Y. 2012. Ice-sheet collapse and sea-level rise at the Bølling warming 14,600 years ago. *Nature,* 483**,** 559-564.

DUTTON, A., CARLSON, A. E., LONG, A., MILNE, G. A., CLARK, P. U., DECONTO, R., HORTON, B. P., RAHMSTORF, S. & RAYMO, M. E. 2015. Sea-level rise due to polar ice-sheet mass loss during past warm periods. *science,* 349**,** aaa4019.

EILERTSEN, R. S., CORNER, G. D., AASHEIM, O. & HANSEN, L. 2011. Facies characteristics and architecture related to palaeodepth of Holocene fjord–delta sediments. *Sedimentology,* 58**,** 1784-1809.

ELDEVIK, T., RISEBROBAKKEN, B., BJUNE, A. E., ANDERSSON, C., BIRKS, H. J. B., DOKKEN, T. M., DRANGE, H., GLESSMER, M. S., LI, C. & NILSEN, J. E. Ø. 2014. A brief history of climate–the northern seas from the Last Glacial Maximum to global warming. *Quaternary Science Reviews,* 106**,** 225-246.

FÆGRI, K., KALAND, P. E., KRZYWINSKI, K. & IVERSEN, J. 1989. *Textbook of pollen analysis*, Chichester, Wiley.

FORWICK, M. & VORREN, T. O. 2002. Deglaciation history and post-glacial mass movements in Balsfjord, northern Norway. *Polar Research,* 21**,** 259-266.

GEHRELS, W. R. & WOODWORTH, P. L. 2013. When did modern rates of sea-level rise start? *When did modern rates of sea-level rise start?,* 100**,** 263-277.

GEODATA. 2019. *Maps, data and content services*. Geodata AS.

GEONORGE 2020. Online GIS server. Norwegian Mapping Authority (Kartverket).

GORNITZ, V. 2013. *Rising Seas : Past, Present, Future*, New York, Columbia University Press.

GUNN, D. E. & BEST, A. I. 1998. A new automated nondestructive system for high resolution multi-sensor core logging of open sediment cores. *Geo-Marine Letters*, 18**,** 70-77.

HAFLIDASON, H., LIEN, R., SEJRUP, H. P., FORSBERG, C. F. & BRYN, P. 2005. The dating and morphometry of the Storegga Slide. *Marine and Petroleum Geology*, 22**,** 123-136.

HAFLIDASON, H., SEJRUP, H. P., NYGÅRD, A., MIENERT, J., BRYN, P., LIEN, R., FORSBERG, C. F., BERG, K. & MASSON, D. 2004. The Storegga Slide: architecture, geometry and slide development. *Marine geology*, 213**,** 201-234.

HEIRI, O., LOTTER, A. F. & LEMCKE, G. 2001. Loss on ignition as a method for estimating organic and carbonate content in sediments: reproducibility and comparability of results. *Journal of Paleolimnology*, 25**,** 101-110.

HIJMANS, R. 2020. *Geographic (GIS) Data* [Online]. DIVA-GIS. Available: https://www.diva-gis.org/gdata [Accessed 15 March 2020].

HORI, K., SAITO, Y., ZHAO, Q., CHENG, X., WANG, P., SATO, Y. & LI, C. 2001. Sedimentary facies and Holocene progradation rates of the Changjiang (Yangtze) delta, China. *Geomorphology*, 41**,** 233-248.

HØYDEDATA. 2019. *National Datasets* [Online]. Norwegian Mapping Authority (Kartverket). Available: https://hoydedata.no/LaserInnsyn/ [Accessed 07 August 2019].

HUGHES, A. L., GYLLENCREUTZ, R., LOHNE, Ø. S., MANGERUD, J. & SVENDSEN, J. I. 2016. The last Eurasian ice sheets–a chronological database and time-slice reconstruction, DATED-1. *Boreas*, 45**,** 1-45.

IPCC 2019. Summary for Policymakers. *In:* PÖRTNER , H.-O., ROBERTS, D. C., MASSON-DELMOTTE, V., ZHAI, P., TIGNOR, M., POLOCZANSKA, E., MINTENBECK, K., ALEGRÍA, A., NICOLAI, M., OKEM, A., PETZOLD, J., RAMA, B. & WEYE, N. M. (eds.) *IPCC Special Report on the Ocean and Cryosphere in a Changing Climate.* In press.

JANKOVSKÁ, V. & KOMÁREK, J. 1995. Pediastrum orientale from subfossil layers. *Folia Geobotanica*, 30**,** 319-329.

JANKOVSKÁ, V. & KOMÁREK, J. 2000. Indicative value of Pediastrum and other coccal green algae in palaeoecology. *Official Journal of the Institute of Botany, Academy of Sciences of the Czech Republic*, 35**,** 59-82.

JUGGINS, S. 2017. rioja: Analysis of Quaternary Science Data, R package version (0.9-21).

KALAND, P. E. 1984. Holocene shore displacement and shorelines in Hordaland, western Norway. *Boreas,* 13**,** 203-242.

KARTVERKET 2019. Tidevannstabeller for den Norse kyst med Svalbard, smat Dover, England. Stavanger. 82. Årgang: Kartverket sjødivisjonen.

KARTVERKET. 2020. *Water level and tidal information* [Online]. Available: https://www.kartverket.no/en/sehavniva/Lokasjonsside/?cityid=735022&city=Evenes%20kommune#tab2 [Accessed 20 April 2020].

KJEMPERUD, A. 1981. Diatom changes in sediments of basins possessing marine/lacustrine transitions in Frosta, Nord-Trøndelag, Norway. *Boreas,* 10**,** 27-38.

KJEMPERUD, A. 1986. Late Weichselian and Holocene shoreline displacement in the Trondheimsfjord area, central Norway. *Boreas,* 15**,** 61-82.

KOMÁREK, J. I. & JANKOVSKÁ, V. 2001. *Review of the green algal genus Pediastrum,* J. Cramer.

LAMBECK, K., ROUBY, H., PURCELL, A., SUN, Y. & SAMBRIDGE, M. 2014. Sea level and global ice volumes from the Last Glacial Maximum to the Holocene. *Proceedings of the National Academy of Sciences,* 111**,** 15296.

LID, K. A. 2019. Holocen strandforskyvnin ved Skånland, Troms. Bergen: Universitetet i Bergen. Available at: http://bora.uib.no/handle/1956/21311 [Accessed 20 September 2020].

LOHNE, Ø. S., BONDEVIK, S., MANGERUD, J. & SVENDSEN, J. I. 2007. Sea-level fluctuations imply that the Younger Dryas ice-sheet expansion in western Norway commenced during the Allerød. *Quaternary Science Reviews,* 26**,** 2128-2151.

LOHNE, Ø. S., MANGERUD, J. & SVENDSEN, J. I. 2012. Timing of the Younger Dryas glacial maximum in western Norway. *Journal of Quaternary Science,* 27**,** 81-88.

LONG, A. J., WOODROFFE, S. A., ROBERTS, D. H. & DAWSON, S. 2011. Isolation basins, sea-level changes and the Holocene history of the Greenland Ice Sheet. *Quaternary Science Reviews,* 30**,** 3748-3768.

MACDONALD, G. M., BEUKENS, R. P., KIESER, W. E. & VITT, D. H. 1987. Comparative radiocarbon dating of terrestrial plant macrofossils and aquatic moss from the "ice-free corridor" of western Canada. *Geology,* 15**,** 837-840.

MANGERUD, J., ANDERSEN, S. T., BERGLUND, B. E. & DONNER, J. J. 1974. Quaternary stratigraphy of Norden, a proposal for terminology and classification. *Boreas,* 3**,** 109-126.

MANGERUD, J., BONDEVIK, S., GULLIKSEN, S., HUFTHAMMER, A. K. & HØISÆTER, T. 2006. Marine 14C reservoir ages for 19th century whales and molluscs from the North Atlantic. *Quaternary Science Reviews,* 25**,** 3228-3245.

MARTHINUSSEN, M. 1962. C14-datings referring to shore lines, transgressions, and glacial substages in northern Norway. *Norges geologiske undersøkelse,* 215**,** 37-67.

MIDTUN, E. S. 2019. Holosen strandforskyvning for Leknes, Vestvågøy. The University of Bergen. Available at: http://bora.uib.no/handle/1956/20900?show=full [Accessed 25 January 2020].

MILNE, G., A., GEHRELS, W. R., CHRIS, W. H. & MARK, E. T. 2009. Identifying the causes of sea-level change. *Nature Geoscience,* 2**,** 471.

MØLLER, J. J. 1984. Holocene shore displacement at Nappstraumen, Lofoten, North Norway. *Nor. Geol. Tidsskr,* 64**,** 1-5.

MØLLER, J. J. 1986. Holocene transgression maximum about 6000 years BP at Ramså, Vesterålen, North Norway.

MØLLER, J. J. 1989. Geometric simulation and mapping of Holocene relative sea-level changes in northern Norway. *Journal of Coastal Research,* 403-417.

MÖRNER, N.-A. 1976. Eustasy and geoid changes. *The Journal of Geology,* 84**,** 123-151.

NESJE, A. 1992. A piston corer for lacustrine and marine sediments. *Arctic and Alpine Research,* 24**,** 257-259.

NGU. 2020a. *Areal Information - Norway, Svalbard and ocean areas* [Online]. Available: http://geo.ngu.no/kart/arealis_mobil/ [Accessed 28 May 2020].

NGU. 2020b. *Bedrock - National Bedrock Database* [Online]. Available: http://geo.ngu.no/kart/berggrunn_mobil/ [Accessed 10 May 2020].

NGU. 2020c. *Superficial Deposits - National Database* [Online]. Available: http://geo.ngu.no/kart/losmasse_mobil/?lang=eng [Accessed 11 May 2020].

NORGESKART. 2019. *Topographic map*. Norwegian Mapping Authority.

NORSK-KLIMASERVICESENTER. 2020. *Observations and weather statistics* [Online]. Norsk-Klimaservicesenter. Available: https://seklima.met.no/observations/ [Accessed 20 May 2020].

NVE. 2020. *NVE Nebørfelt (REGINE)* [Online]. Norwegian Water Resource and Energy Directorate (NVE). Available: https://temakart.nve.no/link/?link=nedborfelt [Accessed 25 January 2020].

OKSANEN, J., BLANCHET, F. G., FRIENDLY, M., KINDT, R., LEGENDRE, P., MCGLINN, D., MINCHIN, P. R., O'HARA, R. B., SIMPSON, G. L., SOLYMOS, P.,

STEVENS, M. H. H., SZOECS, E. & WAGNER, H. 2019. vegan: Community Ecology Package.

OLSEN, L. 2002. Mid and Late Weichselian, ice-sheet fluctuations northwest of the Svartisen glacier, Nordland, northern Norway. *Geological Survey of Norway Bulletin,* 440.

OPPENHEIMER, M., GLAVOVIC, B. C., HINKEL, J., VAN DE WAL, R., MAGNAN, A. K., ABD-ELGAWAD, A., CAI, R., CIFUENTES-JARA, M., DECONTO, R. M., GHOSH, T., HAY, J., ISLA, F., MARZEION, B., MEYSSIGNAC, B. & SEBESVARI, Z. 2019. Sea Level Rise and Implications for Low-Lying Islands, Coasts and Communities. *In:* PÖRTNER, H.-O., ROBERTS, D. C., MASSON-DELMOTTE, V., ZHAI, P., TIGNOR, M., POLOCZANSKA, E., MINTENBECK, K., ALEGRÍA, A., NICOLAI, M., OKEM, A., PETZOLD, J., RAMA, B. & WEYER, N. M. (eds.) *IPCC Special Report on the Ocean and Cryosphere in a Changing Climate.* In press.

PELTIER, W. R., ARGUS, D. & DRUMMOND, R. 2015. Space geodesy constrains ice age terminal deglaciation: The global ICE-6G_C (VM5a) model. *Journal of Geophysical Research: Solid Earth,* 120**,** 450-487.

PRL. 2020. *Uncertainity of Radiocarbon Date* [Online]. Poznan Radiocarbon Labratory. Available: https://radiocarbon.pl/en/uncertainty-of-radiocarbon-date/#maleprobki [Accessed 20 March 2020].

RAMBERG, I. B. The making of a land: geology of Norway. 2008. Geological Society of London.

RASMUSSEN, A. 1984. Late Weichselian moraine chronology of the Vesterålen islands, North Norway. *Norsk geologisk tidsskrift,* 64**,** 193-219.

RASMUSSEN, H., BONDEVIK, S. & CORNER, G. D. 2018. Holocene relative sea level history and Storegga tsunami run-up in Lyngen, northern Norway. *Journal of Quaternary Science,* 33**,** 393-408.

RASMUSSEN, S. O., ANDERSEN, K. K., SVENSSON, A., STEFFENSEN, J. P., VINTHER, B. M., CLAUSEN, H. B., SIGGAARD-ANDERSEN, M. L., JOHNSEN, S. J., LARSEN, L. B. & DAHL-JENSEN, D. 2006. A new Greenland ice core chronology for the last glacial termination. *Journal of Geophysical Research: Atmospheres,* 111.

REIMER, P. J., BARD, E., BAYLISS, A., BECK, J. W., BLACKWELL, P. G., RAMSEY, C. B., BUCK, C. E., CHENG, H., EDWARDS, R. L. & FRIEDRICH, M. 2013. IntCal13 and Marine13 radiocarbon age calibration curves 0–50,000 years cal BP. *Radiocarbon,* 55**,** 1869-1887.

REYNOLDS, C. S. 2006. *The ecology of phytoplankton,* Cambridge University Press.

RICHTER, K., NILSEN, J. Ø. & DRANGE, H. 2012. Contributions to sea level variability along the Norwegian coast for 1960–2010. *Journal of Geophysical Research: Oceans,* 117.

ROMUNDSET, A., LAKEMAN, T. R. & HØGAAS, F. 2018. Quantifying variable rates of postglacial relative sea level fall from a cluster of 24 isolation basins in southern Norway. *Quaternary Science Reviews,* 197**,** 175-192.

ROMUNDSET, A., LAKEMAN, T. R. & HØGAAS, F. 2019. Coastal lake records add constraints to the age and magnitude of the Younger Dryas ice-front oscillation along the Skagerrak coastline in southern Norway. *Journal of Quaternary Science,* 34**,** 112-124.

SARMAJA-KORJONEN, K., SEPPÄNEN, A. & BENNIKE, O. 2006. *Pediastrum* algae from the classic late glacial Bølling Sø site, Denmark: Response of aquatic biota to climate change. *Review of Palaeobotany and Palynology,* 138**,** 95-107.

SHENNAN, I., BRADLEY, S. L. & EDWARDS, R. 2018. Relative sea-level changes and crustal movements in Britain and Ireland since the Last Glacial Maximum. *Quaternary Science Reviews,* 188**,** 143-159.

SHENNAN, I., LAMBECK, K., HORTON, B., INNES, J., LLOYD, J., MCARTHUR, J., PURCELL, T. & RUTHERFORD, M. 2000. Late Devensian and Holocene records of relative sea-level changes in northwest Scotland and their implications for glacio-hydro-isostatic modelling. *Quaternary Science Reviews,* 19**,** 1103-1135.

SHENNAN, I., LONG, A. J. & HORTON, B. P. 2015. *Handbook of sea-level research*, John Wiley & Sons.

SHERMAN, I., GREEN, F., INNES, J., LLOYD, J., RUTHERFORD, M. & WALKER, K. 1996. Evaluation of rapid relative sea-level changes in north-west Scotland during the last Glacial-Interglacial transition: evidence from Ardtoe and other isolation basins. *Journal of Coastal Research***,** 862-874.

SHOTTON, F. W. 1972. An example of hard-water error in radiocarbon dating of vegetable matter. *Nature,* 240**,** 460-461.

SIMPSON, M. J., NILSEN, J. E. Ø., RAVNDAL, O. R., BREILI, K., SANDE, H., KIERULF, H. P., STEFFEN, H., JANSEN, E., CARSON, M. & VESTØL, O. 2015. Sea Level Change for Norway: Past and Present Observations and Projections to 2100. *Norwegian Centre for Climate Services report,* 1**,** 2015.

STANFORD, J. D., HEMINGWAY, R., ROHLING, E. J., CHALLENOR, P. G., MEDINA-ELIZALDE, M. & LESTER, A. J. 2011. Sea-level probability for the last deglaciation: A statistical analysis of far-field records. *Global and Planetary Change,* 79**,** 193-203.

STOCKMARR, J. 1972. Tablets with spores used in absolute pollen analysis. Pollen et Spores, 13 (4): 615-621., 1973: Determination of spore concentration with an electronic particle counter. *Geol. Survey of Denmark***,** 87-89.

STRØM, K. 1957. A lake with trapped sea-water? *Nature,* 180**,** 982-983.

STRUNK, A., LARSEN, N. K., NILSSON, A., SEIDENKRANTZ, M. S., LEVY, L. B., OLSEN, J. & LAURIDSEN, T. L. 2018. Relative Sea-Level Changes and Ice Sheet History in Finderup Land, North Greenland. *Frontiers In Earth Science,* 6.

SVENDSEN, J. I. & MANGERUD, J. 1987. Late Weichselian and Holocene sea-level history for a cross-section of western Norway. *Journal of Quaternary Science,* 2**,** 113-132.

SVENDSEN, J. I. & MANGERUD, J. 1990. Sea-level changes and pollen stratigraphy on the outer coast of Sunnmøre, western Norway. *Norsk Geologisk Tidsskrift,* 70**,** 111-134.

TARASOV, L. GLAC-1b: a new data-constrained global deglacial ice sheet reconstruction from glaciological modelling and the challenge of missing ice. EGU General Assembly Conference Abstracts, 2013.

TELLER, J. T., LEVERINGTON, D. W. & MANN, J. D. 2002. Freshwater outbursts to the oceans from glacial Lake Agassiz and their role in climate change during the last deglaciation. *Quaternary Science Reviews,* 21**,** 879-887.

TJEMSLAND, A. E. 1983. Vegetasjonhistoriske og Plaeoøkologiske Undersøkeler av Rekkingedalstjørma og Sengsvatnet, Fedje, Hordaland. *Institutt for Geovitenskap.* Bergen: Universitetet i Bergen.

TURNER, F., POTT, R., SCHWARZ, A. & SCHWALB, A. 2014. Response of Pediastrum in German floodplain lakes to Late Glacial climate changes. *Journal of Paleolimnology,* in press.

VAN VUUREN, D. P., EDMONDS, J., KAINUMA, M., RIAHI, K., THOMSON, A., HIBBARD, K., HURTT, G. C., KRAM, T., KREY, V. & LAMARQUE, J.-F. 2011. The representative concentration pathways: an overview. *Climatic change,* 109**,** 5.

VASSKOG, K. 2006. Holosen stranforskyvning på sørlige Bømlo. *Institutt for Geovitenskap.* Bergen: Universitetet i Bergen.

VASSKOG, K., SVENDSEN, J.-I., MANGERUD, J., AGASØSTER HAAGA, K., SVEAN, A. & LUNNAN, E. M. 2019. Evidence of early deglaciation (18 000 cal a bp) and a

postglacial relative sea-level curve from southern Karmøy, south-west Norway. *Journal of Quaternary Science,* 34**,** 410-423.

VASSKOG, K., WALDMANN, N., BONDEVIK, S., NESJE, A., CHAPRON, E. & ARIZTEGUI, D. 2013. Evidence for Storegga tsunami run-up at the head of Nordfjord, western Norway. *Journal of Quaternary Science,* 28**,** 391-402.

VINK, A., STEFFEN, H., REINHARDT, L. & KAUFMANN, G. 2007. Holocene relative sea-level change, isostatic subsidence and the radial viscosity structure of the mantle of northwest Europe (Belgium, the Netherlands, Germany, southern North Sea). *Quaternary Science Reviews,* 26**,** 3249-3275.

VORREN, K.-D. & MOE, D. 1986. The early Holocene climate and sea-level changes in Lofoten and Vesterålen, North Norway. *Norsk geologisk tidsskrift,* 66**,** 135-143.

VOS, P. C. & DE WOLF, H. 1993. Diatoms as a tool for reconstructing sedimentary environments in coastal wetlands; methodological aspects. *Hydrobiologia,* 269**,** 285-296.

WALKER, M., HEAD, M. J., LOWE, J., BERKELHAMMER, M., BJÖRCK, S., CHENG, H., CWYNAR, L. C., FISHER, D., GKINIS, V. & LONG, A. 2019. Subdividing the Holocene Series/Epoch: formalization of stages/ages and subseries/subepochs, and designation of GSSPs and auxiliary stratotypes. *Journal of Quaternary Science,* 34**,** 173-186.